Enhanced transport through confined channels by stationary and fluctuating potentials

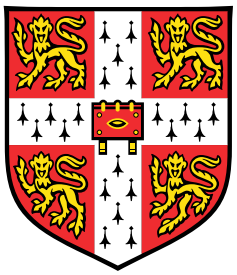

Yizhou Tan

Department of Physics
University of Cambridge

This dissertation is submitted for the degree of
Doctor of Philosophy

Churchill College

December 2018

Abstract

Binding-sites which facilitate the transport of substrates across membranes are ubiquitous in membrane proteins. To understand this fundamental process in cells, we build up a synthetic membrane system consisting of microfluidic channels and colloidal particles. Holographic optical tweezers are used to modulate the potential energy landscape in those channels.

We show how to extract the underlying energy potential by analysing local transition probabilities. Our method is applicable both to equilibrium systems and non-equilibrium steady states. Our method offers improved robustness when dealing with fragmented trajectories or small ensembles of data compared to other established approaches, such as probability density function and splitting probability. Meanwhile, we utilise the intensity distribution of the optical traps generated by holographic optical tweezers to estimate energy landscapes featuring high energy barriers where transitions rarely occur.

We use this newly developed experimental system to mimic the functionality of membrane protein transporters that are known to alternate their substrate-binding sites between the extracellular and cytosolic side of the membrane. We study particle transport through a channel coupled with an energy well that oscillates its position between the two entrances of the channel deterministically and stochastically. Optimised particle transport across the channel is obtained by adjusting the oscillation frequency. At the optimal oscillation frequency, the translocation rate of particles through the channel is a hundred times higher with respect to free diffusion across the channel. Our findings reveal the effect of time dependent potentials on particle transport across a channel. This work adds a new tool for the investigation of highly controlled membrane transport processes at the micron scale. Our results are relevant for improving our understanding of membrane transport especially for microfluidics application.

I would like to dedicate this thesis to my loving parents, my sister and MB.

Declaration

I hereby declare that except where specific reference is made to the work of others, the contents of this dissertation are original and have not been submitted in whole or in part for consideration for any other degree or qualification in this, or any other university. This dissertation is my own work and contains nothing which is the outcome of work done in collaboration with others, except as specified in the text and Acknowledgements. This dissertation contains fewer than 65,000 words including appendices, bibliography, footnotes, tables and equations and has fewer than 150 figures.

Yizhou Tan
December 2018

Acknowledgements

First of all, I would like to say thank you to Ulrich for being a fantastic PhD supervisor. You have given me the opportunity to work on an interdisciplinary project with a group of amazing people. The guidance and the freedom you provided me with has let me complete my thesis with a smile. It has been an honour to join the Keyser group and be part of it.

Stefano, "Thank you" is never adequate to express my gratitude to you. You have taught me how to make PDMS, how to think, how to present, how to write. More importantly, you made me a better person. The skills you have taught me will be beneficial for my whole life. The passion you have for science inspires me to pursue my dream.

I would also like to thank Sebastian for his help on splitting probability, Leonardo for simulations, Michael for helpful suggestions and Richard for the help on tweezers software. I give special thanks to Jannes for rebuilding the optical tweezers in the darkness and opening my horizon on the possibilities of automation. I thank Alice, for her massive help while writing my thesis. She has inspired me to live a happy life, being strong while being nice. I also thank Jeff, Jehangir and Karolis for proof reading my thesis.

Jinglin is my best friend. Without her caring and the courage she inspired in me, I can barely carry on until now. I thank two undergraduate students, Hugh and Floris for joining me and becoming my friends at the end of their projects. I thank Maria for training me on AFM and my office mate Andrew for his fitness suggestions. I have special thanks to my housemates, Jason and Ziyan for all the scientific and non-scientific discussions. Matt for teaching me to play squash and my lunch buddies Shaoran, Hongfei and Haichang. I should also thank Churchill College for feeding me for in the last four and half years, their food is second to none, the best in west Cambridge.

In the end, I thank my parents for providing me amazing opportunities to receive a world class education and my sister for supporting me whenever I am down or need someone to talk. Just before I finish, I give my last acknowledgement to MB thank you for looking after me, for proofreading my English, for supporting my thesis writing and most importantly, thank you for joining the journey. Four years ago I thought finishing this thesis would be the biggest achievement in my life, but now I realise there is much more in life. There are endless adventures in front.

Table of contents

List of figures

List of tables

Chapter 1

Introduction

1.1 Brownian motion

A microscopic particle suspended in a solvent collides with millions of solvent molecules, which results in random movements of the particle, so called Brownian motion. Although ubiquitous in nature, it was not detailed until the early 1800s when botanist Robert Brown observed pollens undergoing random movement in aqueous solvent. The random movement was previously attributed to that the moving particle is alive. However, Robert Brown substituted the pollen with ashes from his chimney and observed similar movement which demonstrated the motion is due to the solvent [1].

Brownian motions are frequently encountered and are of widespread significance in cellular environments. Ions, proteins and other macromolecules are undergoing Brownian motion [2–4]. For example, an ion diffusing outside a cell finds a protein channel embedded in the cell membrane and squeezes through it [5]. Although Brownian motion of a pollen grain and an ion happens under totally different time and length scales, the fundamental mechanism is the same, random but constant bombardments from solvent molecules.

Meanwhile, a diffusion process can be demonstrated easily by putting a drop of ink into a glass of water, which then spreads out over time. In 1905, Einstein and one year later Smoluchowski, offered independent explanations connecting the diffusion phenomenon to Brownian motion based on kinetic theory [6]. Since then, this simple but fundamental physical motion has been studied in all kinds of systems, ranging from nutrition exchange in cells to fluctuation in financial markets, from water purification to climate change [7].

1.2 Transport proteins in cell membranes

Cell membranes are made up of lipid bilayers embedded with proteins. A protein-free lipid bilayer is essentially impermeable to many polar molecules, such as ions, sugars and amino acids. However, those molecules are essential for cell metabolism, communication and function. The proteins embedded in the lipid bilayer actually transfer such solutes between the cytosol and cell exterior. Transporters and channels are two main types of membrane transport proteins. The transporters bind the specific solute and undergo conformational changes to transport the solute across the membrane, while the channels form continuous pores and interact weakly with the solute being transported [8].

The probability for an substrate to be transported through a membrane protein by diffusion is extremely low considering the vast volume of the cellular environment compared to the size of a molecule and the number of proteins. The access to binding sites which have high affinity to specific substrate alternates between extracellular and cytosolic side. Proposed as 'alternating access model' nearly half century ago, this conformational changes in membrane proteins has been used to understand the transport process in all membrane transporters [9]. Three different mechanisms which can be incorporated by a single protein are sketched in Fig. 1.1 [10]. The similarity between them is that the conformational change in the

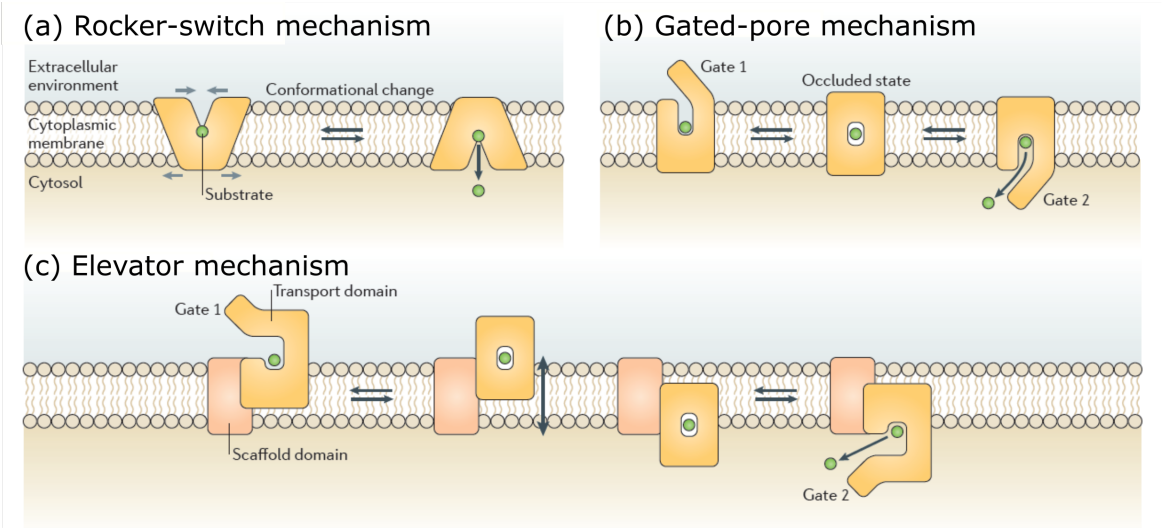

Fig. 1.1 Models for alternating access mechanism in membrane proteins. (a) Rocker-switch model, where substrate binds to the transporter at a site near the centre of the membrane. The protein then undergoes conformational changes. (b) Gated-pore mechanism, where the gates cannot open simultaneously. The protein is opened to extracellular environment to let a substrate in and then open to cytosol to let substrate diffuse out. (c) Elevator mechanisms, the substrate moves during the transport cycle. The protein undergoes a sliding movement but the overall conformation remains the same. Note: the figure is adapted from literature [10].

transporters alters access of substrate to channel thus the protein oscillates between open and closed states. Take the ABC transporters family for example; each member has two highly conserved ATP-Binding "cassettes", so called ATPases. The two ATPases can be brought together by binding and dissociated by ATP hydrolysis. Those movements are transmitted to the transmembrane segments which drive conformational changes in cycles [8, 11–14].

1.3 Building up a synthetic membrane system

Despite transport across membranes is ubiquitous, studying it experimentally is notoriously hard and the transport mechanism is not fully understood. Crystal structures of proteins show the position of binding sites and different structural conformations [15–18], but missing dynamical information. Model lipid bilayers provide access to the transport of specific solutes across membranes [19–21] but are impractical to modify in terms of individual binding affinities. On the other hand, the physical mechanisms underlying transport optimisation have been extensively investigated by molecular dynamics simulations [22, 23], and independently rationalised by a continuum diffusion model based on the Smoluchowski equation [24], a discrete stochastic model [25] and a general kinetic model [26]. It is therefore highly desirable to develop an experimental model system in which the effect of binding sites and conformational changes can be directly probed in channel transport.

One option is studying the transport of colloidal particles across microfluidic channels. The suitability of colloids and channels as a model for membrane transport lies in a number of their intrinsic properties. Firstly, colloidal particles undergo Brownian motion as solutes in a cellular environment. Secondly, the size of colloidal particles is on the length scale of μm which can be experimentally observed under an optical microscope. Thirdly, the diffusion time scales of colloidal particles are on the order of seconds which can be recorded with ease. Furthermore, colloidal particles can be directly manipulated by various sources, such as electrical, magnetic, gravitational and optical methods [27–30]. Therefore, we study binding-site effect in a synthetic membrane system composed of colloidal suspensions and microfluidic channels. Particles are confined to single-file diffusion in the channel, which is close to the realistic situation in natural channels and pores [31–34], and also makes our result comparable with theoretical studies based on one-dimensional transport [24, 35–37].

We build up Holographic Optical Tweezers (HOTs), which are used to modulate the energy landscape in the synthetic membrane system. Optically modulated potentials have been employed to study particle diffusion [38, 39], to induce thermal ratchets [40, 41] to direct [42] and sort Brownian particles [43–47], to study particle escape and synchronization [48] and to investigate stochastic resonance and resonant activation [49, 50]. As demonstrated

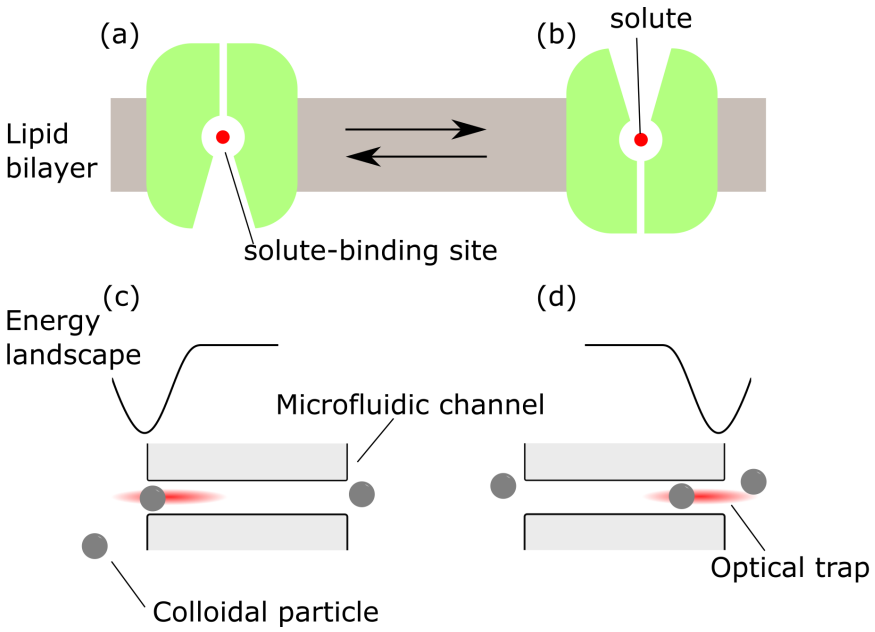

Fig. 1.2 Comparison between a protein transporter and a synthetic membrane model. (a,b) are modified from Fig. 11-3 in literature [8]. A transporter alternates between two conformations with binding sites exposed sequentially to one side of the bilayer. (c,d) An energy landscape fluctuating in the colloidal channel model system which simulates the 'open' and 'close' of the channel. Holographic optical tweezers are used to modulate the energy landscape.

by a previous work in our group, optical traps generated by the HOTs attract particles to diffuse into the microfluidic channel, which is relevant to the binding between the membrane channels and solutes [51, 52]. Inspired by the conformational changes observed in protein transporters, the study of particle transport across a channel is extended to the transport under a time-dependent energy landscape. As shown in Fig. 1.2, an energy well placed at the channel entrance attracts particles to diffuse into the channel, which simulates the 'open' state of the channel in the concept of energy landscapes. Meanwhile, a deep energy barrier which impedes transport of particles, simulates the 'closed' state of the channel. Although matching a complicated protein structure at the atomic level to a simplified channel geometry involves a certain degree of arbitrariness, our results provide guidelines to design artificial membranes with optimal performances from a biomimetic perspective.

1.4 Scope of this thesis

In this thesis, particle transport across a channel via modulated energy landscapes is investigated. A synthetic membrane system composed of colloidal particles and microfluidic channels is built up. HOTs are used to modulate the energy landscape in channels. In the

following chapters, the intensity distribution of optical traps is calibrated to estimate energy landscapes. The Local Transition Probability (LTP) of particles is used to reconstruct energy landscapes under non-equilibrium conditions. This method is further combined with the intensity distribution calibration to resolve energy landscapes in a complex environment. With an accurate knowledge of the energy landscape, the effect of an oscillating energy landscape on particle transport across a channel is studied. By monitoring the movement of particles, an optimal oscillation frequency which significantly enhances the translocation rate of particles is demonstrated and understood by diffusion theories.

The theoretical background behind this work is presented in Chapter 2. The Langevin equation is used to describe the motion of a colloidal particle undergoing Brownian motion in a modulated potential energy landscape. The Fokker-Planck (FP) equation is used to describe the Probability Density Function (PDF) of positions of Brownian particles. The mean exit time is introduced and the PDF is used to reconstruct the energy landscape, which works at equilibrium. To resolve an energy landscape under non-equilibrium conditions, the concept of Splitting Probability (SP) is introduced and used to calculate the underlying energy landscape experienced by particles. At the end of this chapter, the idea of driving a particle by external forces to map an energy landscape is discussed with the theoretical basis laid out.

A synthetic membrane experimental system is built up in Chapter 3. The concept of holographic optical trapping is first explained following the building and alignment of the setup. The procedure of making a microfluidic sample with colloidal suspensions is described. Then, trajectories of particles are extracted with the particle concentration estimated.

Having established the theoretical and technical basis for the experiment, Chapter 4 describes the reconstruction of potential energy landscapes. While the PDF method exhibits the features of the energy landscape accurately at equilibrium, it fails to rebuild the energy landscape with high barriers where transitions of particles rarely happen. However, deep energy wells and high barriers are needed to simulate the open and closed states of a channel. Therefore, the optical intensity is calibrated with the PDF method and used to estimate energy landscapes with high barriers. The calibration result is further validated by dragging a particle through the energy landscape. Meanwhile, all the potential reconstruction methods discussed so far fail in systems out of equilibrium. The SP is in general applicable for both equilibrium and non-equilibrium situations, but requires a large ensemble of trajectory data. We develop a new method using LTP which improves the robustness of the result compared to the SP method. The LTP method also provides error estimations which are not accessible in the PDF and LTP approaches. The LTP method is further combined with the calibration method to characterise the energy landscape in a more complex and realistic environment.

Finally, in Chapter 5, particle transport across a channel under an oscillating potential is studied. The potential is first oscillated deterministically. An optimal oscillation frequency is found which maximises the translocation rate of particles across the channel. The translocation rate is enhanced about one hundred times compared to the transport in a channel without external potentials. This optimal frequency is understood by calculating the mean exit time and solving the FP equation numerically. In the very end, the influence of a potential oscillating stochastically based on exponential distributions on particle transport is probed. The result sheds lights on further study of stochastic gating found in ion channels.

Chapter 2

Theoretical background

This thesis studies transport of colloidal particles across a modulated potential energy landscape. In this chapter, the theoretical background for the experimental work is laid out. A Langevin equation is first written for motion of particles diffusing in a modulated energy potential. Then the theoretical basis of direct transition time in a modulated potential energy landscape is introduced. In order to map the modulated energy potential, two standard methods using trajectories of particles, i.e. probability density function and splitting probability are discussed. In the end, the velocity of particles driven by an external force is also used to reconstruct the underlying energy landscape.

2.1 Langevin equation

The motion of a small particle suspended in a solvent is determined by the total force acting on it, described by Newton's Second Law:

$$\Sigma \mathbf{F}_i = m\frac{d^2\mathbf{r}}{dt^2} \tag{2.1}$$

where $\Sigma \mathbf{F}_i$ is the total force acting on the particle by fluid molecules, m is the mass of the particle and $\mathbf{r}$ is the particle position in three dimensions. In this thesis, only one-dimensional (1D) movement along x is considered so the vector sign is dropped in future discussions. It is impossible to write down each F_i in Eq. 2.1 without the knowledge of initial positions and velocities of those molecules, which is on the order of 10^{23} (the Avogadro constant). However, the total force ΣF_i acting on the particle can be decomposed into a viscous force F_v, due to the movement of the particle in the solvent, and a fluctuating force $\xi(t)$. The viscous

force F_v is proportional to the velocity of the particle according to Stokes' law

$$F_v = \zeta \frac{dx}{dt} \tag{2.2}$$

Here, ζ is the friction coefficient of the particle in the solvent, with $\zeta = 6\pi\eta a$ for a particle with radius a in a bulk solution with viscosity η.

The fluctuating force $\xi(t)$ is a random force with zero mean $\langle \xi(t) \rangle = 0$, which is uncorrelated with the actual particle position $\langle \xi(t)x(t) \rangle = 0$, and known as Brownian noise. The relaxation time of solvent molecules (10^{-14} s) is significantly shorter than the relaxation time of particles used in our experiment (10^{-8} s), so it is reasonable to state that $\xi(t)$ is fluctuating much faster than the particle position, such that

$$\langle \xi(t)\xi(t') \rangle = 2\zeta k_B T \delta(t - t') \tag{2.3}$$

where k_B is the Boltzmann constant, T is the absolute temperature and $\delta(t)$ is the Dirac delta function.

By specifying the two kinds of force, Eq. 2.1 can be written as

$$m\frac{d^2x}{dt^2} = -\zeta \frac{dx}{dt} + \xi(t) \tag{2.4}$$

which describes the force and motion relation for a particle suspended in a solvent.

Here, we introduce Reynolds number (Re) which is the ratio of inertial forces to viscous forces acting on an object moving in a fluid, calculated by $Re = \rho v a/\eta$. For the colloidal system used in this thesis, $Re \approx 2.5 \times 10^{-7}$ is obtained by considering the particle radius $a = 255$ nm, a typical particle speed $v = 1\ \mu m/s$, solvent density $\rho = 1 \times 10^3$ kg m^{-3} and viscosity $\eta = 1 \times 10^{-3}$ Pa s. In a fluid environment with $Re \ll 1$ where the particle is over damped, the inertial term d^2x/dt^2 in Eq. 2.4 can be ignored. The most simplified Langevin equation is

$$\zeta \frac{dx}{dt} = \xi(t) \tag{2.5}$$

which is the equation of motion for a particle undergoing Brownian motion in suspension for a time scale longer than the relaxation time of the solvent. In the presence of a modulated potential energy landscape $U(x)$, the particle experiences a force as

$$F(x) = -\frac{dU(x)}{dx} \tag{2.6}$$

which further influences the motion of the particle. With an additional potential, the Langevin equation is written as

$$\zeta \frac{dx}{dt} = -\frac{dU(x)}{dx} + \xi(t) \tag{2.7}$$

This equation describes the motion of a Brownian particle in an arbitrary energy potential. It will be used to understand the particle transport in an optically modulated potential in this thesis. Particularly, the Langevin equation is used as the theoretical foundation of the Brownian dynamics simulations conducted in Chapter 4 and 5.

2.2 Mean exit time and direct transition time

The Langevin equation and its solution explain Brownian motion in terms of random walks. Meanwhile, the probability density distribution $p(x,t)$ of the ensemble of Brownian particles can be described by the Fokker-Planck (FP) equation

$$\frac{p(x,t)}{\partial t} + v\frac{\partial p(x,t)}{\partial x} = D\frac{\partial^2 p(x,t)}{\partial x^2} \tag{2.8}$$

where v is the velocity of drift and D is the diffusion coefficient of the particle in the solvent, which relates to ζ through $D = k_B T/\zeta$. The FP equation can be solved analytically for simple external forces [53]. When the external driving force is complicated, it can be solved numerically by modern mathematical tools, for example *Wolfram Mathematica*. It is used to understand the diffusion process in an oscillating potential in Chapter 5.

The FP equation expresses the evolution of the single particle density in an ideal 1D infinitely long channel. By starting particles at an initial position, $p(x,0) = \delta(x)$ without considering particle interactions and drift flow, the solution of Eq. 2.8 is

$$p(x,t) = \frac{1}{\sqrt{4\pi D t}} \exp\left(-\frac{x^2}{4Dt}\right) \tag{2.9}$$

Differentiating Eq. 2.9 by time t, one can get the mean first passage time:

$$< t >= \frac{x^2}{2D} \tag{2.10}$$

which is the averaged diffusion time for particles starting at position 0 to cross a distance x in an infinitely long channel.

2.2.1 Mean exit time

Eq. 2.10 provides us with a good intuition for how long it takes a particle to diffuse over a distance. However, channels in reality are never really infinite. In the diffusion system studied in this thesis, colloidal particles are undergoing Brownian motion in a 1D channel, as sketched in Fig. 2.1(a). Absorbing boundaries are used to describe the channel ends a and b [dashed lines in Fig. 2.1]. The movement of a particle is terminated once it reaches a or b. The particle movement along the channel longitudinal direction is denoted as x, which is plotted in Fig. 2.1(b) along the diffusion time t. In this case, x ends when the particle touches absorbing boundary b.

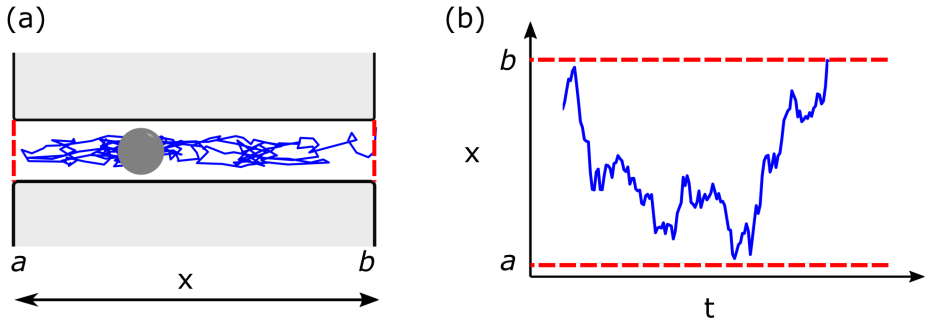

Fig. 2.1 A Brownian particle diffusing in a 1D channel. (a) Sketch of a particle diffusing in a 1D channel with absorbing boundaries a and b (dashed lines) overlapping with positions of the particle. (b) The movement of the particle on x direction is plotted against the diffusion time t. x terminates once the particle reaches one of the absorbing boundaries.

The splitting probability $\pi(x)$ is defined as the probability of a particle starting at $x \in [a,b]$ to reach a before reaching b. By using the Laplace transform of Eq. 2.8, the splitting probability $\pi(x)$ of a particle starting at position x_0 in a channel of length L is given by [54]

$$\begin{aligned} \pi_-(x_0) &= 1 - \frac{x_0}{L} \\ \pi_+(x_0) &= \frac{x_0}{L} \end{aligned} \tag{2.11}$$

where $\pi_-(x_0)$ and $\pi_+(x_0)$ denote the probability that the particle reaches the left end a or the right end b.

The mean first exit time to absorbing boundaries can then be written down as [54]

$$\begin{aligned} \langle t(x_0)\rangle_- &= \frac{L^2}{6D}\mu_0(2-\mu_0) \\ \langle t(x_0)\rangle_+ &= \frac{L^2}{6D}(1-\mu_0^2) \end{aligned} \tag{2.12}$$

where $\mu_0 = x_0/L$ with the initial particle position at x_0 in a channel of length L.

The unconditional mean exit time, which is independent of which end the particle trajectory terminates at is the weighted average of the first exit time [54], given by

$$\begin{aligned}\langle t(x_0)\rangle &= \pi_-(x_0)\langle t(x_0)\rangle_- + \pi_+(x_0)\langle t(x_0)\rangle_+ \\ &= \frac{L^2}{2D}\mu_0(1-\mu_0)\end{aligned} \tag{2.13}$$

The mean exit time gives us a better description of the time a particle takes to escape a channel of finite length than Eq. 2.10.

2.2.2 Direct transition time

In a more specific situation, in which the particle starts at one absorbing boundary and reaches the other, the mean exit time in Eq. 2.12 can be written as:

$$T_{tr} = \frac{2L^2}{3D} \tag{2.14}$$

where the channel begins at $-L$ and ends at L. In this case, the mean exit time is the direct transition time T_{tr}, which is the time a particle goes from one boundary of the interval to the opposite end without retouching the starting point [37].

In the presence of an external potential $U(x)$ in the channel, the direct transition time within two perfect absorbing boundaries is given by [37, 55]:

$$T_{ext} = \frac{1}{D}\frac{\int_a^b (\int_a^x \mathrm{e}^{\beta U(y)}\mathrm{d}y)(\int_x^b \mathrm{e}^{\beta U(y)}\mathrm{d}y)\mathrm{e}^{-\beta U(x)}\mathrm{d}x}{\int_a^b \mathrm{e}^{\beta U(y)}\mathrm{d}y} \tag{2.15}$$

where $[a,b]$ is the diffusion region, $\beta = (k_B T)^{-1}$ with k_B and T denoting the Boltzmann constant and temperature as discussed previously. With the knowledge of the energy potential $U(x)$ and diffusion coefficient D, T_{ext} is calculated and compared to experimental results in Chapter 5.

2.3 Reconstructing the energy potential

The FP equation can be solved with an accurate knowledge of the underlying free energy landscape $U(x)$. $U(x)$ also relates to the direct transition time of a Brownian particle in the channel. Therefore, access to $U(x)$ is of fundamental importance. Note here, the untracked

spatial dimensions y and z remain constant in our 1D channel system therefore $U(x)$ refers to the potential energy landscape in the future discussion [29, 56].

2.3.1 Probability density function

The Probability Density Function (PDF) is one of the most commonly used methods to resolve potential energy landscape under equilibrium conditions [57, 58]. The probability that an equilibrium system is in state s at temperature T is given by the Boltzmann distribution

$$p(s) = \frac{1}{Z} \exp\left(\frac{-U(x)}{k_B T}\right) \tag{2.16}$$

where Z is the partition function. Take a particle of mass m moving in 1D for example, the state s is defined by the particle position x and the particle velocity v so that $E_s = U(x) + \frac{1}{2}mv^2$ [1]. Here,

$$p(s) = \exp\left(\frac{-U(x)}{k_B T}\right) \exp\left(\frac{-\frac{1}{2}mv^2}{k_B T}\right) \tag{2.17}$$

which infers to $p(s) \propto \exp(-U(x)/k_B T)$. As sketched in Fig. 2.2(a), the PDF of particles eventually settles down to a Boltzmann distribution that directly reflects the underlying potential energy landscape in a sparsely populated system [51, 57, 58]. However, the PDF method becomes impractical while mapping an energy landscape with an high energy barrier. In the situation plotted in Fig. 2.2(b), the energy barrier impedes the movement of particles which results in a biased sampling of the position histogram within the measurement time. Meanwhile, an evenly flat distribution of particle positions can be mapped in the presence of a hydrodynamic flow, as illustrated in Fig. 2.2(c). The distribution here does not reflect the underlying energy landscape with an external force. Overall, the PDF is useful but limited to characterise energy landscapes without high barriers at equilibriums.

2.3.2 Splitting probability

The splitting probability (SP) has been defined in Section 2.2.1. In a potential energy landscape, the probability of a particle starting at x to first reach the left or right boundary is denoted as $\pi_-(x)$ and $\pi_+(x)$ as sketched in Fig. 2.3(a). In a double well energy landscape, $\pi_+(x)$ measured from trajectories of 200 simulated Brownian particles is reported in Fig. 2.3(b). The detail of the simulation will be described in Chapter 4. Given a time-stationary $U(x)$, $\pi(x)$ of an overdamped particle can be derived analytically from Eq. 2.8.

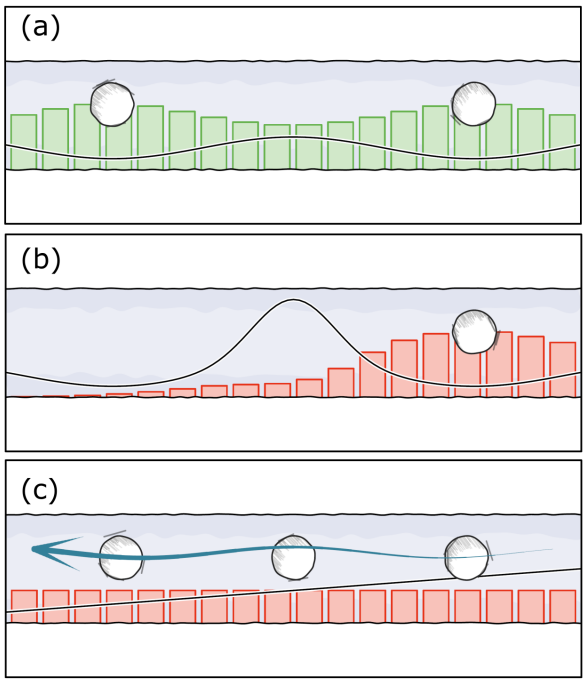

Fig. 2.2 Distribution of particle positions in different environments. (a) The distribution of particle positions (bars) in equilibrium systems reflects the underlying energy landscape (solid line). (b) The distribution of particle positions can be biased with a high energy barrier where few or no particle transitions happen within the measurement time. (c) In the presence of a hydrodynamic flow, a flat distribution of particle position does not reflect the underlying energy landscape. Note: Figure modified from the original plot by Dr. Sebastian Sturm.

Assuming a spatially constant diffusion coefficient $D(x) \equiv D$ [59],

$$\pi(x) = \frac{\int_x^b e^{U(x)/k_BT} dx}{\int_a^b e^{U(x)/k_BT} dx} \tag{2.18}$$

Inverting Eq. (2.18) allows us to obtain an estimate of the underlying energy potential, denoted as $U_{SP}(x)$, read as

$$U_{SP}(x) = \beta^{-1} \ln\left(-D\frac{d\pi(x)}{dx}\right) \tag{2.19}$$

where $\beta = (k_BT)^{-1}$.

The SP has been recently proposed as an alternative method to reconstruct potential energy landscapes from trajectories of Brownian particles [60]. Compared to the PDF method, $U_{SP}(x)$ is able to exhibit non-equilibrium force in a potential energy landscape due to the fact that $\pi(x)$ contains the information of preferred moving direction of particles.

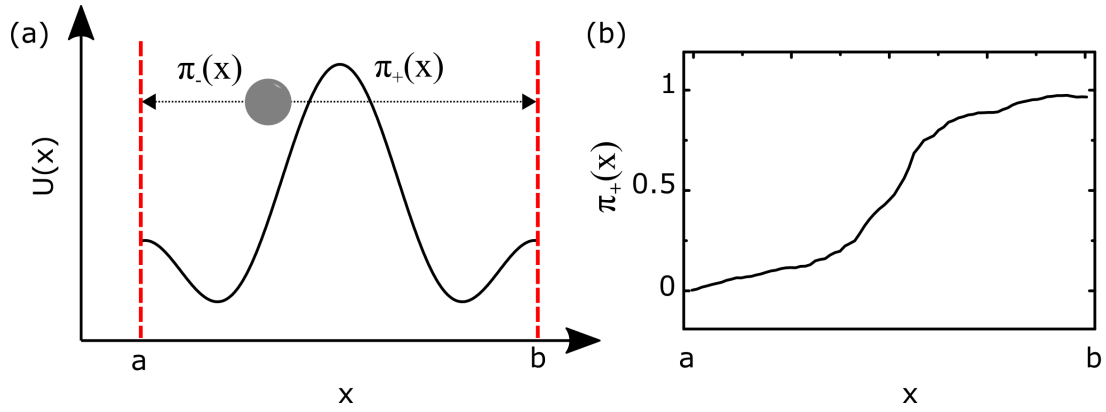

Fig. 2.3 Splitting probability of a particle diffusing in a potential energy landscape. (a) A particle is diffusing within two absorbing boundaries a and b. $\pi_-(x)$ is the probability that a particle starts at x reaches a before it reaches b. $\pi_+(x)$ is the probability to touch b before it gets to a. (b) $\pi_+(x)$ calculated from trajectories of 200 simulated Brownian particles diffusing in a double well energy landscape plotted in (a).

However, a large number of trajectory ensemble is required in this method due to the differential operation in Eq. 2.19 which outputs a significant amount of noise with a non-smooth $\pi(x)$ profile. Meanwhile, the SP method suffers the same problem as the PDF method in the face of a high energy barrier. The low probability of a particle jumping through an energy barrier results in a constant $\pi(x)$ which cannot be used to generate a valid $U_{SP}(x)$ via Eq. 2.19. Both the PDF and the SP methods are employed to reconstruct potential energy landscape in Chapter 4.

2.3.3 Mapping energy potentials by driving particles

In order to map an energy landscape with high barriers, an external driving force F_{drive}, which is larger than the maximum of dU/dx can be applied to drag a Brownian particle [61, 62]. In this case, the Langevin equation with an imposed energy landscape (Eq. 2.7) can be expanded as

$$\zeta \frac{dx}{dt} = F_{drive} - \frac{dU(x)}{dx} + \xi(t) \tag{2.20}$$

Considering the particle is moving at a high driving speed allows us to omit the fluctuating force $\xi(t)$ in Eq. 2.20. Therefore by measuring the particle velocity $v(x)$, the potential $U(x)$ can be deduced as follows

$$U(x) = \int \left(\frac{F_{drive}}{\zeta} - v(x) \right) dx \tag{2.21}$$

with a contribution from F_{drive} to $v(x)$ through the Stokes' equation (Eq. 2.2). This way to resolve $U(x)$ is extremely useful for energy potentials with high barriers where transition events rarely happen within the experimental time scale.

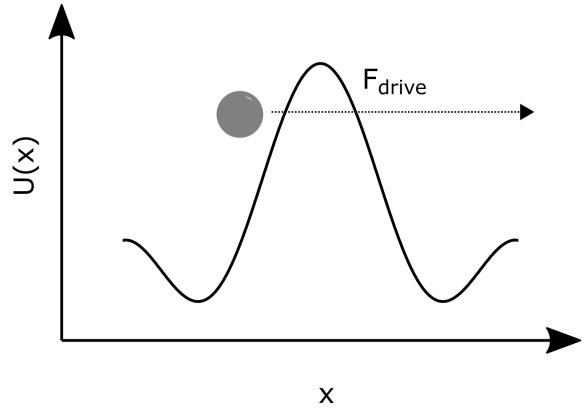

Fig. 2.4 Sketch of driving a particle through a potential energy landscape by an external force F_{drive}.

In addition to this driving method, there is another way to reconstruct an optically induced potential from the intensity distribution, which will be applied and compared with other methods in Chapter 4.

2.4 Conclusion

The motion of particles diffusing in a potential energy landscape can be described by the Langevin equation and the FP equation. The theoretical basis of Brownian motion will be used to conduct simulations and help us to understand the dynamics of particle transport across a finite channel. The potential energy landscape in a 1D system can be mapped by the PDF method at equilibrium and the SP method under non-equilibrium conditions. In the face of a potential landscape with high energy barriers, driving a particle out of the energy minimum provides another way to infer the underlying potential landscape which is inaccessible to the SP and PDF method.

Chapter 3

Experimental methods

A synthetic membrane system which consists of colloidal particles and microfluidic channels is built up to study transport in modulated potential energy landscapes. Holographic optical tweezers are used to generate optical potentials in channels. The transport of colloidal particles in channels is recorded and analysed to understand the effect of modulated energy landscapes. In this chapter, the concept of optical tweezers is first introduced. The details of setting up the holographic optical tweezers are described with notes for alignment. After that, the fabrication process of microfluidic structures is reviewed, followed by steps to make Polydimethylsiloxane samples. In the end, data analysis methods are discussed in the order of tracking particles, calculating diffusion coefficient and estimating particle concentrations.

3.1 Introduction

Manipulating micro dielectric particles by focused laser beams was first achieved by Arthur Ashkin in 1970 [56] and was recently awarded Nobel Prize in Physics. Since then, optical trapping has been realised by different optical techniques and applied in a wide range of studies [63, 64]. Specifically, optical tweezers have been used to modulate potentials in various systems due to their ability to produce a large range of force and their flexibility to be controlled in real time. Colloidal particle experimental systems are well established due to their accessibility in time and length scales and their versatility for influencing with different sources of forces [30, 65]. Inspired by the binding sides observed in membrane proteins, we combine optical tweezers and colloidal suspensions to study the effect of modulated potentials on particle transport.

3.2 Principle of holographic optical trapping

Optical trapping is achievable due to the fact that the trapped object has a different refractive index to its surrounding environment. A proper explanation of optical traps relies on solving Maxwell equations, which involves complex calculations. However, an intuitive explanation of the trapping effect can be given using ray optics where the trapped object is significantly larger than the wavelength of the laser. In ray optics, light is refracted while passing through a colloidal particle because the particle has a higher refractive index than the solvent, mostly water. The change in the light direction induces a force which exerts on the particle due to the momentum conservation. Most optical traps are generated by a Gaussian beam which has a high light intensity in the beam centre. Once the particle is not aligned in the central axis of the beam, the central ray causes a larger force F_2 than the ray closer to the edge of the beam F_1 as sketched in Fig. 3.1(a). Overall, a net 'gradient' force F_{net} drags the particle towards the beam centre. Meanwhile, the light also transfers momentum to the particle by backscattering at the solvent-particle interface, which results in a 'scattering' force along the light propagation direction. When the particle is downstream offset from the beam waist as shown in Fig. 3.1(b), the 'scattering' force is balanced by the 'gradient' force F_{net} and the particle can be firmly trapped near the beam waist [1].

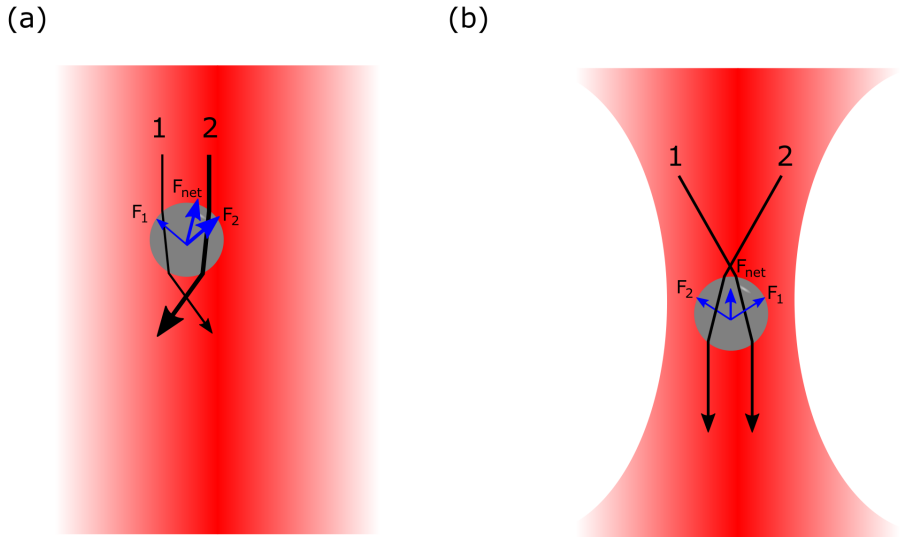

Fig. 3.1 Schematic of the principle of optical trapping in ray optics. (a) In a Gaussion beam profile, particle off-centred is forced to the beam central axis by the gradient force. (b) In a focused beam, the scattering force balances the gradient force on the particle while it is offset downstream from the beam waist.

Optical tweezers have the capability of trapping micron-scale objects, but it involves a substantial amount of effort if one wants to move the trapped object by either moving the sample stage where the actual position of the trap stays or steering the optical beam to change the trapping position. Here, a computer controlled Diffractive Optical Element (DOE) makes it possible to control the position of an optical trap easily and generates multiple traps simultaneously. Specifically, a Spatial Light Modulator (SLM) is used as the DOE in Holographic Optical Tweezers (HOTs) setup, which is able to modulate the amplitude or the phase of a transmitted or reflected light beam.

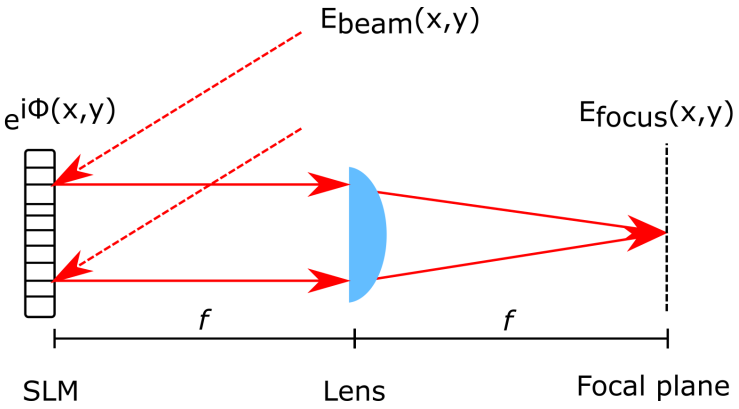

Fig. 3.2 Working principle of HOTs. The incoming laser beam $E_{beam}(x,y)$ is reflected by the SLM with phase modulated by $e^{i\Phi(x,y)}$. The SLM is positioned at the front focal plane of the lens. At the back focal plane of the lens, $E_{focus}(x,y)$ is the Fourier transform of $e^{i\Phi(x,y)}E_{beam}(x,y)$. f denotes the focal length of the lens.

The basic working principle of HOTs is explained as follows, based on a phase-modulated SLM working in a reflection mode (illustrated in Fig. 3.2). At the beginning, an incoming laser beam, denoted as $E_{beam}(x,y)$ is shining on a SLM. For simplicity, $E_{beam}(x,y)$ is assumed to have a uniform distribution in phase. A hologram $\Phi(x,y)$, which is essentially a grey scale image is loaded on the reflection area of the SLM. Two sample holograms used to generate line traps and point traps are shown in Fig. 3.3(a,b). These holograms are calculated based on superposition of light field corresponding single traps [66] and the algorithm has been readily implemented in *Red Tweezers* [67], a *Labview* based program. Each pixel on the SLM causes individual change to the phase of the reflected light. After reflection, the electric field of the beam is modified to $e^{i\Phi(x,y)}E_{beam}(x,y)$. The SLM is placed at the front focal plane of the convex lens. The lens collects the diffracted beam from the SLM and focuses it to the back focal plane, denoted as $E_{focus}(x,y)$ which is the Fourier transform of $e^{i\Phi(x,y)}E_{beam}(x,y)$ [1]. The whole process can be calculated by Fresnel diffraction integral [1] by inputting a Gaussian beam profile with the phase change $e^{i\Phi(x,y)}$. By putting holograms shown in Fig. 3.3(a,b) into a Fresnel diffraction process, we obtained the corresponding

electric field at focal domain or in other words the generated optical traps in Fig. 3.3(c,d) respectively. Note here, the zeroth order of the diffraction is omitted deliberately to show the high order diffractions. In the experimental setup described in the following section, we manage to monitor the intensity distribution of the optical trap. The recorded intensity distribution (Fig. 3.3(e,f)) matches the calculated first order of diffraction (Fig. 3.3(c,d)) qualitatively.

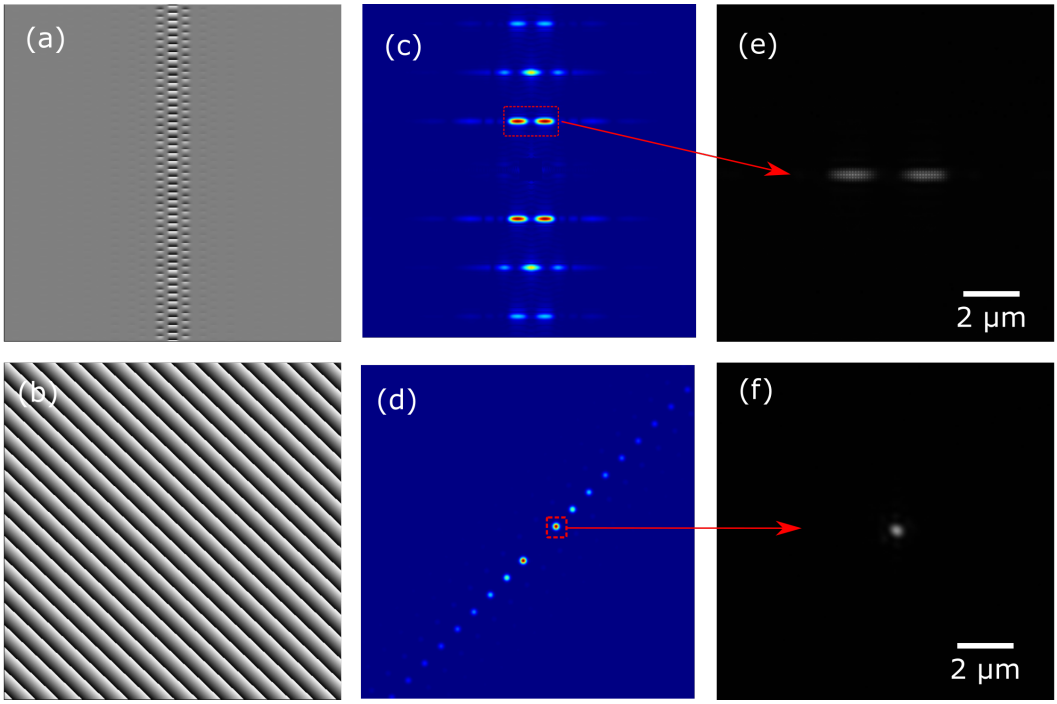

Fig. 3.3 Holograms and the corresponding intensity distributions of optical traps. (a,b) The specific hologram is calculated and displayed on the SLM. (c,d) Calculated intensity distributions of optical traps generated by the holograms in (a,b). The zeroth order of the diffraction is omitted deliberately to show the high order diffractions. (e,f) The first order of the diffraction captured by an infrared camera in our experiment.

3.3 Experiment methods

3.3.1 Building holographic optical tweezers

We built HOTs[1] (sketched in Fig. 3.4 and photograph in Fig. 3.5) based on the configuration proposed in [64]. Details of the components are listed in Appendix A. Briefly, a laser beam with a wavelength of 1064 nm transmits through a polarisation beam splitter (PBS) and a

[1]The building and alignment of HOTs was carried out with Mr. Jannes Gladrow.

half wavelength ($\lambda/2$) plate, which is used to control the beam intensity by rotating the orientation of the $\lambda/2$ plate. The laser beam is then expanded 5 times through lenses L1 and L2 to overfill the reflection area of the SLM. A $4f$ optical system consisting of SLM, L3, L4 and the objective conjugates the phase modulated light to the back aperture of the objective. Pinhole P2 is placed at the focal plane between L3 and L4 to block the zeroth order diffraction, which is essentially a spot. The back aperture of the objective is positioned on the end of the $4f$ system which further focuses the laser beam into our microfluidic channels. A collimated illumination made up by L7 and L8 is shining on the top of the microfluidic sample. The image of the sample is collected by the same objective and recorded by a fast camera (Camera1). Camera2 and a pellicle BS2 are used to monitor the back scattering of the optical trap from the cover glass. In order to monitor the intensity of the generated optical traps, a second $4f$ system is built by L3 and L9 with 2% of the laser beam split by a pellicle beam splitter BS1 from the main $4f$ path. The laser traps are then focused and monitored by Camera3.

3.3.2 Alignment of the holographic optical tweezers setup

The HOTs set up in our lab is made up of more than forty optical components. Careful and correct alignment ensures trapping of micron sized particles in three dimensions and avoids unintentional force gradients in generated traps. We summarise the following key steps in the alignment process, although they are not the only ones worth attention,

1. The back aperture of the objective should be placed exactly at the end of the $4f$ system to ensure that the generated optical traps are the Fourier transform of the laser beam reflected by the SLM. A misplacement of objective on the $4f$ will end up with fractional Fourier transform, which produces undesired optical distributions.

2. The back aperture of the objective should be overfilled by the incident laser beam to generate a large enough gradient force to trap a particle. Otherwise, particles may be pushed away by the optical trap due to an overwhelming scattering force.

3. The output beam from the expander and $4f$ system should be accurately collimated. A beam profiler is used to make sure the beam size stays constant while propagating. Pinholes are easy to implement but they are not accurate enough to check the collimation of beams.

4. The back scattering of an optical trap from the cover glass should be a symmetric four-lobe pattern, as shown in Fig. 3.6. The intensity distribution of the back scattering is dependent on the distance z between the objective pupil and the cover glass as shown in Fig. 3.6(a,b). However, the centre of mass of the pattern should be independent in z and a good alignment example is shown in Fig. 3.6(c). By contrast, a changing centre of mass along z indicates misalignment between the beam and the objective axes [1].

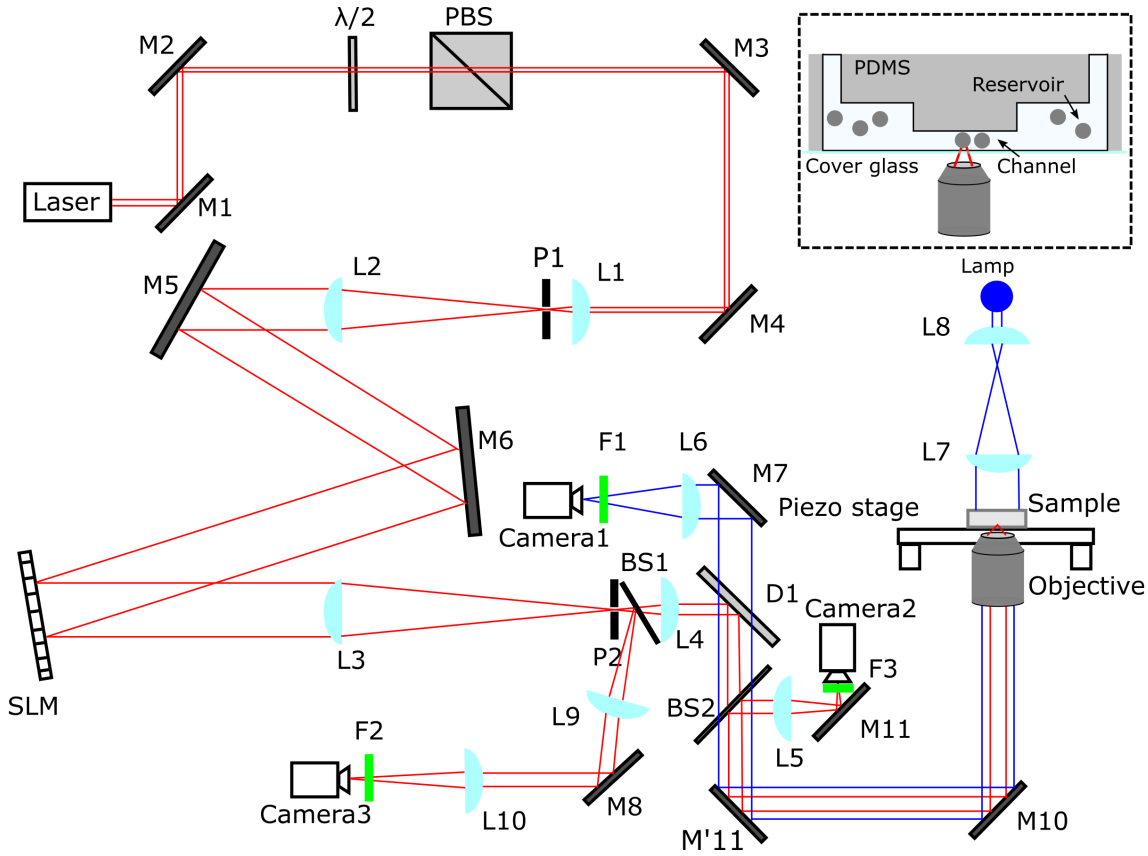

Fig. 3.4 Schematic of the HOTs setup. M1-M10: AR-coated dielectric mirrors. PBS: Polarizing beamsplitter cube. $\lambda/2$: Half wavelength plate. P1,P2: Iris. L1-L10: Plano-convex lens. SLM: Spatial Light Modulator. F1-F3: Bandwidth filter. D1: Dichroic mirror. BS1-BS2: pellicle. Details of the components are listed in Table. 3.1 in Appendix.A . The inset shows the optical trap is focused into the microfluidic channel to manipulate colloidal particles, which is not to scale.

5. The output power of the laser can be controlled by the laser driver or by adjusting the orientation of the $\lambda/2$ plate. However, the actual laser power focused into the sample is hard to estimate. We measured the laser power at the position of the objective's back aperture via a power meter, result shown in Fig. 3.7(a). The readout is sensitive to the hologram loaded on the SLM and varies between different trap configurations. The actual power arriving into the sample should also consider the absorption by the objective which is 66% at 1064 nm, the absorption by the immersion oil and the reflection from the cover glass.

6. The position of the objective is fixed on our HOTs setup to minimise focus drift. The whole optical path is enclosed and built on an air damped optical table. However, we still find the position of a stationary optical trap strongly correlated with the lab temperature, with measurement shown in Fig. 3.7(b).

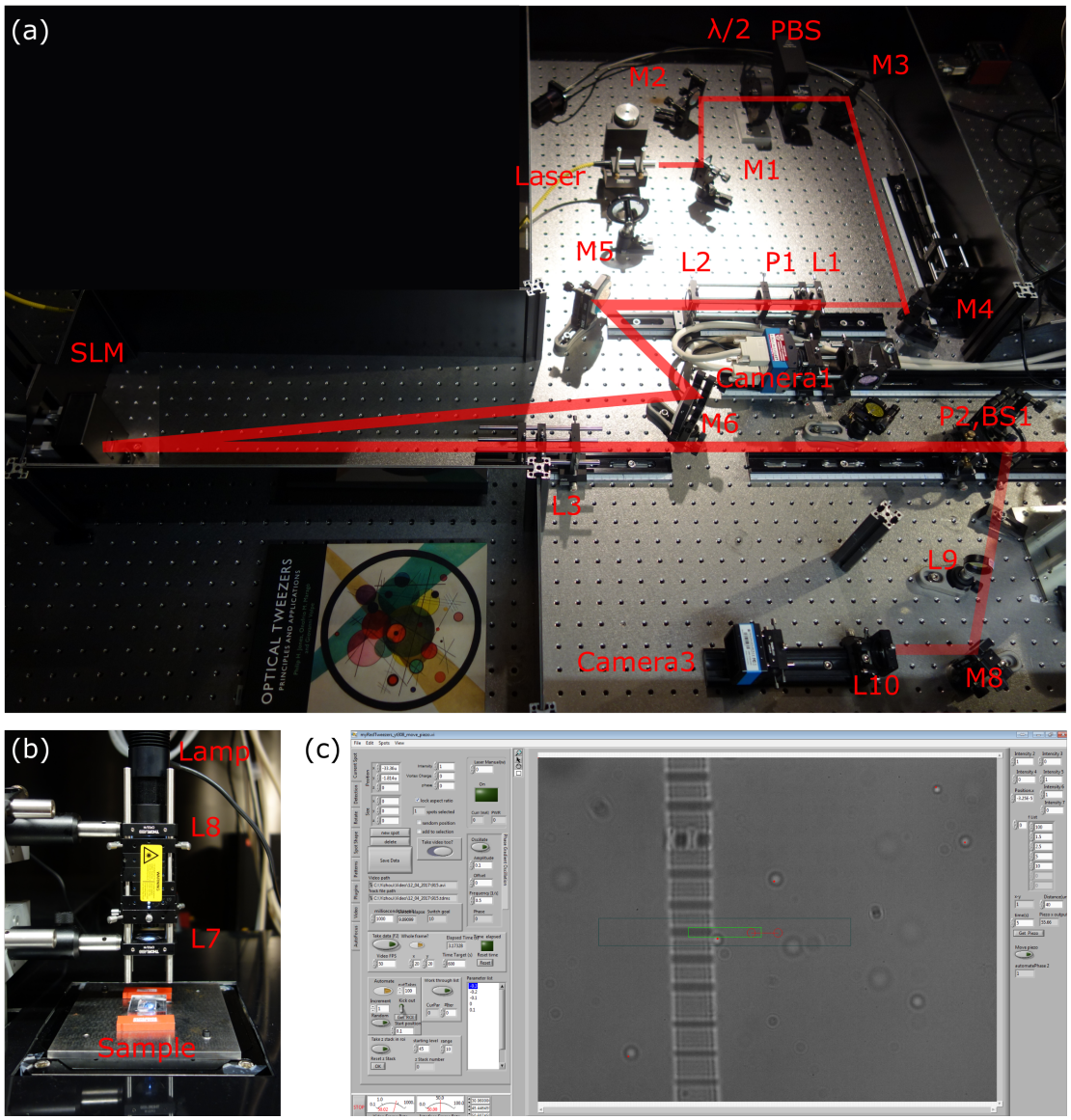

Fig. 3.5 Photograph of the HOTs setup. (a) The laser, beam expander and the $4f$ configurations for holographic optical trapping. Components are labelled corresponding to Fig. 3.4. Photograph was taken without enclosure for clarity. (b) The Piezo stage, sample holder and a microfluidic sample under illumination. (c) Screen shot of the HOTs control software which is developed basing on *red tweezers* [67].

By carefully aligning the HOTs setup, we manage to trap not only Polystyrene particles with diameter down to 300 nm but also gold particles of diameter of 80 nm in three dimensions. The HOTs are used to modulate energy landscapes in the microfluidic domain in the rest of the thesis.

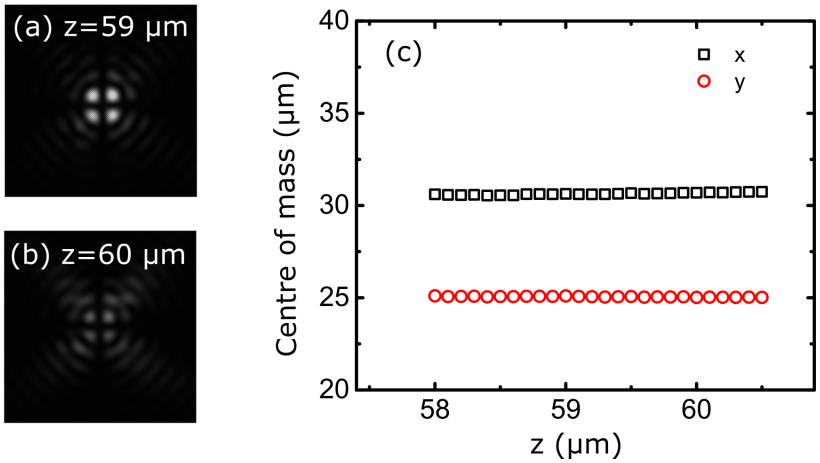

Fig. 3.6 Back scattering of an optical trap from the cover glass. (a,b) Image of the back scattering of an optical trap taken at two different z, which is the distance between the cover glass and the objective pupil, recorded by Camera2. (c) The centre of mass of the back scattering measured by scanning the distance z by moving the Piezo stage.

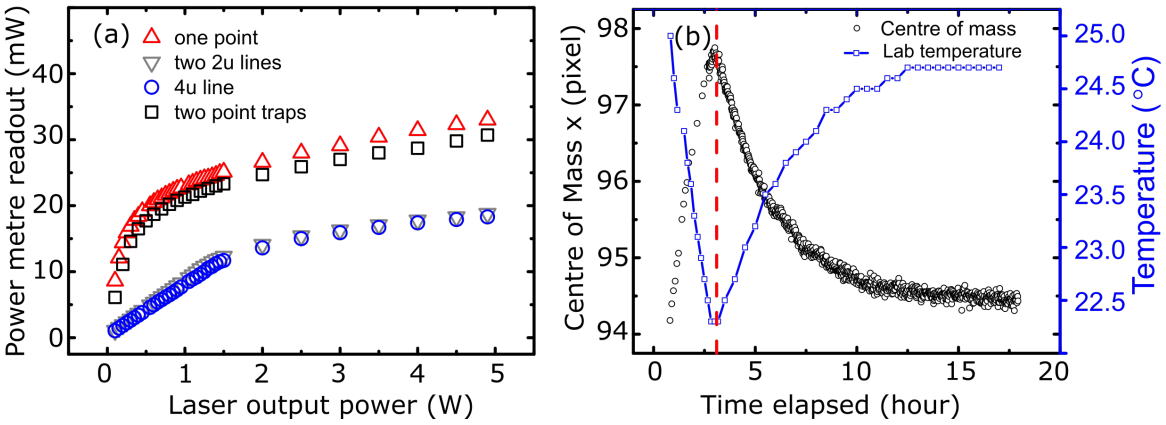

Fig. 3.7 Output power of the HOTs and the effect of temperature on the position of an optical trap. (a) Laser power measured at the position of the back aperture of the objective by a power meter. (b) Correlation between lab temperature and the centre of mass of an optical trap recorded by Camera3. The dashed line indicates the time when the aircon in lab was switched off.

3.3.3 Fabrication of the sample cell[2]

A mould for making microfluidic chips is fabricated in two steps [68, 69]: firstly, platinum micro-wires are fabricated on a silicon wafer via a focused ion beam assisted deposition as

[2]Part of this section has been published as **Diffusion coefficients and particle transport in synthetic membrane channels** Stefano Pagliara, Simon Dettmer, Karolis Misiunas, Lea Lewis, Yizhou Tan, Ulrich F. Keyser, *The European Physical Journal Special Topics*, 14(223), 3145-3163 (2014).

shown in Fig 3.8(a). An organometallic precursor is decomposed by the ion beam resulting in platinum atoms being deposited and the organic fragments being exhausted. Secondly, polymer micro-chambers are fabricated by photolithography as shown in Fig 3.8(b). A 10 μm thick layer of photoresist (AZ 9260) is spun over the wires and substrate, then patterned by photolithography through a Chromium/quartz mask. The region of the AZ layer exposed to UV light remains on the substrate after chemical development, whereas the unexposed regions on the AZ layer are washed away during development. This results in a mould consisting of the silicon substrate, the platinum wires and the AZ micro-chambers, as shown in Fig. 3.9(a)[3].

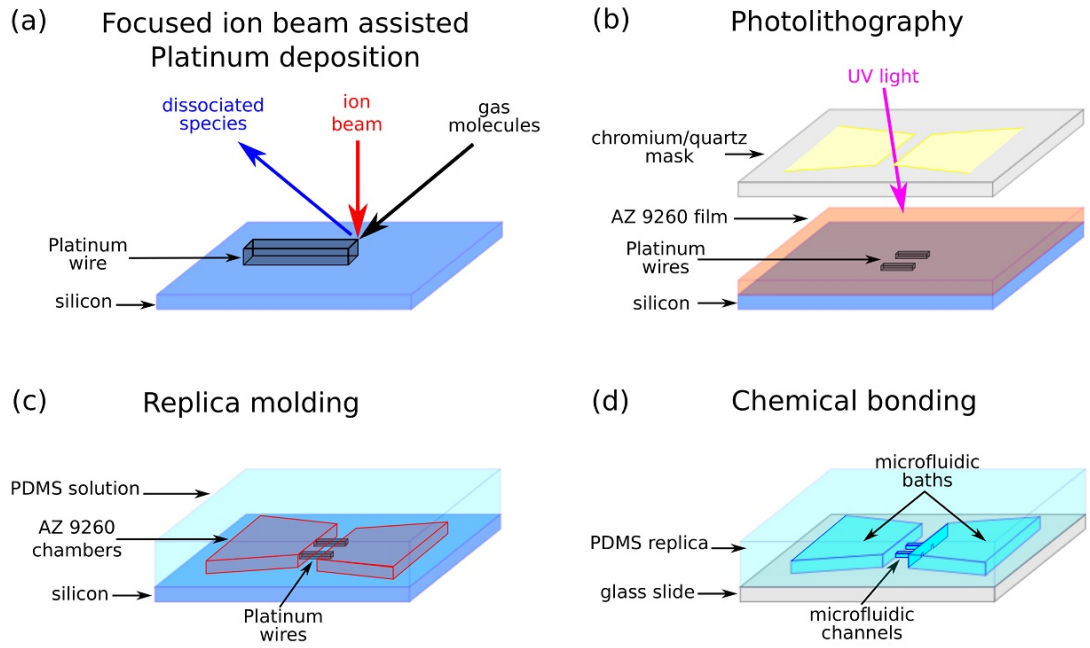

Fig. 3.8 Fabrication process of microfluidic samples. (a) Platinum wires are fabricated on a silicon substrate by FIB assisted platinum deposition. (b) A layer of photoresist (AZ 9260) is spun over the wires and substrate, then patterned by photolithography through a mask. (c) A PDMS mixture is poured over the silicon mould. Once totally solid, the PDMS replica is peeled off the silicon mould carefully. (d) The PDMS replica and a glass slide are plasma cleaned and bonded to form reservoirs and channels. This figure has been published in [68].

Fabricating a microfluidic chip consists of two steps: firstly, the structure on the silicon mould is replicated with Polydimethylsiloxane (PDMS), shown in Fig 3.8(c). The replica of the mould is realised by casting a 10:1 (polymer base:curing agent) PDMS mixture on it, which is left to settle and degas for 30 minutes and then cured at 60 °C for 120 minutes in an oven. The base and curing agent are well mixed by an electric drill beforehand. After cooling

[3]The fabrication processes (a,b) were done by Dr. Stefano Pagliara.

down, the PDMS sample is peeled off the mould along the direction perpendicular to the channel array in order to minimise the mechanical stress along the longitudinal axes of the channels. The channel has a length of 4.8 μm and width of around 1 μm, measured by atomic force microscopy in Fig 3.9(b,c). Two 1.5 mm wide circular holes are punched by a 1.5 mm wide circular disposable biopsy punch (Kai Industries Co. Ltd., Seki City, Japan) to enable fluid access to the microchannels, as shown in Fig 3.9(d). Secondly the PDMS sample is chemically boned to a glass slide via air plasma functionalization as shown in Fig 3.8(d) [69]. The PDMS sample and a glass slide (50×24 mm, thickness No.1, Glaswarenfabrik Karl Hecht GmbH & Co KG) are placed in the chamber of a plasma etcher (Diener, Royal Oak, 127 MI) and degassed for 5 minutes. Afterwards, air is injected in the chamber at 25 sscm and the pressure in the chamber is left to stabilize for two minutes. Finally the sample and the glass slide are exposed to the air plasma (2.5W power, 10 seconds). Right after exposure, the patterned surface of the PDMS replica which contains the channels is brought in contact with the glass slide and a chemical bonding is formed by the air plasma functionalization of the two surfaces. The hollow structures on the PDMS surface and the glass surface form the microfluidic reservoirs and channels.

Polystyrene colloids with diameter of (510 ± 10)nm (Polyscience, Warrington, PA) are used in our experiment. A suspension of spherical particles in 5mM KCL is prepared and sonicated for 15 minutes to break down possible aggregates of colloidal particles. Approximately 4μl of 5mM KCL is injected in the bonded chip through a 27 gauge needle connected to a plastic syringe. Attention is paid to avoiding the formation of air bubbles which may introduce non-equilibrium forces inside the chip. The channels are connected by two reservoirs, as shown in Fig 3.9(a). Afterwards, all the vertical fluid accesses are completely filled with the colloidal suspension. The top surface of the device is finally sealed with a rectangular piece of a cover slip slightly larger than the PDMS sample. In order to protect the original structure on the silicon based mould, a replica procedure is performed and successfully reproduces the micron structure using epoxy, details can be found in Appendix.B and Fig. 3.13.

3.4 Analysis of the trajectory data

Particle tracking provides quantitative information from time-lapse microscopic images, which is of crucial importance in the study of colloidal systems and intracellular dynamic processes [70, 71]. The movement of Brownian particles in our microfluidic sample is recorded as videos. By extracting trajectories of particles, the underlying energy potential is estimated by different methods under equilibrium and non-equilibrium conditions in

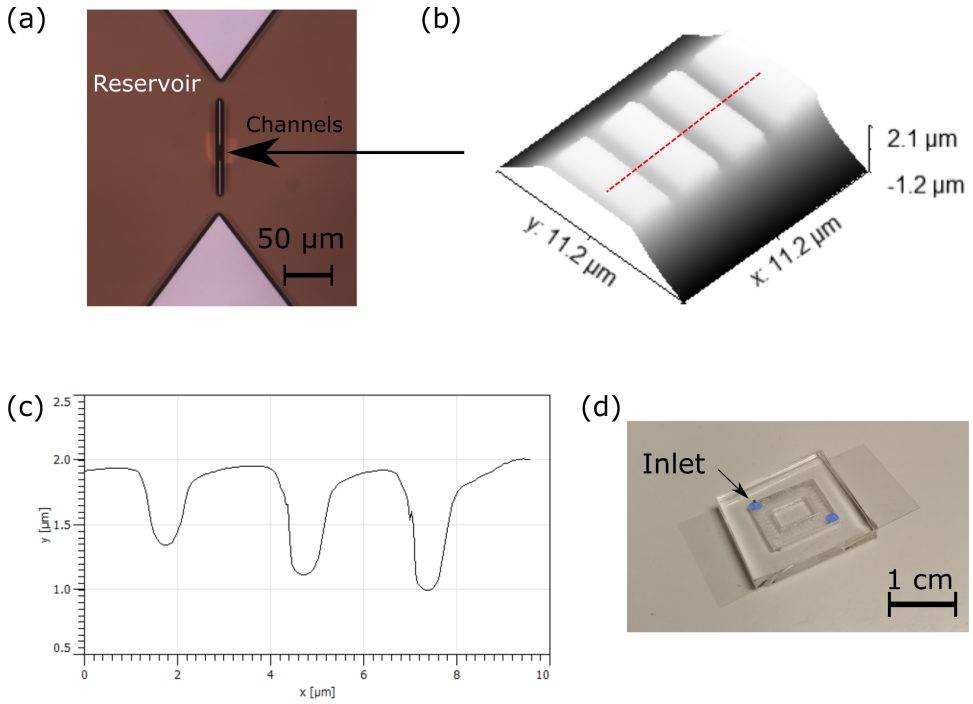

Fig. 3.9 Silicon mould, AFM characterisation and the PDMS sample. (a) Microscopic image of the silicon mould taken under a 2.5x objective. The channels are located at the centre of the image. (b) Three dimensional profile of microfluidic channels on a PDMS sample. (c) Height profile of the section image of the dashed line on (b) shows the cross section of channels. (d) Photo of a microfluidic sample ready for experiments. Colloidal suspension is injected through the two highlighted inlets.

Chapter 4. By analysing those trajectories, the effect of modulated energy potentials on particle transport is studied in Chapter 5.

3.4.1 Particle tracking method and accuracy

Trajectories of particles are extracted from recorded videos by implementing the method proposed by [72] in *Matlab*. Firstly, a background image is generated by averaging all the frames in one video. Only stationary features are shown on the background image, such as the microfluidic structures and dusts on the camera. Secondly, the background image is subtracted from the video frames. The resulting images contain particles undergoing Brownian motion and other noise. A bandpass and a threshold filter is then applied to the resulting images to eliminate the noise. Ideally, only moving particles are left on the image. Thirdly, a two dimensional Gaussian function is used to fit the intensity profile of a particle to get its positions (x, y) on the frames. Each frame has a frame number embedded by the

recording camera which accurately shows the time line t of the experiment. After obtaining $[t,x,y]$ information of particles, individual trajectories are connected in adjacent frames.

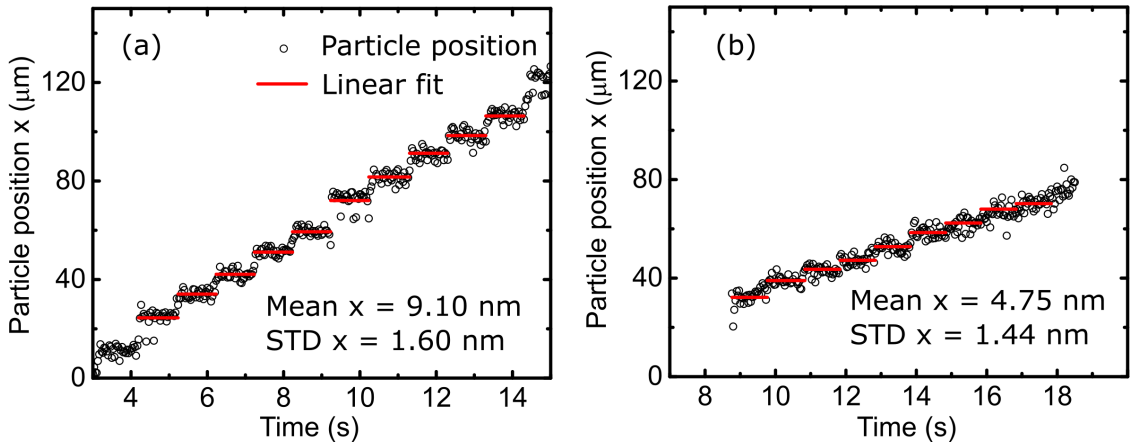

Fig. 3.10 Tracking accuracy tested by moving the Piezo stage with step functions. The position of a particle stuck on the cover glass (circles) is fitted by horizontal solid lines based on the movement of the Piezo stage with a step function. The Piezo stage is moving at (a) 10 nm and (b) 5 nm per step per second.

The tracking accuracy is tested by moving a sample cell with particles stuck on the cover glass. The sample sits on a Piezo stage, which is moved with a step function with position accuracy down to 1 nm according to the manufacturer (Physik Instrumente). The movement of a particle stuck on the cover glass is tracked by our algorithm. We find that our tracking routine is able to distinguish step movement of 10 and 5 nm, as shown in Fig. 3.10. However, the movement is mostly covered by noise when the step decreases to less than 5 nm per step per second.

The magnification produced by an infinity objective is calculated by dividing the reference focal length (500 mm) by the focal length of the objective (180 mm for Olympus). The relation between the pixel length to the real length is obtained by considering the magnification and pixel size of the camera, which is 14 μm for Camera1. We obtain 50.4 nm/pixel as the reference length of a sample on the image, which is further confirmed by imaging a diffraction grating with known lengths.

3.4.2 Calculation of diffusion coefficient

As introduced in Chapter 2, the diffusion coefficient D characterises the mobility of an object in a solvent. In bulk, D can be calculated by $\frac{k_B T}{6\pi\eta a}$ for a single particle with radius a in a solution with viscosity η, where k_B is the Boltzmann constant and T is the absolute temperate.

By inputting $a = 255$ nm, $\eta = 1 \times 10^{-3}$ Pa s, we obtain $D = 0.8\ \mu\text{m}^2/\text{s}$. However, it has been found in experiments that the value of D decreases when close to a wall or in a channel [73], which can be estimated by Faxén corrections [74]. In addition, the diffusion coefficient can be measured from trajectories of particles. For a particle diffusing in one dimension, the diffusion coefficient is calculated by

$$\langle x^2 \rangle = 2D\Delta t \tag{3.1}$$

where x is the trajectory of a Brownian particle, $\langle x^2 \rangle$ is the Mean Square Displacement (MSD) and Δt is the time difference between recorded frames. D is then obtained by fitting a linear line to MSD on Δt. In this thesis, 10 points of MSD are used for the fitting with an example shown in Fig. 3.11(a). The fitting result provides D value of one particle. Considering the variation of particle sizes, at least one hundred D values are calculated and averaged as the diffusion coefficient of one type of particles in a channel.

Our group has previously reported hindered diffusion coefficient of particles close to channel ends due to the increased space [75]. Here, we measure D as a function of channel length x and plot the hindered D effect in Fig. 3.11(b).

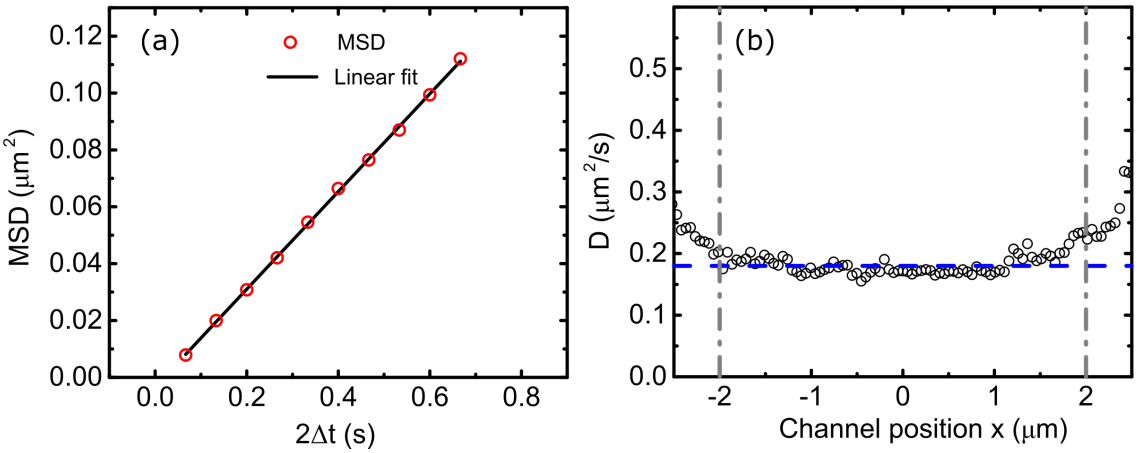

Fig. 3.11 Calculating the diffusion coefficient of one particle diffusing in the channel. (a) MSD of one particle is fitted by a linear line along $2\Delta t$ to obtain D. (b) The dependence of D values on the channel position x. The dash-dotted lines indicate the channel ends. The dash line is a guidance for a constant D along x.

3.4.3 Estimation of particle concentration

The main question in this thesis is concerned with particle transport through channels, and hence the concentration of particles in the microfluidic reservoirs, denoted as c, is a key parameter. Firstly, we examine the effect of gravity in our microfluidic system. The gravitational height h_g of particles in solution can be written down as

$$h_g = \frac{k_B T}{\frac{4}{3}\pi a^3 \Delta\rho g} \tag{3.2}$$

where a is the radius of the particle, g is the gravitational acceleration, $\Delta\rho$ is the difference in mass density between particles and the solvent, k_B is the Boltzmann constant with T the temperature [76]. By putting $a = 255$ nm and mass density 1.05 g/cm^3 of the polystyrene particles into Eq. 3.2, we get h_g close to 0.1 mm which is significantly more than the depth of the reservoirs at ~ 12 μm. Therefore the gravitational effect can be neglected [77] and we assume the colloidal particles disperse evenly in the reservoirs.

Secondly, c is estimated by the tracking algorithm described in Section 3.4.1. To do this, we image a particle stuck on the cover glass in focus, as highlighted by a blue box in Fig. 3.12(a). The microfluidic chip is then moved 1 μm away from the focus by controlling the z position of the Piezo stage. The intensity profile of a particle decreases away from the focus plane of the objective. A threshold value of particle intensity profile is then chosen to detect particles within 1 μm distance to the cover glass in our tracking algorithm. It is worth noting here that we obtain the intensity threshold for static particles. However colloidal particles are undergoing Brownian motion while experiments take place, which adds uncertainties for this detection method.

Finally, we estimate the particle concentration in a reservoir by averaging the number of detected particles during an one-hour video. A typical image of particles diffusing in reservoirs is shown in Fig. 3.12(a). The particle recognised by the tracking algorithm is overlapped with a circle and the particle concentration is evaluated separately in the two reservoirs. The algorithm ignores static (stuck) particles in both the channel and reservoirs. The particle concentrations are estimated in terms of volume fraction for each reservoir and plotted as a function of time in Fig. 3.12(b). From the result, concentrations of particles in both reservoirs are found close to each other throughout the 150-hour measurements, indicating a well equilibrated environment. However, the particle concentrations increase gradually with time, which is in accordance with our previous publication [69]. We attribute the increased particle concentration to the evaporation of solvent in the microfluidic chip. We also mark here that although the current concentration estimation method is easy to implement in a colloidal diffusion experiment, other measurements such as confocal microscopy or

UV-Vis Spectra [78] should be considered if more accurate concentration information is needed.

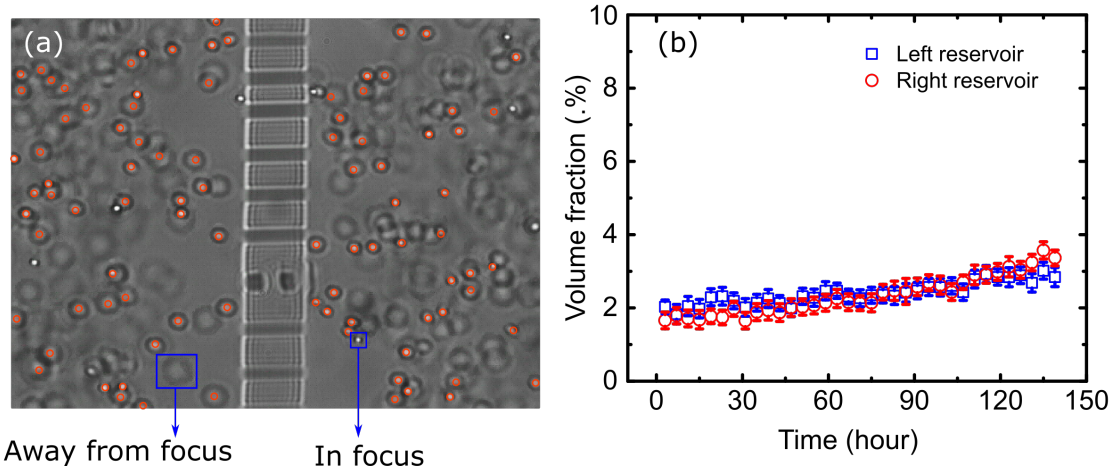

Fig. 3.12 Estimating the particle concentration in reservoirs. (a) The particle tracking results are plotted on one frame of the recorded video. Red circles represent the recognised particles. (b) The volume fraction of particles in the two reservoirs is plotted against time. The error bars are calculated from all the frames in one-hour videos.

3.5 Conclusion

We built up a synthetic membrane system with colloidal particles diffusing in microfluidic channels. Holographic optical tweezers are used to modulate the energy landscape of the channel. The motion of particle is extracted by implementing the particle tracking algorithm in microfluidic environments. Our experimental system is going to be used to measure the energy landscape in a fluid environment in Chapter 4. After the characterisation of energy landscapes, we further explore particle transport in time-dependent energy landscapes in Chapter 5.

Acknowledgement

Dr. Stefano Pagliara built up the first HOTs in Keyser group. Dr. Richard Bowman is thanked for his assistance with implementing the labview-based programme *red tweezers*.

Appendix

A. Table of components in the HOTs setup

The components used to build the HOTs setup are listed in Table. 3.1.

Table 3.1 Components of the holographic optical tweezers setup

Component	Model	Detail
Objective	UPLSAPO ×100	NA 1.4, back focal plane diameter 3.78 mm, Olympus
Laser	YLM-5-1064LP	IPG fibre laser, 1064 nm
SLM	X10468	Hamamatsu, Optical Phase Modulators
Piezo stage	P-561.3CD	Controlled via (E-725.3CD)
Camera1	EoSens CL Full	Mikrotron, High frame rate camera
Camera2,3	DMK 41BUC02	Imagingsource, USB 2.0 monochrome camera
M1-4, M8-9	BB1-E03	1" AR-coated dielectric mirrors
M5,6,7	BB1-E03	2" AR-coated dielectric mirrors
M10	PFE10-P01	1" Protected Silver Elliptical Mirror
$\lambda/2$	WPH10M-1064	Zero-Order Half-Wave Plate
PBS	PBS253	1" Polarizing Beamsplitter Cube, 900 - 1300 nm
P1,P2	ID12/M	Mounted Standard Iris
L1	LA1805-C	1", f = 30.0 mm, AR Coating
L2	LA1433-C	1", f = 150.0 mm, AR Coating
L3	LA1908-C	1", f = 500.0 mm, AR Coating
L4	LA1708-C	1", f = 200.0 mm, AR Coating
L5	LA1484-C	1", f = 300.0 mm, AR Coating
L6	LA1908-C	1", f = 500.0 mm, AR Coating
L7	LA1131	1", f = 50.0 mm
L8	LA1805	1", f = 30.0 mm
L9	LA1708-C	1", f = 200.0 mm, AR Coating
L10	LA1433-C	1", f = 150.0 mm, AR Coating
BS1	BP208	2" 8:92 (R:T) Cube-Mounted Pellicle Beamsplitter
BS2	BP108	1" 8:92 (R:T) Cube-Mounted Pellicle Beamsplitter
D1	Linos	Dielectric-Coated Plane Mirrors DLHS NIR 1064 nm
F1,2	M254H00	1" UVFS Hot Mirror
F3	NE80A	1" Absorptive Neutral Density Filters
Lamp	MWWHL4	White mounted LED
Optics table	Newport I-2000	High performance laminar flow isolator

B. Using epoxy to replicate micro-structures

The fabrication process described in Section 3.3.3 takes long hours with many trials to get the desired structure. Meanwhile, the mould is fragile due to the rigidity of silicon. The peeling process to separate PDMS from the mould makes the chance to snap the mould even higher. In order to protect the original mould, we use epoxy to replicate the structure on the mould. This idea has been explored by using PDMS with different stiffness as a copy of the structure on a silicon mould [79]. So far, we find the protocol from Jun Lab at University of California San Diego, which use epoxy as the new substrate provides the best replica result. The original protocol has been tailored to perform in our lab conditions and described as following:

1. A PDMS sample cell as a copy of the silicon mould is made as described in Fig 3.8(c,d).

2. In order to make the separation between epoxy and PDMS sample easy, a salinisation agent is deposited on the surface of the PDMS sample first. To do this, 200 μl salinisation agent (1H,1H,2H,2H-Perfluorodecyltrichlorosilane, 96%) is placed evenly in a glass vacuum chamber with the PDMS sample inside. The chamber is vacuumed immediately after putting the salinisation agent, other wise the agent oxidises shortly. The PDMS sample is left in the vacuumed chamber for one hour to let the salinisation agent settle on the surface.

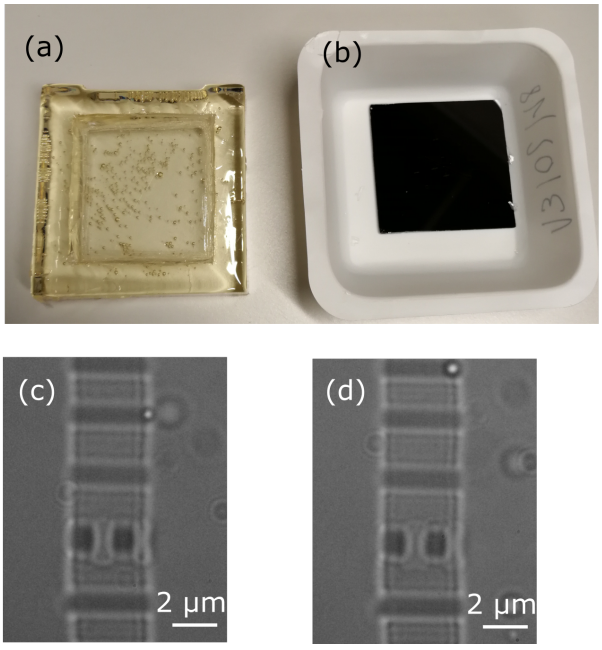

Fig. 3.13 Photos of an epoxy mould (a) and a silicon mould (b) which carry the same microfluidic structures. (c) and (d) show the microfluidic channels made from (a) and (b) respectively. Under microscope, the two samples appear to be identical and both used for the experiments in this thesis.

3. Epoxy (LOCTITE HYSOL 9483 50ML) is poured over the PDMS straight after the saliniation process. The epoxy is mixed by a mixing tube and gun provided by the epoxy manufacturer. Note here, many different types and brands of epoxy products have been tried but the only product works is the above mentioned one.

4. After step 3, air bubbles are found in epoxy, the interface between epoxy and PDMS, and mainly inside the porous PDMS. A key to make a successful epoxy replica is to get rid of all the trapped air bubbles. Therefore, the liquid epoxy and the PDMS sample is degassed in a vacuum chamber for 20 minutes. Degassing for too long will solid the epoxy due to the low boiling point of epoxy in a vacuum environment. After 20 minutes, all the small bubbles should have disappeared. The surface between epoxy and PDMS is checked to be bubble-free.

5. Finally, the epoxy along with the PDMS chip is left for 24 hours on a flat surface to become solid. It is then hardened enough to be separated from the PDMS and works as a new mould. Due to the salinisation process in step 2, the separation should be effortless.

By using the epoxy shown in Fig. 3.13(a), the original silicon mould [Fig. 3.13(b)] is backed up and can be reproduced easily. According to Jun lab, the accuracy of replica can be down to nanometres. We find no differences between the geometry of the channels made from an epoxy mould and a silicon mould [Fig. 3.13(c,d)].

Chapter 4

Reconstruction of potential energy landscapes in microfluidic channels

Membrane protein undergoes conformational changes to transport specific solutes across the membrane. To simulate this effect, we generate energy landscapes with high barriers by holographic optical tweezers in our synthetic membrane system. Understanding the effect of the energy landscape on particle transport requires an accurate knowledge of the energy landscape experienced by the particles. There are many ways of determining the energy landscape, including measurement of the Probability Density Function (PDF), the Splitting Probability (SP), the intensity distribution of optical traps and the velocity of particles driven by external forces. Each method is, however, associated with certain limitations especially for reconstructing energy landscapes in systems out of equilibrium.

In this chapter, we first calibrate the intensity distribution of optical traps with the potential energy landscape measured through the PDF method. The calibrated energy landscape is further confirmed by comparing to the energy landscape rebuilt from velocity of particles driven by external forces. Importantly, we develop a new method to extract the underlying energy landscape by analysing Local Transition Probabilities (LTP). Our method is applicable to both equilibrium and non-equilibrium steady states. Compared to the SP method, the LTP approach offers improved robustness in the use of small trajectory ensembles or fragmented trajectories, which is tested in colloidal diffusion experiments and Brownian dynamics simulations. In the end, we demonstrate that combining the LTP with the measurement of the intensity distribution of optical traps allows for the estimation of potentials with high barriers which are inaccessible for trajectory-based methods.

4.1 Reconstructing potential energy landscapes from optical intensity distributions

4.1.1 Introduction

Binding sites in membrane transporters which show high affinity to specific substrates have been investigated via crystal structures [16–18], molecular simulations [22, 23] and theoretical models [24, 25, 80]. HOTs have been used to generate energy wells near entrances of microfluidic channels to mimic binding-site effect at the transporter mouths [51, 52]. A colloidal particle in an attractive energy well experiences an increased affinity similarly to what a solute experiences in a membrane transporter. In a previous research done by our group [52], a 40-fold enhancement in translocation rate of particles across a channel was found with an attractive potential in the channel compared to a channel without external potentials. Besides binding, membrane proteins can also perform rigid-body rocking-type movements to rearrange from an outward to an inward-open configuration and vice versa [14]. Conformational changes between open and closed states have been found in primary active transporters like ABC transporters [11, 81], and secondary active transporters like sodium coupled cotransporters [8]. However, it is difficult to change the geometrical landscape of a channel dynamically in a synthetic experimental system. Therefore, in order to investigate the effect of conformational changes on channel transport, we use HOTs to generate high energy barriers which impede the movement of particles to simulate the effect of a 'closed' state in the channel, and deep energy wells to imitate the 'open' state of a channel. Meanwhile, the HOTs are able to oscillate the position of the energy barrier, which performs fluctuation between the open and closed states.

In order to characterise a underlying potential energy landscape, trajectories of Brownian particles have been used to reconstruct the potential energy landscape $U(x)$. In systems at equilibrium, the probability density function (PDF) of a large ensemble of single-particle trajectories can be used to estimate $U(x)$ [51, 57, 58] (details discussed in Section 2.3.1). However, the PDF fails to describe deep energy wells (e.g. $> 5\ k_B$T) in our experimental system due to few or no trajectories available in those regions. The PDF method is also impractical to estimate a potential fluctuating at a time scale shorter than the particle diffusion time.

An alternative way to measure an optically induced potential is by calibrating the intensity distribution of the optical traps. An effective potential energy landscape is obtainable by convoluting the intensity distribution with a form factor function [82]. The form factor contains information of the material and the shape of the trapped object.

In this section, we adopt the method proposed in [82] where the intensity distribution of optical traps is calibrated to estimate the optically induced potential with high barriers. Our work provides a method to characterise diffusion in confined geometries where molecules strongly interact with their environment.

4.1.2 Theory

HOTs are used to generate optical traps with various configurations which modulate potential energy landscapes. Importantly, objects of different geometry and composition in a same environment experience different energy landscapes. The effective energy landscape $U_I(x)$ can be calculated by convoluting the laser intensity distribution $I(x)$ with a form factor function f [82]

$$U_I(x) = (f \circ I)(x), \tag{4.1}$$

where f depends on the object and the environment. $I(x)$ can be measured from images captured by an infrared camera. In this thesis, we consider the form factor function f of a uniform dielectric sphere of a radius a illuminated by light of wavelength λ, where $\lambda > a$ [83]

$$f(x) = \alpha\sqrt{(a^2 - x^2)}\Theta(a - x) \tag{4.2}$$

where Θ is the Heaviside step function and

$$\alpha = \frac{\sqrt{\varepsilon_0}}{c}\left(\frac{\varepsilon_0 - \varepsilon}{\varepsilon + 2\varepsilon_0}\right) \tag{4.3}$$

where ε_0 is the dielectric constant of the medium, ε is the dielectric constant of the particle and c is the velocity of light. Monitoring $I(x)$ gives us a way to approximate the energy landscape.

The optical trap is the only external contribution to the potential energy landscape at equilibrium. However, the value of $I(x)$ depends on the camera model and settings. As a result, $U_I(x)$ only provides a qualitative estimation of the underlying potential energy landscape. Meanwhile the PDF of particle positions can be related to the potential energy landscape $U_{PDF}(x)$ through the Boltzmann distribution. Previous study on optical traps has demonstrated that depth of optical traps is linearly proportional to the laser power up to 200 k_BT [61] which also agrees with the theoretical prediction [84]. Therefore, we are able to calibrate $U_I(x)$ with $U_{PDF}(x)$ for energy landscapes without high barriers using the following equation,

$$U_{PDF}(x) = C \cdot U_I(x) \tag{4.4}$$

where C is a scaling factor between the two energy landscapes. We find C to be a constant by calibrating $U_{PDF}(x)$ and $U_I(x)$ under various trap configurations, including different depths, lengths and numbers of traps. Crucially, obtaining the scaling factor C for energy landscapes without high barriers allows us to estimate the energy landscape with high barriers through $U_{I,PDF}(x) = C \cdot U_I(x)$, where the trajectory-based method fails due to extremely low probability of escaping from those high energy barrier regions.

4.1.3 Experimental methods

Measurement of the trajectories of Brownian particles

Particle trajectories are measured by a drag-and-release experiment in a potential energy landscape where the particle explores all regions of the channel within the experimental time scale. We fabricated microfluidic devices as described in Section 3.3.3. Briefly, each device is made of glass and Polydimethylsiloxane, and consists of two 12 μm deep reservoirs connected by an array of channels with a length of 4.8 μm and a cross section of around 0.9×0.9 μm^2. We filled the device with polystyrene colloidal particles with a diameter of (510 ± 10) nm. The particles freely diffuse in the reservoirs but are restricted to single file diffusion within the channels. A typical bright field image of a particle in the channel is shown in Fig. 4.1(a). We used HOTs [51, 52, 67, 85, 86] to position the particle and generate specific optical potential energy landscapes in each channel. The optical intensity distribution is monitored by an infrared camera, as shown in Fig. 4.1(b) and sketched in Fig. 4.1(c).

Videos of the movement of each particle are recorded by a fast camera. The trajectories of particles $x(t)$ [sample in Fig. 4.1(d)] are extracted off-line from the recorded videos using a custom implementation of the Crocker and Grier's algorithm [72] (details in Section 3.4). The first thirty frames of each particle movement are discarded in order to exclude the effect of trapping on the reconstructed energy landscapes.

Our drag-and-release measurements consist of six steps as illustrated in Fig. 4.1(e): I. Trap a single particle diffusing in either reservoir using HOTs. II. Position the particle at a position chosen randomly from a uniform distribution along the channel. III. Use HOTs to set up laser line traps which produce local potential wells. IV - VI. Release the particle and record its trajectory until it escapes the channel. This process is repeated at least one hundred times for each potential energy landscape configuration.

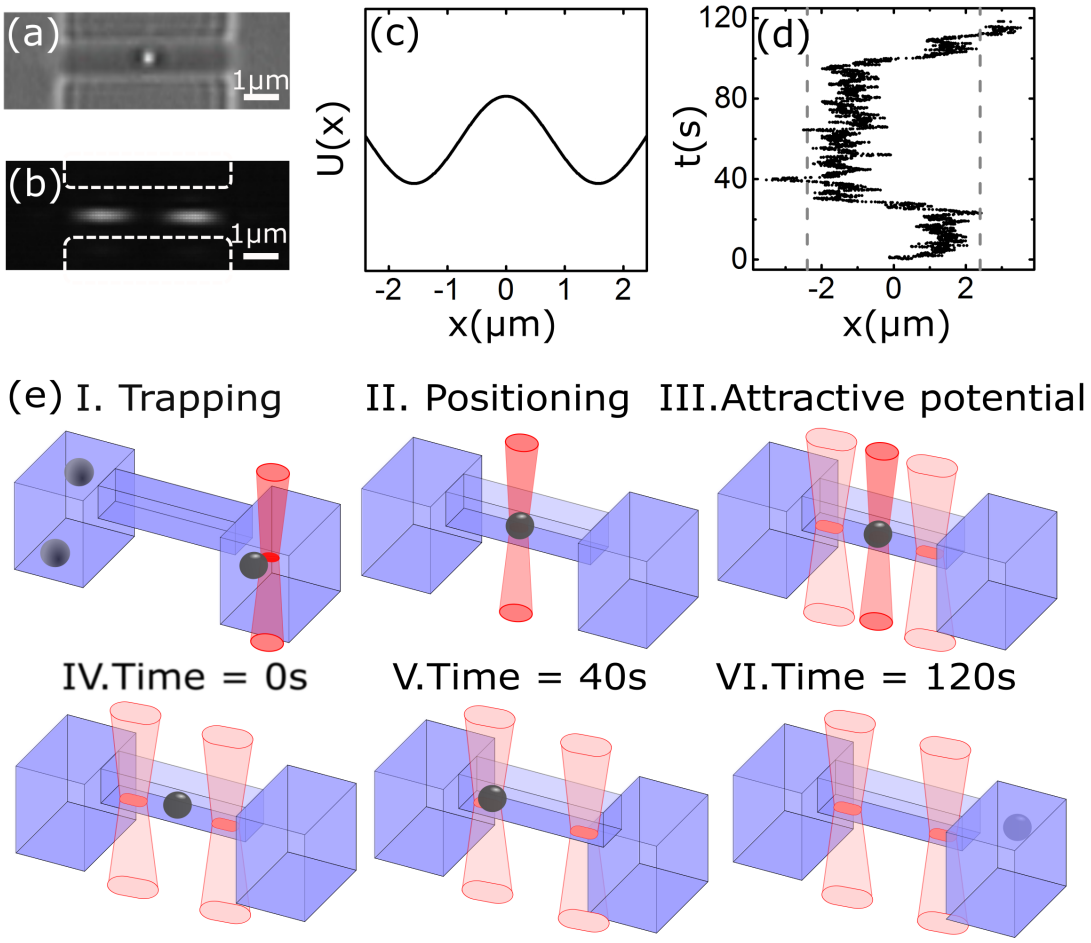

Fig. 4.1 Measuring potential energy landscapes in microfluidic channels. (a) Bright-field image of a polystyrene particle of diameter 510 nm trapped in the centre of a microfluidic channel of length 4.8 μm and connecting two large reservoirs of depth 12 μm. (b) Dark-field image of the intensity distribution of two laser line traps generated by the HOTs. The dashed lines highlight the channel contour. (c) Sketch of the potential wells generated by the two laser line traps in the channel. (d) Sample trajectory of one particle diffusing in the channel. (e)Illustration of the protocol used for drag-and-release measurements.

Calculating the probability density function of particle positions

The PDF approach, as described in Section 2.3.1 is applicable to systems at equilibrium. It relates the underlying energy landscape $U_{PDF}(x)$ to the probability density function of particle positions $p(x)$ via Eq. 2.16. Here $p(x)$ is the probability to find a particle in a bin centred at x, with the width of the bin here defined to be one pixel of the camera. The position distribution

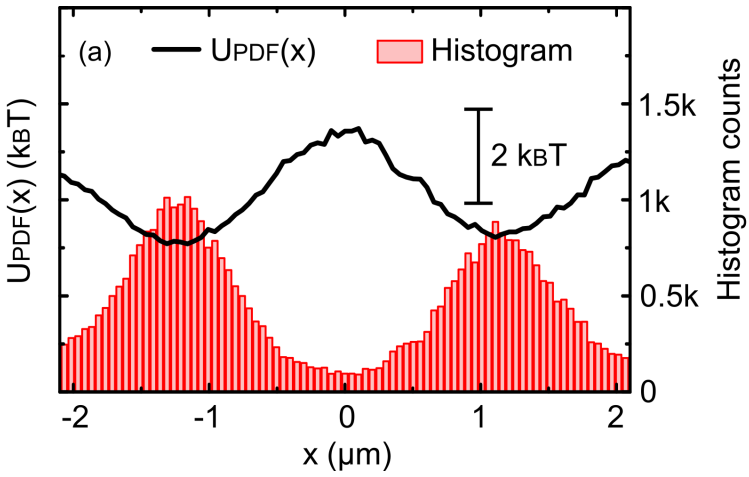

Fig. 4.2 Implementing the PDF method to reconstruct the energy landscape. The histogram (bars) is the position distribution of particles diffusing in the energy landscape. $U_{PDF}(x)$ (solid line) is inferred from the PDF through the Boltzmann distribution. Note: the relative value of $U(x)$ shows the energy landscape experienced by the particle but the absolute value of $U(x)$ is meaningless.

of particles diffusing in an energy landscape is first plotted in a histogram, represented by bars in Fig. 4.2. Dividing each position count in the histogram by the sum of all the counts leads to the particle density function $p(x)$. $p(x)$ is then put into Eq. 2.16, which gives us $U_{PDF}(x)$ [solid line in Fig. 4.2]. From $U_{PDF}(x)$, we can clearly see two energy minima. Note here, the absolute value of a potential energy landscape depends on the partition function in Eq. 2.16, as described in Section 2.3.1. However, the differences between $U(x)$ at each position show the energy landscape experienced by the particle. Therefore $U(x)$ is plotted with a scale bar instead of absolute values in the rest of the thesis.

Measuring the optical intensity distribution

The intensity distribution of optical traps is recorded by a monochrome camera. The optical path of the setup can be found in Section 3.2. To obtain a stable intensity distribution for different laser trap configurations, the digital gain of the camera is set to be at a minimum value. The shutter time of the camera is also chosen to have a large range of sensitivity.

While a short shutter time introduces more background noise, a very long shutter time results in overexposures. In addition to the gain value and the shutter time, all other settings of the camera are kept constant.

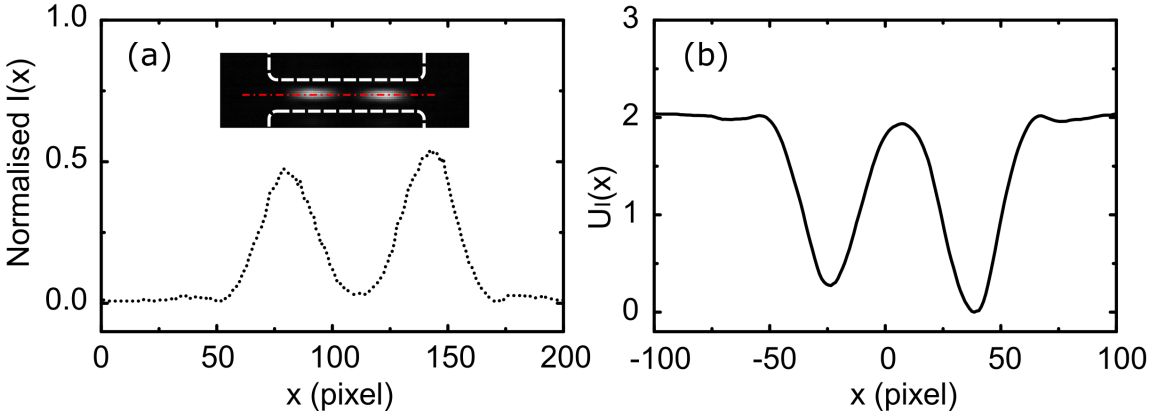

Fig. 4.3 An intensity distribution of optical traps and the corresponding effective energy landscape. (a) Normalised intensity distribution $I(x)$ measured at the channel longitudinal axis. Inset: Optical intensity distribution recorded by a monochrome camera. The dashed lines indicate the contours of the channel. The red dash-dotted line represents the positions where $I(x)$ is obtained. (b) $U_I(x)$ is calculated by Eq. 4.1 using $I(x)$ plotted in (a), considering a Polystyrene particle of radius $a = 255$ nm diffusing in water.

To obtain an effective energy landscape, we first measure a two-dimensional intensity distribution of the optical traps from a recorded grey scale image, an example of which is shown in the inset of Fig. 4.3(a). Since the two laser lines are focused into the centre of the channel in diffusion experiments, we measure a one-dimensional (1D) distribution in the middle of the 2D intensity distribution [red dash-dotted line in the inset of Fig. 4.3(a)]. The 1D distribution is then normalised by 255, which is the maximum bit depth of one pixel to make sure the image is not overexposured. Clearly from Fig. 4.3(a), the normalised $I(x)$ (dotted line) did not hit the maximum bit value so the image is not saturated. Next, the effective potential energy landscape $U_I(x)$ is calculated by putting $I(x)$, particle radius $a = 255$ nm, dielectric constants of Polystyrene and water into Eq. 4.1 [Fig. 4.3(b)]. Notably, small fluctuating structures in $I(x)$ are smoothed out in $U_I(x)$. This is due to the physical size of the particle being bigger than the fine structures in the intensity profile. In general, a larger particle experiences the force gradient in an optical trap at a larger range compared to a smaller particle [82].

By calibrating $U_I(x)$ with $U_{PDF}(x)$, we can obtain a scaling factor C via Eq. 4.4. C is going to be used to estimate energy landscapes with high barriers which cannot be assessed by the PDF method.

4.1.4 Results and discussion

The scaling factor C is obtained from four different energy landscapes, L1 to L4. For one potential energy landscape, we first measure $U_{PDF}(x)$ and $U_I(x)$ as previously described then calibrate $U_I(x)$ by a scaling factor C to match $U_{PDF}(x)$ via a least-squares fitting by Eq. 4.4. The least-squares fitting iterates the C and two-dimensional position parameters until it finds the smallest summed square of residuals χ^2. The fitting is done by *Curve Fitting Toolbox* in *Matlab*. For example, We get $C = 3.05$ by calibrating $U_{PDF}(x)$ (dashed line) and $U_I(x)$ (dash-dotted line) in Fig. 4.4(a). The fitted potential, denoted by $U_{I,PDF}(x)$ is plotted by a solid line in Fig. 4.4(a). The same calibration procedure is carried out on energy landscapes L2 to L4. As can be seen from Fig. 4.4(a-d), $U_{I,PDF}(x)$ matches $U_{PDF}(x)$ reasonably well after calibrations. Fitting results including χ^2 error are listed in Table 4.1. The value of C varies in a range between 3.05 and 3.49. $C = 3.05$ is chosen as the general scaling factor with the lowest χ^2. We apply $C = 3.05$ to calibrate L2 to L4 with ${\chi_C}^2$ listed in Table 4.1. The difference between χ^2 and ${\chi_C}^2$ is within 17%. Finally, we use the obtained C to estimate a potential with high energy barriers where no particle trajectory is available to resolve $U_{PDF}(x)$ [dashed line in Fig. 4.4(e)]. We obtain an energy landscape $U_{I,PDF}(x)$ has a barrier higher than 5 k_BT [solid line in Fig. 4.4(e)].

Table 4.1 Calibration parameters for different landscapes. L is the landscape number. P is the nominal output power of laser. l is the length of a line trap. G is the distance between two line traps. The estimation boundary is calculated under 95% confidence. χ^2 is the sum of squares of error between U_{PDF} and $U_{I,PDF}$. ${\chi_C}^2$ is the sum of squares of error between U_{PDF} and $C \cdot U_I$ with $C = 3.05$.

No.	P (W)	l (μm)	G (μm)	Scaling factor C	Bounds of C	χ^2	${\chi_C}^2$
L1	0.5	1.5	1.3	3.05	[2.97,3.15]	1.78	1.78
L2	0.1	1.5	1.3	3.40	[3.21,3.57]	4.26	5.15
L3	0.5	1.0	2.4	3.18	[2.85,3.52]	11.64	11.43
L4	1.0	1.5	1.4	3.49	[3.24,3.74]	28.20	32.69
L5	2.0	1.5	1.4	-	-	-	-

It is worth nothing here, Eq. 4.2 is valid under the condition that the particle size is sufficient smaller than the wavelength of the light, called Rayleigh approximation [84]. Our experimental length scale, however, does not fall in the Rayleigh approximation range thus the generalized Lorentz-Mie scattering theory should be applied to describe the force interaction between light and object [84]. However, our method works surprisingly well for rebuilding bias-free potential energy landscapes. The accuracy of the rebuilt potential energy landscape is further demonstrated in the next section where the depth of potential

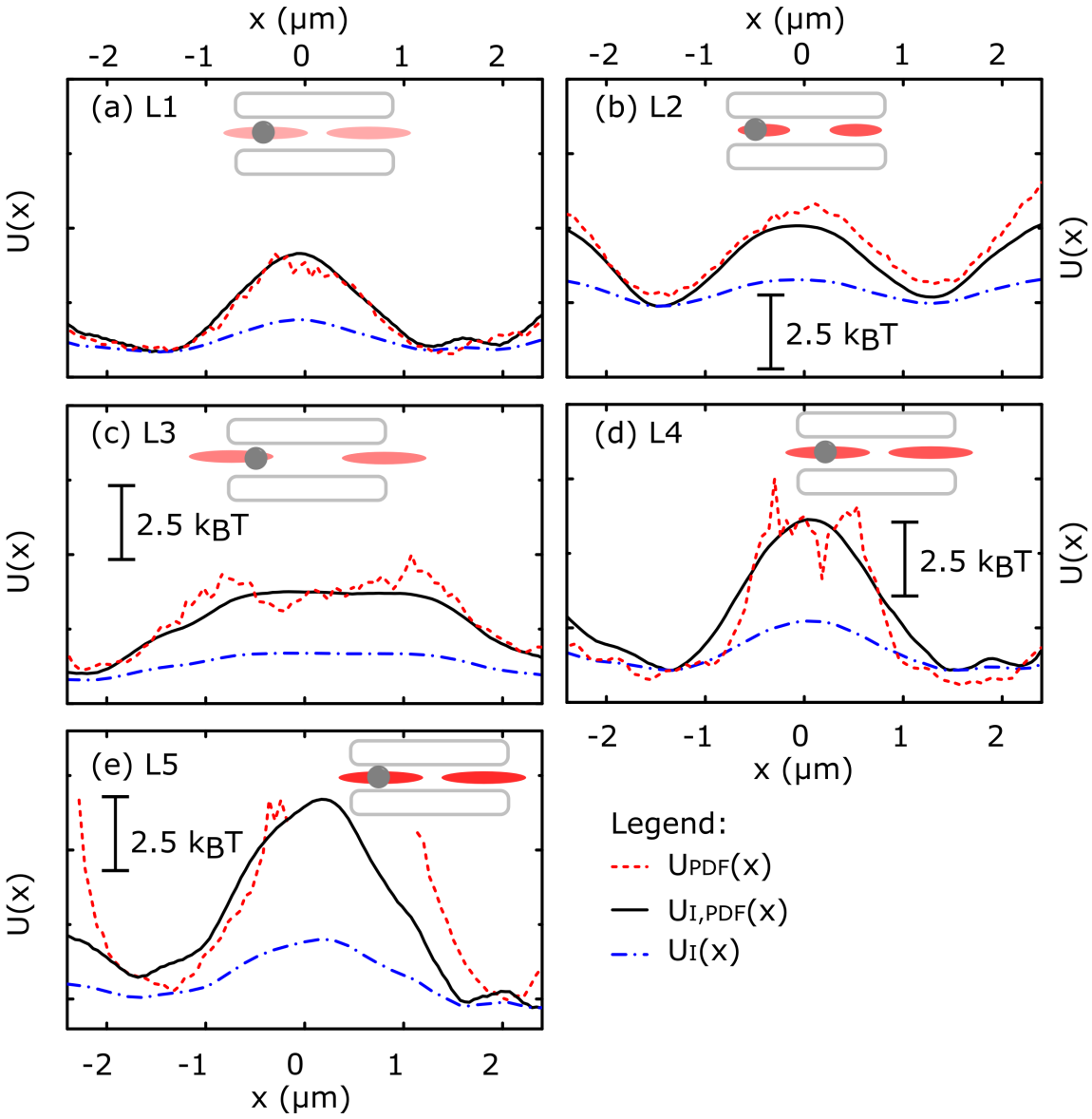

Fig. 4.4 Reconstruction of energy landscapes in the presence of shallow and deep energy wells at equilibrium. (a) Fitting the effective energy landscape $U_I(x)$ (dash-dotted line) evaluated from the intensity distribution $I(x)$ with $U_{PDF}(x)$ (dashed line). This allows us to obtain the calibrated energy landscape $U_{I,PDF}(x)$ (solid line). (b-d) The same fitting procedure is carried out on different energy landscape configurations. (e) $U_{PDF}(x)$ is invalid in the face of a high energy barrier. $U_{I,PDF}(x)$ is applied to estimate the energy landscape using $I(x)$ of the optical traps. The insets sketch the configuration of optical traps used for each experiment. Note: the relative value of $U(x)$ at each position shows the energy landscape experienced by the particle.

energy landscape is as deep as 15 k_BT by showing that the potential reconstructed from particle speed is in good agreement with this method. We suspect that the confinement of

microfluidic channel which constrains the light matter interaction to 1D may be one of the reasons that our method works outside Rayleigh range. The theoretical reason behind is worth further investigation.

4.2 Mapping potential energy landscapes by driving particles

4.2.1 Introduction

In order to measure the profile of deep energy wells, one approach is to drive the trapped particle away from the energy minimum. For example, particles have been flushed by a syringe pump through an optical potential [61]. The potential experienced by the particle is then rebuilt based on the change of the particle velocity. In another work, an optically trapped particle was approached by another trapped particle as a probe [87]. The energy landscape was rebuilt from the displacement of the probe particle. Beside those two examples, Piezoelectric stages [88, 89], dual beam optical traps [90] and gravity force [91] have been employed to drive particles to high energy barrier regions which are otherwise rarely explored at thermal equilibrium. In this section, we drag particles through an optically induced potential to validate the optical intensity distribution method introduced in Section 4.1.

4.2.2 Theory

For systems at a low Reynolds number, the velocity of a particle driven under a constant force $F_{drive}(x)$ remains constant due to no particle inertia. Meanwhile, an optically induced potential $U(x)$ exists a force $F_{opt}(x)$ on the particle which influences the velocity of particle. Overall, $U(x)$ can be inferred with the knowledge of the particle velocity $v(x)$ through Eq. 2.21 (details in Section 2.3.3). However, the particle is also undergoing Brownian motion, so $v(x)$ here denotes the mean velocity of particles at x which is later used to resolve the energy landscape.

By assuming the potential energy landscape generated by a laser line trap is a Gaussian function, $U(x)$ can be written down as [92]

$$U(x) = U_0 \cdot (1 - \exp[-\frac{k(x-x_0)^2}{2 \cdot U_0}]) \tag{4.5}$$

where x_0 is the position of the centre of the trap, k and U_0 can be interpreted as trap stiffness and depth in a typical optical trap. Here, k and U_0 are used as fitting parameters. The relation between $v(x)$ and $U(x)$ can be deduced as follows [61]

$$v(x) = v_{drive}(x) + \frac{1}{\zeta} k(x - x_0) \cdot U_0 \cdot (-\exp[-\frac{k(x-x_0)^2}{2 \cdot U_0}]) \tag{4.6}$$

where ζ is the friction coefficient of the particle. By obtaining the experimentally measured $v(x)$, we can fit the velocity profile using k and U_0 in Eq. 4.6, which can then be used to reconstruct the energy landscape.

Here we introduce the *Péclet* number to give an idea of the relative importance between Brownian motion and drift flux. It is defined by the ratio of the time a particle takes to diffuse over its own radius to the time to be driven over its own radius, written as

$$Pe = \frac{a^2 \zeta}{k_B T} / \frac{a}{v} = \frac{\zeta v a}{k_B T} \tag{4.7}$$

where a is the particle radius and v is the velocity of the particle. While the effect of Brownian motion is negligible compared to the driving force with $Pe \gg 1$, diffusion becomes more important when Pe gets close to 1 [62].

4.2.3 Experimental methods

In this experiment, the particle is driven by moving a Piezo stage on which the sample cell sits[1]. The microfluidic sample containing channels and colloidal suspensions is fixed on the Piezo stage by magnets. By controlling the position of the Piezo stage, we can move the sample cell at a constant velocity. The optical potential to be mapped is first placed outside the channel, as illustrated in Fig. 4.5(a). A colloidal particle is trapped by the HOTs and dragged to the centre of the channel. A typical microscope image of a particle in a channel is shown in Fig. 4.5(b). Once the particle is released, the sample moves at a constant velocity $v_{drive}(x)$ by the Piezo stage towards the optical potential until the particle and channel pass the optical potential. Measurements are repeated at least one hundred times for one potential energy landscape to obtain mean velocity of particles along x. Here x is the particle position on the recorded video frames, which is irrelevant to the position of the channel. Positions of particles are extracted by the algorithm described in Section 3.4.1. $v(x)$ is calculated by the position difference between two video frames with a time difference of 0.02 s. $v_{drive}(x)$ is chosen to be big enough to push particle out the energy minimum. However, motion blur in

[1] This idea was first implemented by Dr. Michael Juniper [30] at University of Oxford.

the recorded videos gets worse with $v_{drive}(x)$ increased. So $v_{drive}(x)$ is optimised subject to the configuration of different energy landscapes.

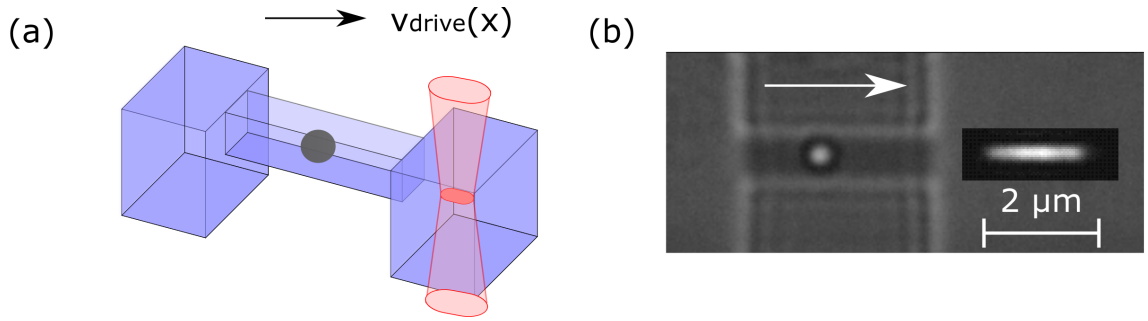

Fig. 4.5 Driving a particle in a channel through an optical potential. (a) Sketch of the initial position of a line trap outside the channel. A particle is placed at the centre of the channel. Once the particle is released, the sample is moved towards the optical potential at a constant speed. (b) An image of the moving sample with a superimposed picture of a stationary laser line trap. The arrow indicates the moving direction of the sample cell.

4.2.4 Results and discussion

Individual particles are first driven through the channel with no external optical potential placed on the driving path. The velocity of the particles here only depends on the magnitude of the driving force, which is imposed by moving the sample at a constant speed. In Fig. 4.6(a), the particle velocity $v(x)$ is plotted as circles for a sample moving at 6 μm/s. Each $v(x)$ is obtained by averaging the velocities of one hundred particles on x. As can be seen from Fig. 4.6(a), $v(x)$ is constant over x. Next, by averaging all $v(x)$, we find the averaged velocity v_{ave} of 5.9 μm/s, which is closed to $v_{drive} = 6\mu$m/s. The *Péclet* number $Pe = 6.1$ by putting v_{drive} into Eq. 4.7. We repeat these measurements at different v_{drive} and plot the result in Fig. 4.6(b). The nearly perfect agreement between the driving velocity v_{drive} and v_{ave} shows that inertia is indeed negligible in our microfluidic environment.

To map an optical potential, the optical trap is placed outside the channel on the channel axis. The influence of the optical force on the movement of a particle can be easily seen from the trajectory of the particle. A sample trajectory is plotted in Fig. 4.7(a). At the beginning and the end of the trajectory, the particle is moving at a constant speed. However, the velocity of the particle suddenly increases, then decreases sharply when the particle falls into the optical trap and is forced out [between two dashed lines on Fig. 4.7(a)]. The relative velocity of particle to channel, $(v(x) - v_{drive}(x))$ is plotted in Fig. 4.7(b) which clearly traces the change of the local force.

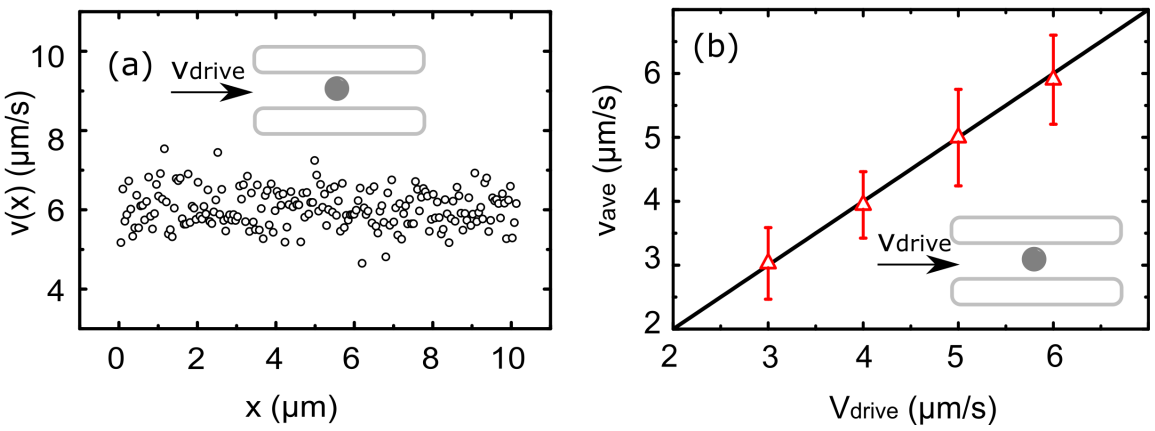

Fig. 4.6 (a) Velocity profile of a particle $v(x)$ dragged without passing an optical energy landscape. (b) Averaged velocity of particles v_{ave} driven at a constant v_{drive} without passing an optical potential.

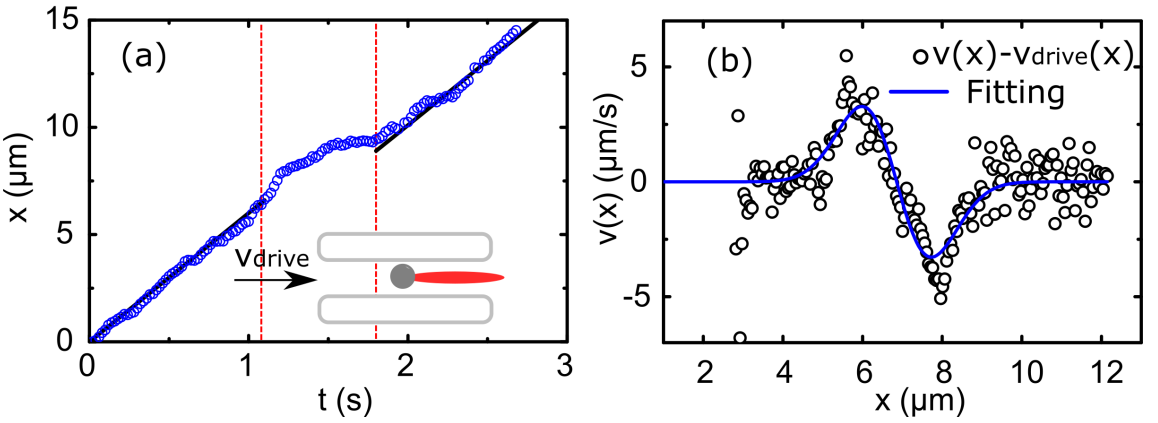

Fig. 4.7 Velocity of a particle driven through an optical potential. (a) A sample trajectory shows the optical force existing on a particle. The solid line indicates the linear relation between t and x. Red dashed lines indicate the non-linear region between t and x. (b) The relative velocity of a particle to microfluidic channel $v(x) - v_{drive}(x)$ (circles), whilst moving through an optical line trap. The velocity profile is fitted by Eq. 4.6, plotted by a solid line.

Two conceptually similar methods are used to resolve the underlying potential energy landscape using $v(x)$ with result plotted in Fig. 4.8(a). (i) By subtracting $v_{drive}(x)$ from $v(x)$, the optical force $F_{opt}(x)$ along the moving axis x is obtained through the Stokes' law (Eq. 2.2). $F_{opt}(x)$ is then integrated along x through Eq. 2.21 with dx equal to the length of one camera pixel. The integration gives us the potential energy landscape, denoted as $U_{velocity}(x)$ [circles in Fig. 4.8(a)]. The same method is used to rebuild energy landscape from $v(x)$ for a channel

without an optical potential, result plotted in Appendix A. (ii) Based on the assumption that a line trap induced potential can be fitted as a Gaussian function, the velocity profile of particles is first fitted by Eq. 4.6 which outputs two fitting parameters k and U_0. The fitting result is plotted by a solid line in Fig. 4.7(b). The fitting parameters are then employed in Eq. 4.5 to get $U_{fit}(x)$ [solid line in Fig. 4.8(a)]. The energy landscape rebuilt from the two methods matches each other.

$U_{velocity}(x)$ is further compared with $U_{I,PDF}(x)$ introduced in Section 4.1 to resolve the potential energy landscape. First, we calculate $U_I(x)$ [dash dot line in Fig. 4.8(b)] from the intensity distribution of the optical traps then calculated $U_{I,PDF}(x)$ by previous found scaling factor C [dashed line in Fig. 4.8(b)]. Next, we calculate the $U_{velocity}(x)$ based on the first method described in the previous paragraph and plot it against $U_{I,PDF}(x)$ in Fig. 4.8(b). Remarkably, the result from two independent methods shows great agreement which further verifies the optical intensity calibration method (detail in Section 4.1). It is worth noting that the standard deviation of velocity of a moving particle $\Delta v = \sqrt{2 \cdot D/T_{frame}}$, where T_{frame} is the frame duration of the camera. By putting $D = 0.25\ \mu\text{m}^2/\text{s}$ and $T_{frame} = 0.02$ s into the calculation, we get an estimation of $\Delta v = 4.47\ \mu$m/s. An example of standard deviations of $v(x)$ can be found in Appendix A , Fig. 4.19(b). The standard deviation of $v(x)$ originates from Brownian motion of particles and is independent of the local force. Therefore $U_{velocity}(x)$ should not be expected to detect small force variations, i.e a few femtonewtons.

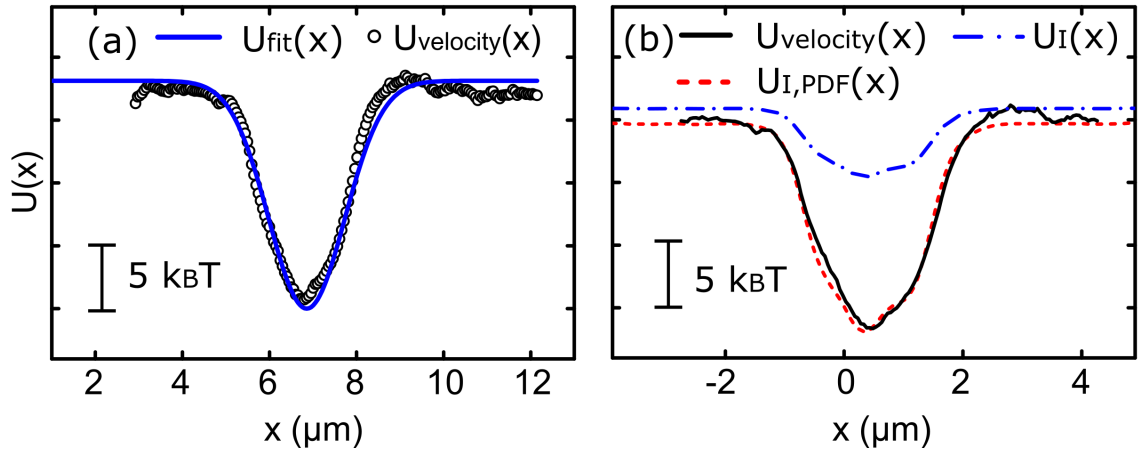

Fig. 4.8 (a) The potential energy landscape determined using the velocity profile by method (i) integrating via Eq. 2.21 ($U_{velocity}(x)$, circles) and method (ii) from the fitting Eq. 4.5 ($U_{fit}(x)$, solid line). (b) Comparison of the potential energy landscape rebuilt by the velocity of particles ($U_{velocity}(x)$, solid line) and the optical intensity distribution ($U_{I,PDF}(x)$, dashed line).

4.3 Reconstructing energy landscapes from local transition probability

4.3.1 Introduction

Trajectories of Brownian motion are collected via a range of experimental methods to rebuild the underlying potential energy landscape. For example, (i) Force spectroscopy measures the molecular extension of single proteins or nucleic acids. A conformational free-energy landscape can then be reconstructed from this data to access the folding dynamics of each single molecule [93, 94]. (ii) Fluorescence microscopy and electrophoresis are employed in DNA translocation across channels and pores to study the effect of entropic barriers [95–97]. (iii) Colloidal suspensions have been used in a wide range of studies due to their applicability to experimental time and length scales. Example studies include exploring hydrodynamic interactions [65, 98, 99], stochastic resonance [49, 50], optical ratcheting and sorting [40, 44, 100] and mimicking transport in membrane channels [51, 52, 69]. In all those cases, the system dynamics depends sensitively on the underlying potential energy landscape. However, it is difficult to accurately determine the energy landscape.

There are two conventional ways to rebuild a time-stationary potential energy landscape, denoted as $U(x)$, from Brownian trajectories. In a system at equilibrium, the Probability Density Function (PDF) of a large ensemble of single-particle trajectories relates to a Boltzmann distribution that directly reflects the underlying $U(x)$ [51, 57, 58] (details can be found in Section 2.3.1 and 4.1.3). However, many synthetic and living systems are often far from equilibrium [11, 81] and thus cannot be analysed using the PDF method. Splitting Probability (SP) has recently emerged as an alternative method that overcomes this limitation. The SP is the probability of a particle starting at $x_0 \in [a,b]$, where $[a,b]$ is the defined analysis interval, to reach a before it reaches b. It relates to $U(x)$ as described in Section 2.3.2. Thus given a large enough ensemble of single-particle trajectories which end at a or b individually, this relation can be used to reliably infer the potential energy landscape, as has recently been demonstrated in single-molecule experiments [59, 60].

However, experimental systems often contain small numbers of long trajectories and large numbers of short fragmented trajectories. Therefore they do not readily generate enough long single-particle trajectories to use the SP method. In the case of diffusion experiments at low density, video frames involving more than one particle are typically removed in order to exclude the effect of inter-particle interaction [98] on the potential energy landscape [52, 69]. As illustrated in Fig. 4.9(a), overlapped trajectories of two particles diffusing in [a,b] are removed from the initial long trajectories. This strategy generates several fragments that typically start at some point and terminate in the close vicinity, shown by black points in Fig. 4.9(b). In principle, these shorter fragments could still be treated using a SP analysis. However in practice, it is difficult to estimate for short observation intervals since the particle may not reach the interval end a or b in the trajectory fragment.

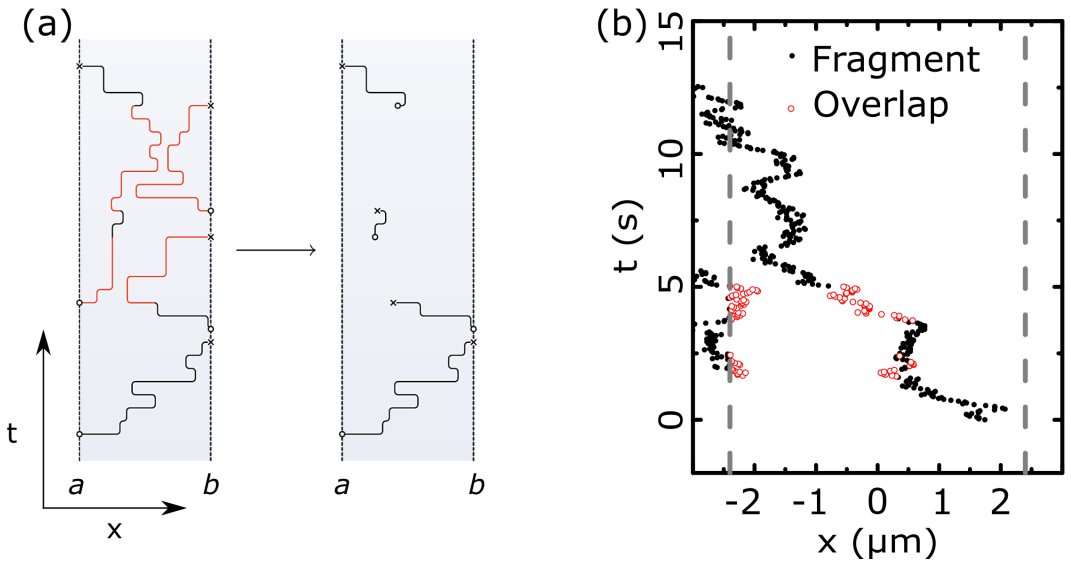

Fig. 4.9 Strategy of filtering out overlapped trajectories. (a) Sketch of removing multi-particle trajectories within region [a,b]. The overlapped trajectories (red lines) are eliminated, generating fragments of single-particle trajectories (black lines). (b) A sample trajectory of two particles diffusing in the same channel. Overlapped trajectories are removed (red circles), leaving several fragments of single-particle trajectories (black dots). The dashed lines indicate the channel ends.

In this section, a new analysis method, the Local Transition Probability (LTP) is developed to estimate $U(x)$ from fragmented trajectories, both under equilibrium and non-equilibrium conditions. Following the rules of Bayesian statistics, individual LTP is used to estimate the underlying energy landscape through a Gaussian propagator. This method is demonstrated in our colloidal channel experimental system and Brownian dynamics simulations. Compared to the SP method, our LTP method depicts the underlying $U(x)$ more accurately with less noise

from the same trajectory ensemble. Therefore, the LTP method provides a better estimate of potentials in more complex and realistic circumstances.

4.3.2 Theory

The trajectories of particles is obtained by the drag-and-release experiment as illustrated in Fig. 4.1. Using this measurement, we are able to obtain single-particle trajectories that can also be analysed with the PDF and SP approaches. This allows us to directly compare results and performance with our LTP method under realistic conditions. In total, three different trajectory analysis methods are used to rebuild the underlying potential energy landscape.

I. Probability Density Function

The PDF approach, as described in Section 2.3.1 (applicable to systems at equilibrium).

II. Splitting Probability

As a baseline for non-equilibrium methods, the SP approach earlier introduced by [59] is implemented (detailed in Section 2.3.2). Formally, $\pi(x)$ is defined as the probability of a particle starting at $x \in [a,b]$ to reach a before reaching b, as sketched in Fig. 4.10(a). $\pi(x)$, is measured experimentally by considering the two channel ends as a and b. For particles diffusing in a double well energy landscape, $\pi(x)$ to exit from the left end of the channel is presented by squares in the top panel of Fig. 4.10(a). For particles starting at the centre of the channel, they have a 50% of chance exiting from either end of the channel. However, the particles starting at the left part of the energy landscape have a higher chance to exit from the left entrance instead of jumping across the barrier then exiting from the right end. In a potential energy landscape with a constant force towards the left side, a particle has a higher chance to exit to the left end compared to the right end, as illustrated by squares in the top panel of Fig. 4.10(b). Note here, $\pi(x)$ is smoothed by a 100 nm boxcar filter to reduce noise as documented in [60].

III. Local Transition Probability

We propose a different method that roughly follows the spirit of the SP method by measuring a particle's transition event to move leftward[2]. If the particle is observed at x' one video frame time after it had been observed at x, we consider that a transition event, as illustrated in Fig. 4.10. Overall we get the LTP along x which is the probability that a particle is moving leftward one video frame later. Compared to the definition of $\pi(x)$, we can get more statistics from LTP by analysing the same trajectory ensemble. For example, LTP of particles diffusing in a double well energy landscape shows less steep changes compared to SP in the top panel of Fig. 4.10(a). In a tilted energy landscape as Fig. 4.10(b), LTP is nearly constant along

[2]The method is co-developed with Dr. Sebastian Sturm in Universität Leipzig.

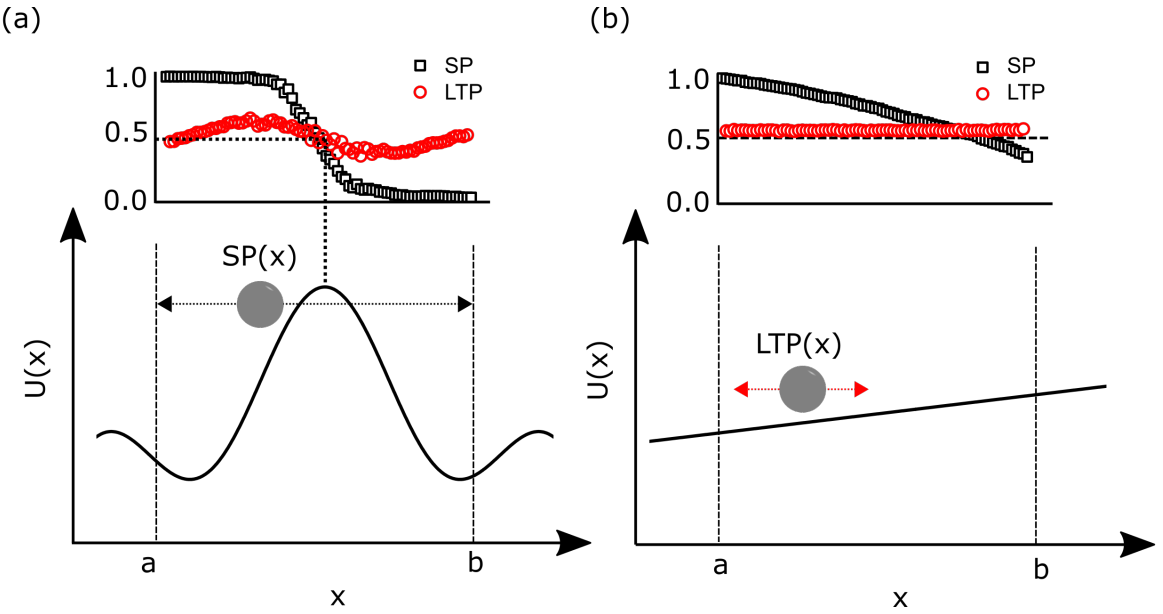

Fig. 4.10 (a) Sketch of SP in a double well energy landscape with probability profiles. SP is defined by the probability of a particle exit through the left absorbing boundary a compared to b. (b) Sketch of LTP in a tilted energy landscape with probability profiles. LTP is defined by the probability of a particle at x to diffuse to the leftwards compared to the rightwards.

x with a value slight higher than 0.5 indicating that particles have a higher chance moving towards left.

The LTP of a particle at position x, denoted as $\phi(x)$ is shown in Eq. 4.8 with the PDF of the particle $p(x)$

$$\phi(x) = \frac{\int_{-\infty}^{x} p(x)\,\mathrm{d}x}{\int_{-\infty}^{x} p(x)\,\mathrm{d}x + \int_{x}^{\infty} p(x)\,\mathrm{d}x} \tag{4.8}$$

To find the relationship between $\phi(x)$ and $U(x)$, we need to write down the average position displacement of the particle $x_{mean}(x)$ and the Mean Square Displacement (MSD) of a particle in a potential energy landscape. Assuming that the potential energy landscape is locally quadratic, the external force acting on the particle is

$$f_{ext} = F - (x - x0)\kappa + \xi \tag{4.9}$$

where F denotes the force landscape, κ is the potential's local spring constant and ξ is random thermal noise. The f_{ext} in Eq. 4.9 has to balance the drag force $\zeta\dot{x}(t)$, where ζ presents the friction coefficient. For $< x_{mean}(t) >$, the random part cancels out because $< \xi >= 0$, so we integrate

$$\zeta \dot{x}(t) = F - \kappa(x(t) - x0) \tag{4.10}$$

which gives us

$$x_{mean}(\delta x, \Delta t) = e^{-\frac{\Delta t \kappa}{\zeta}} \left(\delta \mathrm{x} - \frac{F}{\kappa} \right) + \frac{F}{\kappa} \tag{4.11}$$

For MSD ξ is important because the external force is deterministic, so the broadening of the particle density distribution comes from the random part, and unlike $< \xi >$, the squared expression $< \xi^2 >$ is not, in general zero. The fluctuation-dissipation theorem says that random thermal white noise satisfies $< \xi(t)\xi(t') >= 2\delta(t-t')k_B T\zeta$. Therefore, an extra force $A\delta(t)$ is added to Eq. 4.10 which generates a term $A\exp(-t\kappa/\zeta)/\zeta$ to the solution. The extra trajectory part caused by ξ is:

$$x_\xi(t) = \int_0^t \frac{\xi(T)\exp(\frac{-(t-T)\kappa}{\zeta})}{\zeta} \mathrm{d}T. \tag{4.12}$$

Then we square Eq. 4.12:

$$\begin{aligned} < x_\xi(t) x'_\xi(t) >= < \int_0^t \int_0^t \xi(T)\xi(T')\exp(-(t-T)\kappa/\zeta) \\ \exp(-(t-T')\kappa/\zeta)/\zeta^2 \mathrm{d}T\mathrm{d}T' > \end{aligned} \tag{4.13}$$

Because exp and ζ are fully deterministic, we take the thermal average $<>$ into the integral and get:

$$\begin{aligned} < x_\xi^2(t) >= \int_0^t \int_0^t \exp(-(t-T)\kappa/\zeta) \\ \exp(-(t-T')\kappa/\zeta)/\zeta^2 < \xi(T)\xi(T') > \mathrm{d}T\mathrm{d}T' \end{aligned} \tag{4.14}$$

Now we replace $< \xi(T)\xi(T') >$ by $2\delta(T-T')k_B T\zeta$, which removes one of the integrals and the $<>$ brackets:

$$< x_\xi^2(t) >= 2\int_0^t \frac{\exp(-2(t-T)\kappa/\zeta)}{\zeta} k_B T \mathrm{d}T \tag{4.15}$$

After integration, we get

$$MSD(\Delta t) = \frac{k_B T \left(1 - e^{-\frac{2\Delta t \kappa}{\zeta}}\right)}{\kappa} \tag{4.16}$$

The probability density of a diffusion particle is

$$p(x|x_0) = A\frac{\exp\left(\frac{-(x-x_{mean}(x_0,\Delta t))^2}{2MSD}\right)}{\sqrt{2\pi MSD}} \tag{4.17}$$

Putting Eq. 4.16 and 4.11 into Eq. 4.17, we obtain the relation between p and F

$$p(x|x_0) = A\frac{\exp\left(-\frac{\left(\coth\left(\frac{D\Delta t\kappa}{k_BT}\right)-1\right)\left((\kappa x-F)e^{\frac{D\Delta t\kappa}{K_BT}}+F-\kappa x_0\right)^2}{4\kappa k_BT}\right)}{\sqrt{2\pi}\sqrt{\frac{k_BT-k_BTe^{-\frac{2D\Delta t\kappa}{k_BT}}}{\kappa}}} \tag{4.18}$$

where Δt denotes the inverse of the frame rate and D is the particle's diffusion coefficient.

Combining Eq. 4.8 and 4.18, LTP is able to be used to estimate the force landscape F, which can be further used to get the energy landscape $U(x)$ through $F(x) = \frac{\mathrm{d}U(x)}{\mathrm{d}x}$.

4.3.3 Trajectory analysis

When we apply the LTP method to analyse particle diffusion experiment, the x axis along microfluidic channel is split in bins. Our notion of what constitutes a transition explicitly does not refer to the particle crossing the boundary from bin i to bin $i-1$, but to what we can measure experimentally: if the particle is observed at some bin $j < i$ one video frame after it had been observed at bin i, that constitutes a transition event. Using this definition, it is irrelevant whether there had been intermediate transitions between i and j, or even to the opposite direction $k > i$. We rewrite Eq. 4.8 as

$$\phi_i \approx \frac{\int_{-\infty}^{x_i-\Delta x/2} p(x \mid x_i)\,\mathrm{d}x}{\int_{-\infty}^{x_i-\Delta x/2} p(x \mid x_i)\,\mathrm{d}x + \int_{x_i+\Delta x/2}^{\infty} p(x \mid x_i)\,\mathrm{d}x} \tag{4.19}$$

where $p(x \mid x_i)$ is the PDF of particles starting at x_i diffusing along x, x_i denotes the centre of the i-th bin, Δx is the bin size, and the approximate relation between ϕ_i and its right-hand side expression becomes exact in the limit $\Delta x \to 0$.

Our approach is readily formulated in a way that can be implemented by modern probabilistic programming tools, given the experimental set of transition counts $|(i\leftarrow)|$, $|(i\rightarrow)|$

where

$$\begin{aligned}(i\leftarrow) \equiv &\{\text{video frame pairs } (n,n+1)\\ &\text{where } x(n)=i \text{ and } x(n+1)<i\},\\ (i\rightarrow) \equiv &\{\text{video frame pairs } (n,n+1)\\ &\text{where } x(n)=i \text{ and } x(n+1)>i\},\end{aligned}$$

the transition counts should follow a binomial distribution with position-dependent parameters,

$$\begin{aligned}\mathbb{P}(|(i\leftarrow)| = k \in [0,\ldots,n_i]) &= \binom{n_i}{k}\phi_i^k(1-\phi_i)^{n_i-k},\\ n_i &= |(i\leftarrow)|+|(i\rightarrow)|\end{aligned} \tag{4.20}$$

Implementing Eq. 4.19 in *Stan* [101] allows us to automatically obtain both the expectation value and the local uncertainty of $\phi(x)$ (i.e., a set of position-dependent standard deviations, means, medians, 5- and 95-percentiles) following the rules of Bayesian statistics. Finally, the estimated $\phi(x)$ is put in Eq. 4.18 and 4.19 to evaluate the force landscape and the corresponding potential energy landscape $U(x)$.

4.3.4 Results and discussion

Reconstructing potential energy landscapes from experimental trajectories at equilibrium

The three analysis methods discussed above are implemented to reconstruct potential energy landscapes at equilibrium using trajectory data extracted from experiments. $U_{PDF}(x)$ obtained from Eq. (2.16) is able to effectively depict features of the potential energy landscape where non-equilibrium forces are weak or absent, with results plotted in Fig. 4.11. We measured $U_{PDF}(x)$ for particles diffusing in a microfluidic channel with no external force applied. As expected, $U_{PDF}(x)$ [dash line Fig. 4.11(a)] is a nearly flat line in our quasi-1D channel. When line traps were generated and focused into the channel by HOTs, $U_{PDF}(x)$ clearly shows the position and the depth of the energy well. In Fig. 4.11(b), L1 represents the energy landscape with one optical line trap coupled. $U_{PDF}(x)$ here exhibits an energy well in the middle of the channel which matches the position of the line trap. In Fig. 4.11(c,d), L2 and L3 represent the energy landscapes induced by two laser line traps with different powers. The solved $U_{PDF}(x)$ shows the position and depth of the two energy landscapes.

For comparison, we applied the LTP method to reconstruct L0-L3 using the same trajectory ensembles. The energy landscapes reconstructed by the LTP approach [$U_{LTP}(x)$, solid

lines in Fig. 4.11] are close to the ones reconstructed using the PDF approach. However, the LTP approach also allows us to estimate the error associated with the landscape estimation (grey areas in Fig. 4.11).

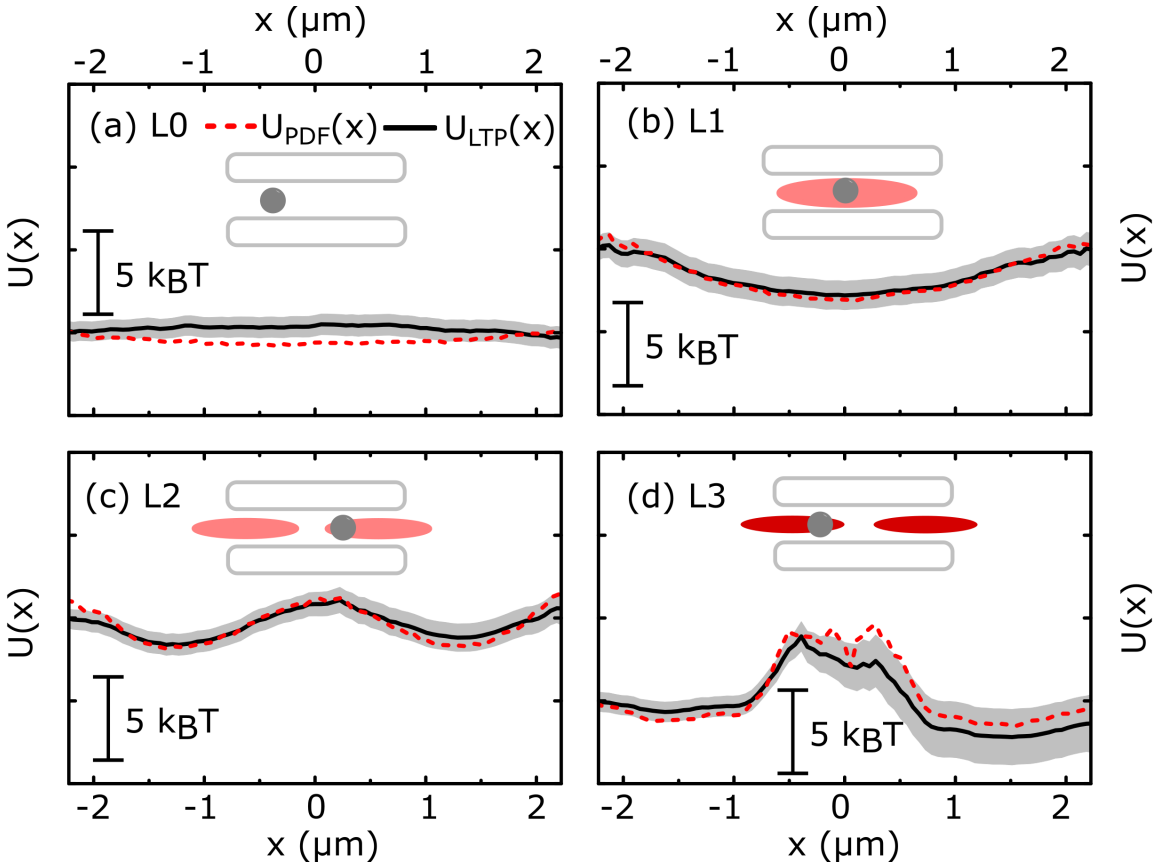

Fig. 4.11 Reconstructing potential energy landscapes from experimental trajectories at equilibrium by the PDF and the LTP methods. (a) $U(x)$ is found to be flat in a channel with no external energy landscape, labelled as L0. (b) With a laser line trap placed in the middle of the channel, $U(x)$ shows one energy minimum at the centre of the energy landscape L1. (c) Two energy minimums are found in the reconstructed $U(x)$, where two line traps are coupled in the channel L2. (d) Two line traps with higher laser power compared to L2 are imposed in the channel, with the energy landscape L3 showing two deep energy wells. The insets show the laser trap configurations in the channels. The shaded area represents the estimated standard deviation of $U_{LTP}(x)$. Note here the relative value of $U(x)$ shows the energy landscape experienced by the particle but the absolute value of $U(x)$ is meaningless.

We further compare our LTP method with the SP method under equilibrium conditions. Energy landscapes $U_{SP}(x)$ estimated via the SP approach managed to show the features of a flat potential (L1), one energy minimum (L2) and two energy minimums (L3) [circles in Fig. 4.12(a-c)]. However, $U_{SP}(x)$ exhibits large fluctuations which make the energy landscape hard to distinguish. By comparison, our LTP approach allows us to reconstruct landscapes with substantially reduced noise [solid lines in Fig. 4.12(a-c)]. Importantly, $U_{SP}(x)$ becomes invalid in the face of an energy barrier in Fig. 4.12(d). During the measurement, no particle starting near the left energy minimum exits from the right end of the channel, rendering $\pi(x) = constant$. However, $LTP(x)$ is able to pick up the moving direction of the particle and be used to calculate $U_{LTP}(x)$ [solid line in Fig. 4.12(d)].

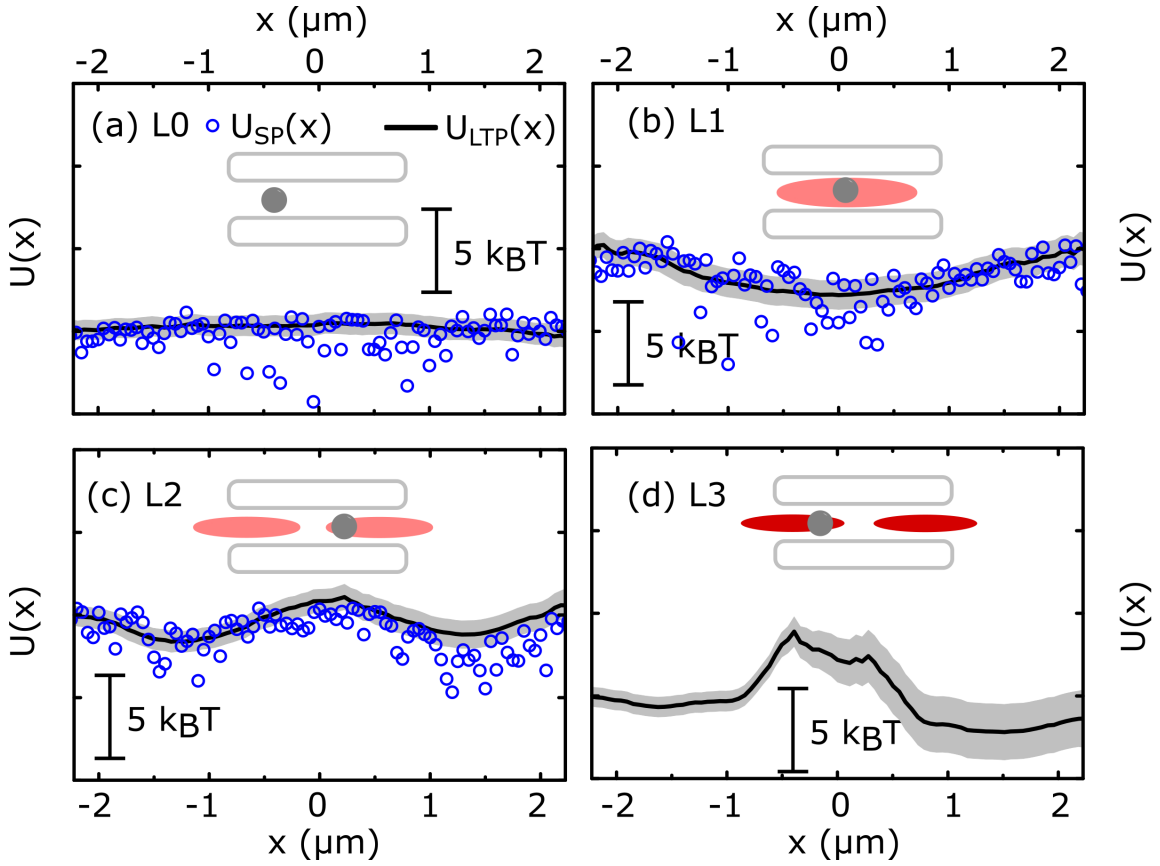

Fig. 4.12 Reconstruction of $U(x)$ from experimental trajectories at equilibrium. The underlying potential energy landscape is evaluated using the SP approach ($U_{SP}(x)$, circles), and our LTP approach ($U_{LTP}(x)$, solid lines). L0-L3 represent four different energy landscapes measured in channels. (a-c) the potential obtained from the splitting probability method $U_{SP}(x)$ agrees with our result $U_{LTP}(x)$. (d) $U_{SP}(x)$ is missing due to a constant $\pi(x)$. The insets show the laser trap configurations in the channels. The shaded area represents the estimated standard deviation of $U_{LTP}(x)$. Note: the relative value of $U(x)$ shows the energy landscape experienced by the particle but the absolute value of $U(x)$ is meaningless.

Reconstructing potential energy landscapes from trajectories in experiments out of equilibrium

Both the PDF and SP methods exhibit serious limitations when investigating systems out of equilibrium. We consider two forms of potential energy landscapes in non-equilibrium states. Firstly, no optical potential is coupled in the channel but a hydrodynamics flow exists between the two reservoirs. In the measurement reported in L4 [Fig. 4.13(a,c)], 193 particles are released at randomised starting positions along the channel, with 152 particles exiting to the left entrance of the channel and 41 particles leaving via the right entrance. In total, 80% of the particles exit through the left entrance of the channel, indicating a bias to the left direction in L4. By measuring the averaged speed of particles in the channel, we get $Pe = 0.15$ as the *Péclet* number through Eq. 4.7. A constant bias, however, does not affect the time-averaged probability density and leads to a flat position histogram, so the PDF method resolved potential appears to be flat [$U_{PDF}(x)$, dashed line in Fig. 4.13(c)]. In the measurement reported in L5 [Fig. 4.13(b,d)], 206 particles exit via the left entrance and one particle exits via the right channel entrance with $Pe = 0.92$. However, $U_{PDF}(x)$ reconstructed for L5 [dashed line Fig. 4.13(d)] still does not show the bias.

The splitting probability based $U_{SP}(x)$ is generally able to resolve $U(x)$ in non-equilibrium conditions, but requires a reliable estimation of the underlying splitting probability $\pi(x)$. $\pi(x)$ collected for L4 and L5 is plotted as squares in Fig. 4.13(a,b). In the case of a weak bias, $U_{SP}(x)$ describes the energy landscape reasonably but exhibits substantial fluctuations [circles in Fig. 4.13(c)]. In the data used for L5, $\pi(x)$ [squares in Fig. 4.13(b)] is essentially a constant $\pi(x < b) = 0$ with a data set consisting almost solely of left-exit events, which can not generate a valid $U_{SP}(x)$ via Eq. 2.19. In contrast, the potential energy landscape $U_{LTP}(x)$ reconstructed from $\phi(x)$ exhibits the bias in energy landscape L4 and L5. The strength of bias in the channel can be identified by comparing the value of $\phi(x)$ presented by squares in Fig. 4.13(a,b). Besides, slopes of $U_{LTP}(x)$ [solid lines in Fig. 4.13(c,d)] also shows the differences between the bias in two channels.

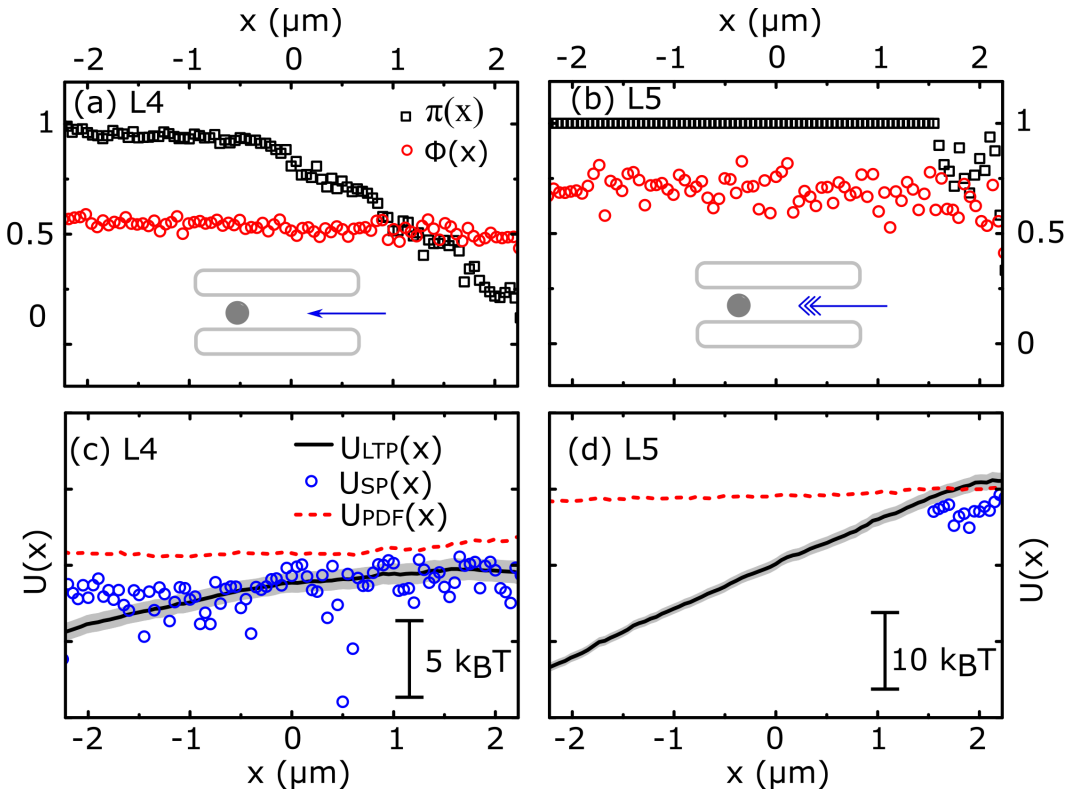

Fig. 4.13 Reconstructing potential energy landscapes from experimental trajectories in the presence of an external bias. (a,b) $\pi(x)$ measured with two channel ends set as absorbing boundaries. (c,d) Energy landscape reconstructed by three methods using the same trajectory ensemble. Dashed lines show $U_{PDF}(x)$ obtained from the PDF method, circles show $U_{SP}(x)$ obtained from the splitting probability method, solid lines show $U_{LTP}(x)$ obtained from our approach. The shaded area represents the estimated standard deviation of $U_{LTP}(x)$. Note that the absolute value of a potential energy landscape is meaningless.

Secondly, we study potential energy landscapes with external bias forces and optical potentials coupled in the channel. Not surprisingly, the same limitations of the PDF and SP methods appear on the analysis of L6 and L7, as shown in Fig 4.14. $U_{PDF}(x)$ [dashed line in Fig. 4.14] only shows the contribution of optical traps to the potential energy landscape with bias information missing. Meanwhile, few transition events detected in the opposite direction of the bias make $\pi(x)$ constant on the region between -2.2 to -1 μm in Fig. 4.14(a), which cannot be used to calculate $U_{SP}(x)$ in L6. In the measurement reported in L7, no transition to the right end of the channel makes $\pi(x)$ a constant value over the whole observation region [Fig. 4.14(b)]. $U_{SP}(x)$ is therefore invalid and missing in Fig. 4.14(d). Crucially, our LTP approach allows us to recapitulate the energy landscape successfully when a bias is superimposed on potential wells generated by laser line traps [solid lines in Fig. 4.14(c,d)].

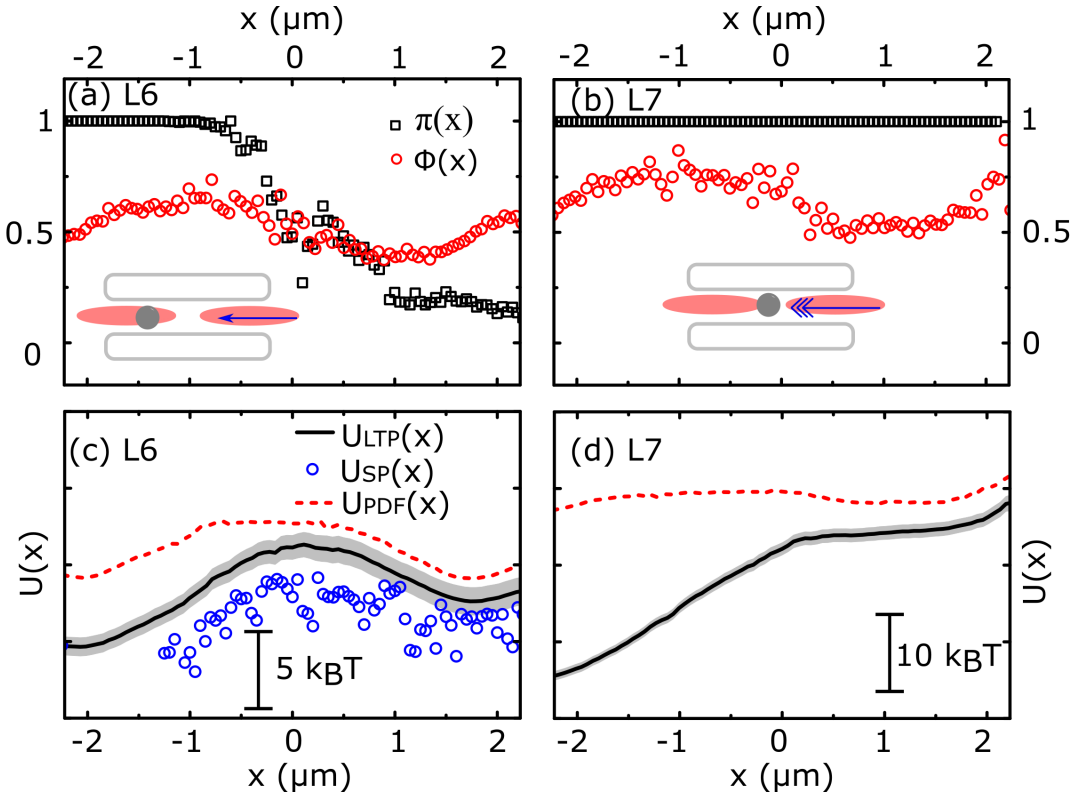

Fig. 4.14 Reconstructing potential energy landscapes from experimental trajectories in the presence of an optical potential and an external bias. (a,b) $\pi(x)$ measured with two channel ends set as absorbing boundaries. (c,d) Energy landscape reconstructed by three methods using the same trajectory ensemble. Dashed lines show $U_{PDF}(x)$ obtained from the PDF method, circles show $U_{SP}(x)$ obtained from the SP method, solid lines show $U_{LTP}(x)$ obtained from our approach. The shaded area represents the estimated standard deviation of $U_{LTP}(x)$. Note that the relative value of $U(x)$ shows the difference of the potential energy landscape.

Effect of energy barriers on the resolved potential energy landscape

In principle, larger ensemble sizes are all that is needed to obtain reliable results from the SP method. However, since the probability p of thermal activation across a potential with difference ΔU scales exponentially in ΔU, $p \propto \exp(\Delta U / k_B T)$, this solution may require exponentially more trajectories and becomes impossible to implement in practice. The SP approach fails when no particles jump through the energy barrier to touch the absorbing boundary on the other side within the experiment time scale, resulting $\pi(x) = constant$ and invalid $U_{SP}(x)$. Qualitatively, our LTP method is subject to the same caveat; energetic barriers impede the motion of a particle, thus decreases the number of observed transition events and the reliability of the obtained result. Quantitatively, however, the energy differences that must be overcome to generate the local transitions analysed by our method are much smaller than the energy differences that must be overcome to generate the non-local exit events considered by the SP method. To test this, we explicitly create a double well potential energy landscape with a high barrier in the middle, as plotted in Fig. 4.15. Within the experiment time, particles stay either at the left or the right energy well without transition through the barrier. As discussed before, rebuilding $U_{SP}(x)$ is then impractical in this situation. For the similar reason, the estimated uncertainty in $U_{LTP}(x)$ with our method [grey area in the Fig. 4.15(a)] increases much more quickly around energetic constrictions than in a flat and featureless potential. However, $U_{LTP}(x)$ matches $U_{PDF}(x)$ well when it is only calculated

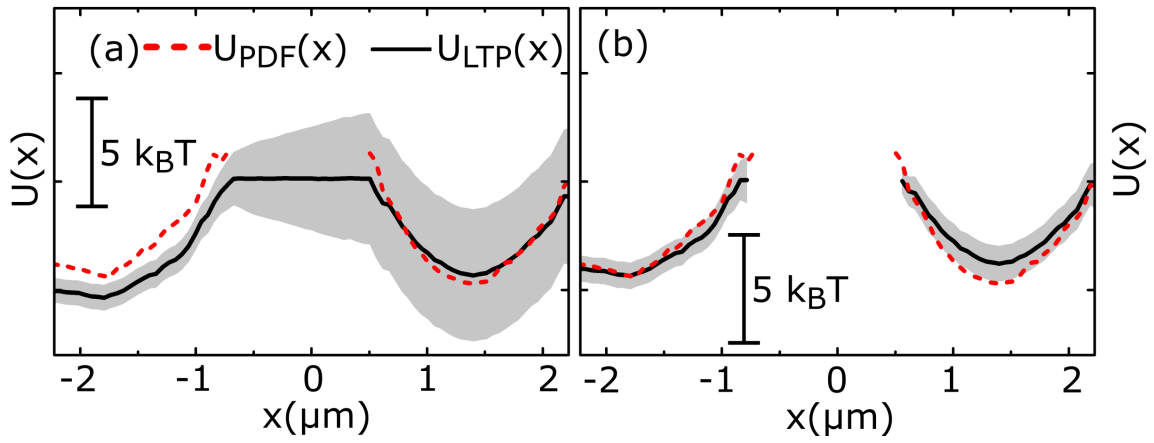

Fig. 4.15 Reconstruction of potential energy landscapes with a high barrier. $U_{PDF}(x)$ (dashed line) and $U_{LTP}(x)$ (solid line) gained from the same experimental trajectories data when calculated (a) along the whole observation region and (b) within the energy wells. The shaded area represents the estimated standard deviation of $U_{LTP}(x)$. The experiment is conducted at equilibrium. Note that the relative value of $U(x)$ shows differences of the potential energy landscape.

within the regions where trajectories are available near the energy wells, as compared in Fig. 4.15(b).

Effect of the size of trajectories on the resolved potential energy landscape

In general, one would collect more experimental data to improve the estimation of $U(x)$. We consider this for our method by using different sizes of trajectory data from the same ensemble to rebuild an potential energy landscape at equilibrium. Using the LTP algorithm, the standard deviation of $U_{LTP}(x)$ decreases with the increased size of experimental trajectory data, as demonstrated by grey areas in Fig. 4.16(a-d). However, the LTP method managed to output reasonable potential using the smallest tested number of trajectories, $U_{LTP}(x)$ plotted by a solid line in Fig. 4.16(a) using $N = 3966$ particle trajectories.

Importantly, $U_{LTP}(x)$ remains constant with different data sizes, as compared in Fig. 4.16(e). Meanwhile, $U_{PDF}(x)$ is in a good agreement with $U_{LTP}(x)$ in all the tests. However, having a small size of trajectory ($N = 3966$) makes the SP incapable of reconstructing the potential energy landscape [circles in Fig. 4.16(a)]. The results of $U_{SP}(x)$ improve with increased numbers of trajectories used for the calculation, but $U_{SP}(x)$ is still significant more noisy compared to $U_{LTP}(x)$ in all the cases.

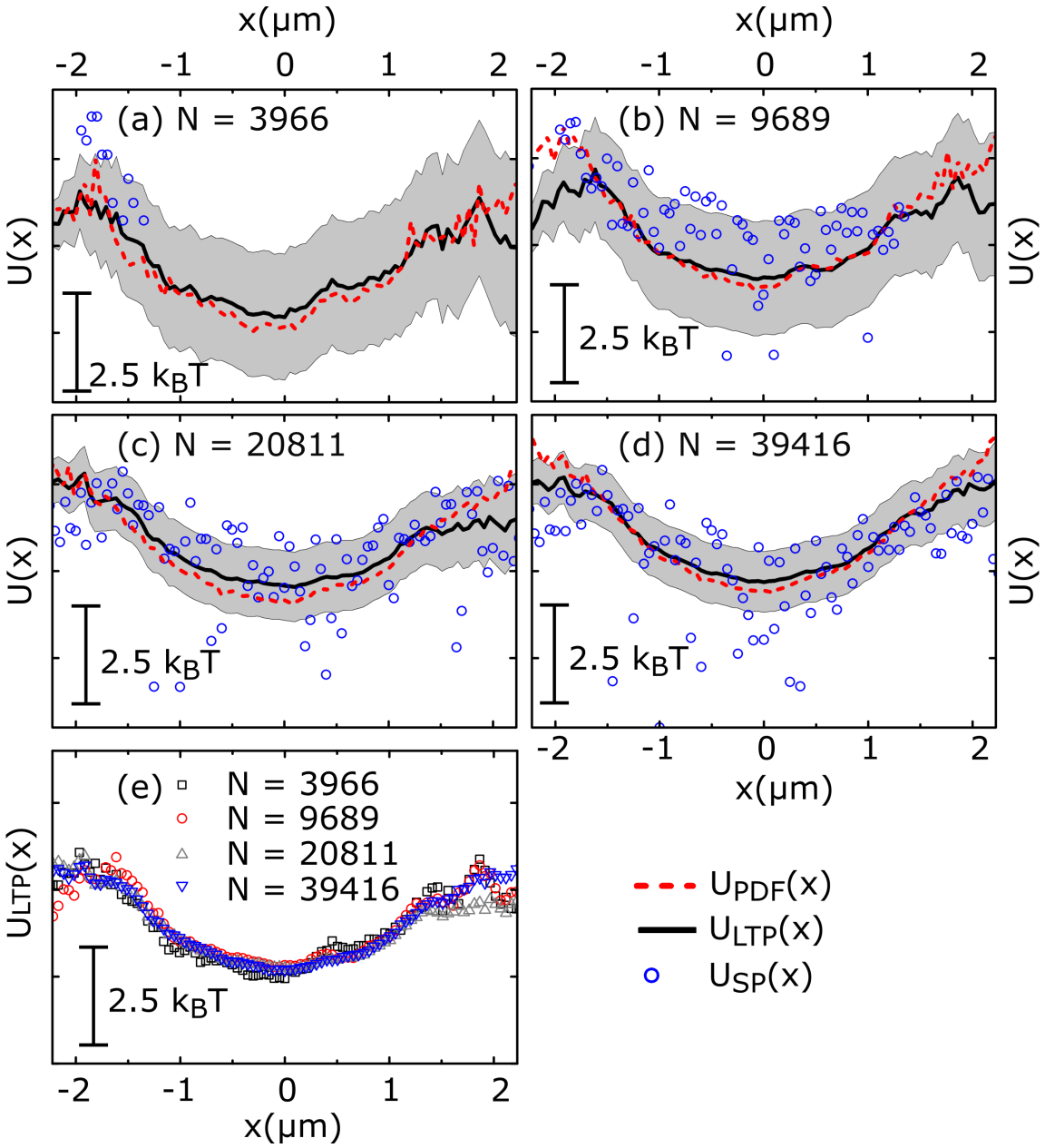

Fig. 4.16 Energy landscape reconstructed from ensembles of (a) N = 3966, (b) N = 9689, (c) N= 20811 and (d) N= 39416 experimental particle trajectories obtained by coupling a laser line in the centre of a microfluidic channel without any external bias. Comparison of the energy landscape estimated via the PDF ($U_{PDF}(x)$, dashed lines), the SP ($U_{SP}(x)$, circles) and the LTP approach ($U_{LTP}(x)$, solid lines and grey areas indicating mean and standard deviation, respectively). (e) shows the overlapping of $U_{LTP}(x)$ calculated by different N. Note that the relative value of $U(x)$ shows the difference of the potential energy landscape at different positions.

All three methods include binning the observation region x to measure the position density, the splitting probability and the local transition probability. The effect of the bin size is tested on an energy well at equilibrium with results plotted in Fig. 4.17. $U_{SP}(x)$ is affected by the bin size most severely. The fluctuation seen in $U_{SP}(x)$ becomes more significant with a smaller bin size by analysing the same trajectory ensemble (circles in Fig. 4.17). $U_{PDF}(x)$ also fluctuates more with a smaller bin size which provides less data for one bin [dashed lines in Fig. 4.17]. By comparison, the bin size on LTP analysis was found to have little effect on the rebuilt potential energy landscape and the error bar, as the solid lines and grey areas in Fig. 4.17(a-c) are almost identical.

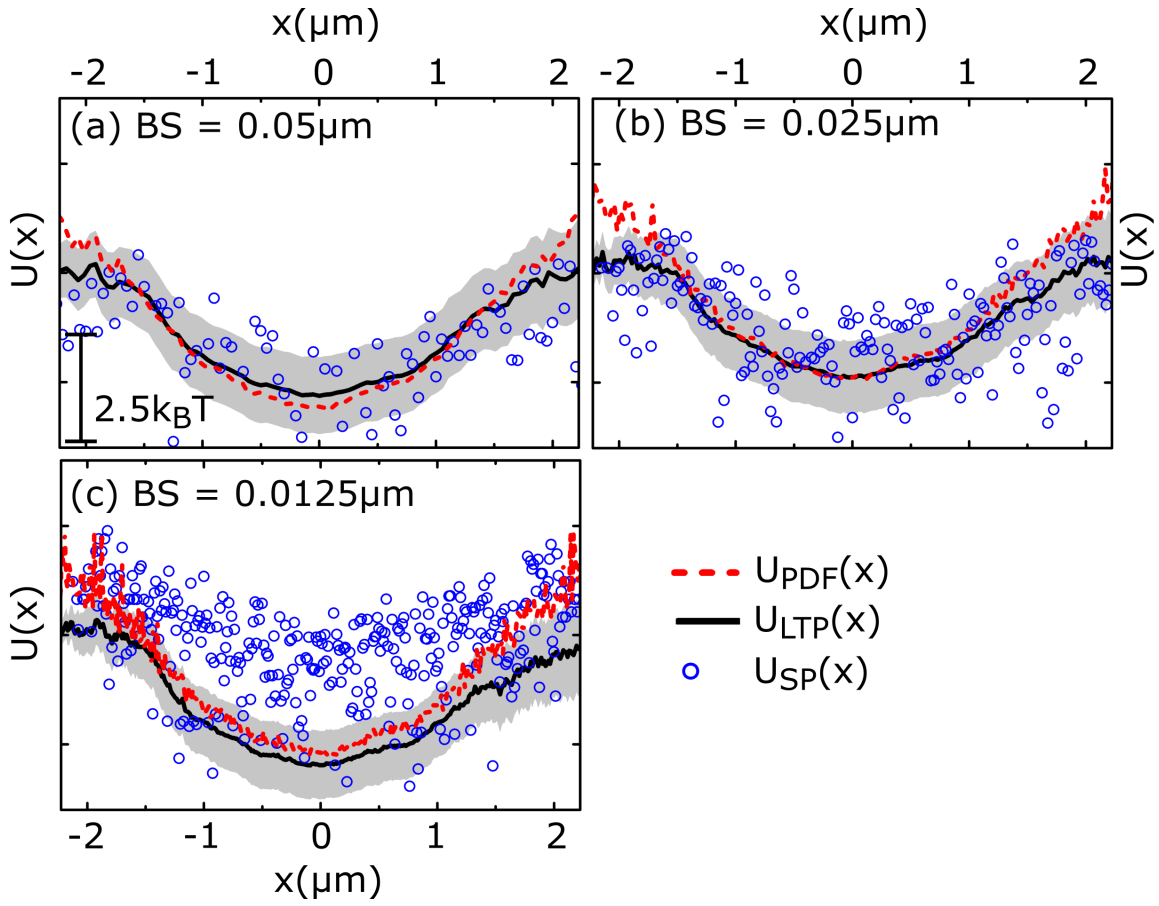

Fig. 4.17 Energy landscape reconstructed from the same ensemble of experimental particle trajectories obtained at equilibrium with a Bin Size (BS) of (a) $BS = 0.05$ μm, (b) $BS = 0.025$ μm and (c) $BS = 0.0125$ μm using the PDF ($U_{PDF}(x)$, dashed lines), the SP ($U_{SP}(x)$, circles) and the LTP approach ($U_{LTP}(x)$, solid lines and grey areas indicating mean and standard deviation, respectively). Note that the relative value of $U(x)$ shows the difference in the potential energy landscape.

4.4 Reconstructing energy landscapes with high barriers at non-equilibrium

While the optical intensity distribution method does not contain information of non-equilibrium forces, the trajectory-based method fails in reconstructing energy landscapes with high barriers. However, high energy barriers appear frequently in non-equilibrium situations, for example membrane proteins with binding sites transport solutes along the electrochemical gradients. Therefore, measuring such energy landscapes is of vital importance for understanding those transport processes.

4.4.1 Method

We combine the bias sensitive LTP analysis (Section 4.3) with calibrating the optical intensity distribution method (Section 4.1) to estimate an potential energy landscape with high energy barriers under non-equilibrium conditions. We first approximate the bias induced energy landscape $U_{LTP}(x)$ using our LTP method in a microfluidic channel without optical potentials. Then, we estimate the potential with high energy barriers and external bias by using the following equation

$$U_{I,B,PDF}(x) = U_I(x) \cdot C + U_{LTP}(x) \tag{4.21}$$

where $U_{I,B,PDF}(x)$ denotes the assessed potential, C is the scaling factor and $U_{LTP}(x)$ is the energy landscape of the bias.

4.4.2 Results and discussion

The reconstruction process consists of two steps. Step I: The drag-and-release measurements are carried out in the channel without external optical potentials. The potential energy landscape $U_{LTP}(x)$ is inferred from the LTP along x to obtain information about the bias [solid line in Fig. 4.18(a)]. As demonstrated in Section 4.3.4, $U_{PDF}(x)$ [dashed line in Fig. 4.18(a)] rebuilt through the PDF of particles does not show the bias information, but $U_{LTP}(x)$ depicts well a tilted potential with an external bias towards the right end of the channel. Here $U_I(x) = 0$ because no optical potential is imposed in the channel. Step II: optical traps are coupled into the channel by HOTs. $U_I(x)$ is calculated by putting the intensity distribution $I(x)$ into Eq. 4.1. Here $I(x)$ is generated and measured by HOTs so it does not include the information of the microfluidic environment. Finally, $U_{I,B,PDF}(x)$ is obtained by putting the scaling factor C, the measured $U_{LTP}(x)$ and $U_I(x)$ into Eq. 4.21.

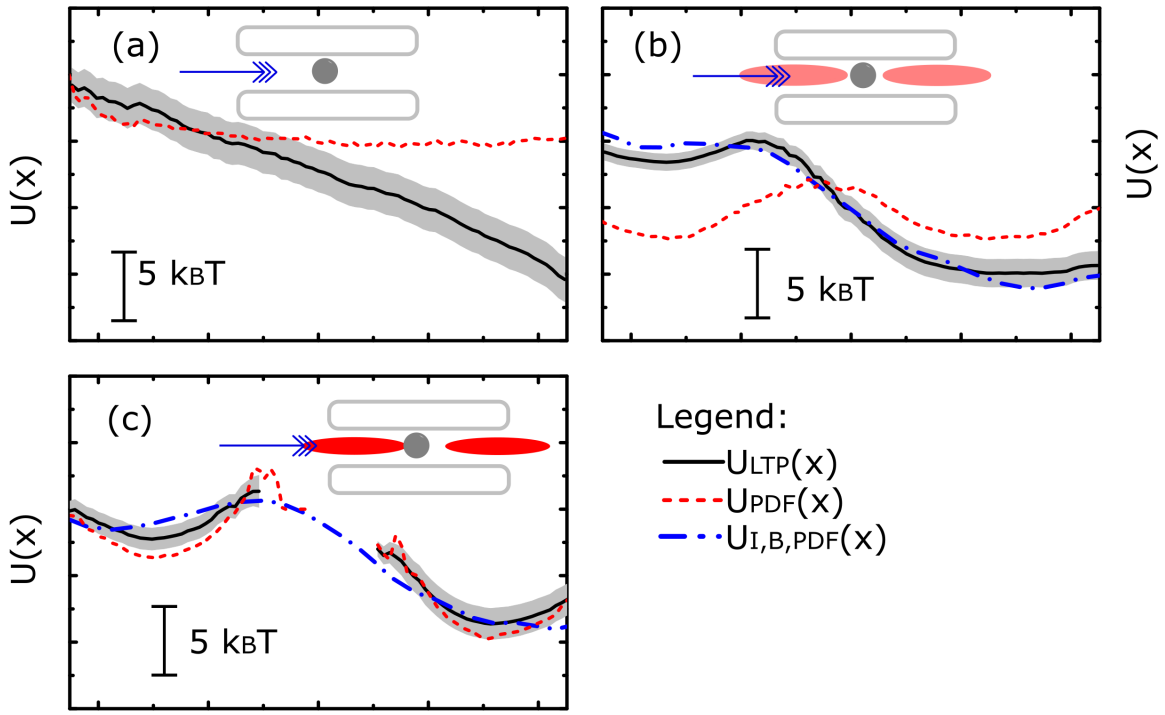

Fig. 4.18 Reconstruction of energy landscapes in the presence of energy barriers combined with bias. (a) Energy landscape in a channel with bias reconstructed via the PDF approach $U_{PDF}(x)$ (dashed line) and the LTP approach $U_{LTP}(x)$ (solid line). Note here, $U_I(x) = 0$ in this energy landscape and $Pe = 0.7$. (b) Energy landscape in a channel with bias and shallow energy barriers. Both $U_{LTP}(x)$ and the bias calibrated $U_{I,B,PDF}(x)$ accurately describe the energy landscape in the simultaneous presence of bias and shallow wells. (c) Energy landscape in a channel with bias and high energy barriers. Both $U_{PDF}(x)$ and $U_{LTP}(x)$ fail to reconstruct the energy landscape in the presence of external bias and a high barrier. The bias calibrated $U_{I,B,PDF}(x)$ manages to estimate the energy landscape. The grey shaded area represents the estimated standard deviation of $U_{LTP}(x)$. Note that the absolute values of the left and right part $U_{LTP}(x)$ is adjusted to show the agreement with $U_{I,B,PDF}(x)$. Insets show the configuration of optical potentials and the bias direction.

This method is first validated in an energy landscape with a low barrier and bias. With particles travelling along the energy landscape, our LTP method is used to reconstruct the energy landscape obtaining $U_{LTP}(x)$ [solid line in Fig. 4.18(b)] showing two energy wells with a bias force to the right end of the channel. $U_{I,B,PDF}(x)$ [dash-dotted line in Fig. 4.18(b)] obtained from Eq. 4.21 exhibits similar energy landscape compared to $U_{LTP}(x)$. The result matches the nominal potential used in HOTs, as sketched in the inset of Fig. 4.18(b). We then apply this method to reconstruct a potential with high barriers at non-equilibrium. Neither $U_{LTP}(x)$ [solid line in Fig. 4.18(c)] nor $U_{PDF}(x)$ [dashed line in Fig. 4.18(c)] work in the

energy barrier region as no particle transitions occur. Consequently, the relative difference between the left and right part of the split energy landscape is unknown. However, $U_{I,B,PDF}(x)$ [dash-dotted line in Fig. 4.18(c)] reconstructed from the intensity distribution and the bias potential manages to provide an estimation of the underlying energy landscape. The absolute values of the left and right part of $U_{LTP}(x)$ and $U_{PDF}(x)$ are adjusted to show the agreement with $U_{I,B,PDF}(x)$.

4.5 Conclusion

In this chapter, HOTs are used to modulate potential energy landscapes inside microfluidic channels and the potential energy landscapes experienced by colloidal particles are recovered by a number of methods. We first consider the methods to reconstruct potential landscapes with deep minima. An effective energy landscape is first estimated based on the intensity distribution of optical traps. This is then calibrated with a potential energy landscape inferred from the trajectories of particles. There is no high energy barrier in the potential energy landscape used for calibration purpose to obtain a valid potential from the trajectory-based methods. After obtaining a scaling factor from the calibration procedure, the optical intensity distribution is used to estimate potential energy landscapes with high barriers where few or no transitions event happen. Secondly, the energy landscape is measured independently by driving a particle in the channel under a constant force. The change of mean particle velocity relates to the potential of mean force experienced by the particle. Notably, the velocity-resolved potential matches the potential obtained by measuring the effective energy landscape from the intensity distribution of optical traps.

Next we consider methods to rebuild energy landscapes in systems out of equilibrium. We develop a new approach using the local transition probability of particles to accurately characterise stationary 1D potential energy landscapes. Our method is demonstrated in colloidal diffusion experiences and Brownian dynamics simulations, with details in Appendix B and C. Our method improves the conceptually similar splitting probability method by (i) allowing for the unbiased usage of small trajectory fragments (ii) providing us with systematic error estimates and (iii) increasing the accuracy of the obtained potential estimated at identical ensemble sizes. Experimentally, our approach demands no specialized equipment as it exclusively relies on the conventional microscopy technique, and is readily applied to single molecule measurements via fluorescence microscopy, force spectroscopy or electrophoresis.

One step further, the optical intensity method is combined with our LTP method to estimate potential energy landscape with high barriers under non equilibrium conditions. To achieve this, the potential of the bias is first resolved via LTP without external optical

potentials. Afterwards, the underlying potential is determined as the sum of the bias and the optically induced potential. Our work provides a new method to estimate potential energy landscape with high barriers which is inaccessible by trajectory based analysis methods. The knowledge of an potential energy landscape is of fundamental importance to the application of optical tweezers in sorting, optical ratcheting, stochastic resonance and measurements of reaction profile in chemistry.

Appendix

A. Energy landscape in a channel and standard deviation of the velocity profile

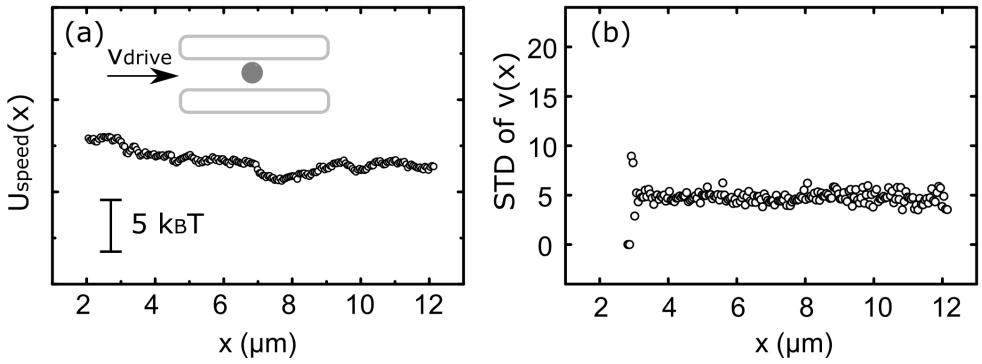

Fig. 4.19 (a) Energy landscape reconstructed from particle velocity $v(x)$ for a channel with no external potential. (b) Standard deviation of particles driving under a constant force.

B. Simulation method

Brownian dynamics simulations were carried out to compare with experimental results. The simulation of Brownian motion in a 1D channel is implemented in *Julia* based on the *msdanalyzer* algorithm proposed by [102]. External energy landscapes are added to the simulation with help from Prof. Leonardo Dagdug [37, 103]. Based on the Langevin equation (Eq. 2.7), the position of a Brownian particle x_{n+1} in a potential energy landscape $U_{MODEL}(x)$ is obtained by

$$x_{n+1} = x_n + x_{ran} + \beta \cdot D \cdot F \cdot \Delta t \tag{4.22}$$

Here, x_n is the previous position of the particle. x_{ran} is a pseudo random number generated with a Gaussian distribution with average position displacement $\mu = 0$ and standard deviation

$\sigma = \sqrt{2D\Delta t}$, which represents the random walk of the particle. D is the diffusion coefficient of the particle and assumed to be constant in the channel. $\beta = (k_B T)^{-1}$ with k_B denoting the Boltzmann constant and T denoting the absolute temperature. Force F is derived from $U_{MODEL}(x)$ through Eq. 2.6.

$U_{MODEL}(x)$ is chosen to be in line with the potential energy landscape imposed in experiments. For example, a double well energy landscape at equilibrium is modelled by $U_{MODEL}(x) = x^2 + \cos(x)$ where x is the channel longitudinal axis. In a non-equilibrium setting, a constant force is applied along x. $U_{MODEL}(x) = -B \cdot x + x^2 + \cos(x)$ is used to describe the double well energy landscape under non-equilibrium conditions. In this case, a constant force with strength B is exerting on the particle with a double well energy landscape imposed simultaneously.

During the simulation, a single particle is started at a random position chosen from a uniform distribution along the channel length. Experimentally obtained diffusion coefficient D and camera frame time Δt are used as parameters in Eq. 4.22. The first thirty positions of each particle trajectory are eliminated to exclude the effect of starting positions. Trajectories of particles are terminated at their first contact with each of the perfect absorbing boundaries, which are set at the channel ends.

C. Reconstructing synthetic potential energy landscapes from Brownian simulations

Brownian dynamics simulations are conducted as described in Appendix B. The simulation is started by letting a particle diffuse from a random position inside the channel and terminated when the particle hits one of the two channel ends. Trajectories of two hundreds particles are used to reconstruct one potential energy landscape. Under the equilibrium condition, $U_{PDF}(x)$ [dashed line in Fig. 4.20(a,b)] accurately reproduces the underlying $U_{MODEL}(x)$ [dotted line in Fig. 4.20(a,b)] for a flat potential energy landscape S1 and a sinusoid potential S2. $U_{LTP}(x)$ [solid line in Fig. 4.20(a,b)] using our LTP method gives similar results as the PDF method under the equilibrium condition and matches with the underlying potential $U_{MODEL}(x)$. By comparison, $U_{SP}(x)$ [circles in Fig. 4.20(a,b)] calculated from the SP approach comes with significant noise by analysing the same trajectory ensembles for S1 and S2.

In non-equilibrium setting S3 and S4, constant external forces are added to the energy landscape S1 and S2 in opposite directions. In energy landscape S3, $U_{MODEL}(x)$ is a tilted line with an external force pushing particle towards the left end of the region. $U_{PDF}(x)$ deviates strongly from $U_{MODEL}(x)$ in the result reported in Fig. 4.20(c). $U_{SP}(x)$ [circles in Fig. 4.20(c)] is able to resolve part of the energy landscape but becomes invalid when all the

particles exit to the left end. In energy landscape S4 plotted in Fig. 4.20(d), $U_{PDF}(x)$ exhibits the position of the energy wells but not the external force. $U_{SP}(x)$ [circles in Fig. 4.20(d)] shows a potential energy landscape matching $U_{MODEL}(x)$ with an observable amount of fluctuations in the resolved landscape. By comparison, our method $U_{LTP}(x)$ (solid lines in Fig. 4.20) accurately reproduces $U_{MODEL}(x)$ in all the tested energy landscape configurations, both in and out of equilibrium. $U_{LTP}(x)$ is in line with $U_{SP}(x)$ in all the simulations but comes with significantly less uncertainty (shaded area in Fig. 4.20).

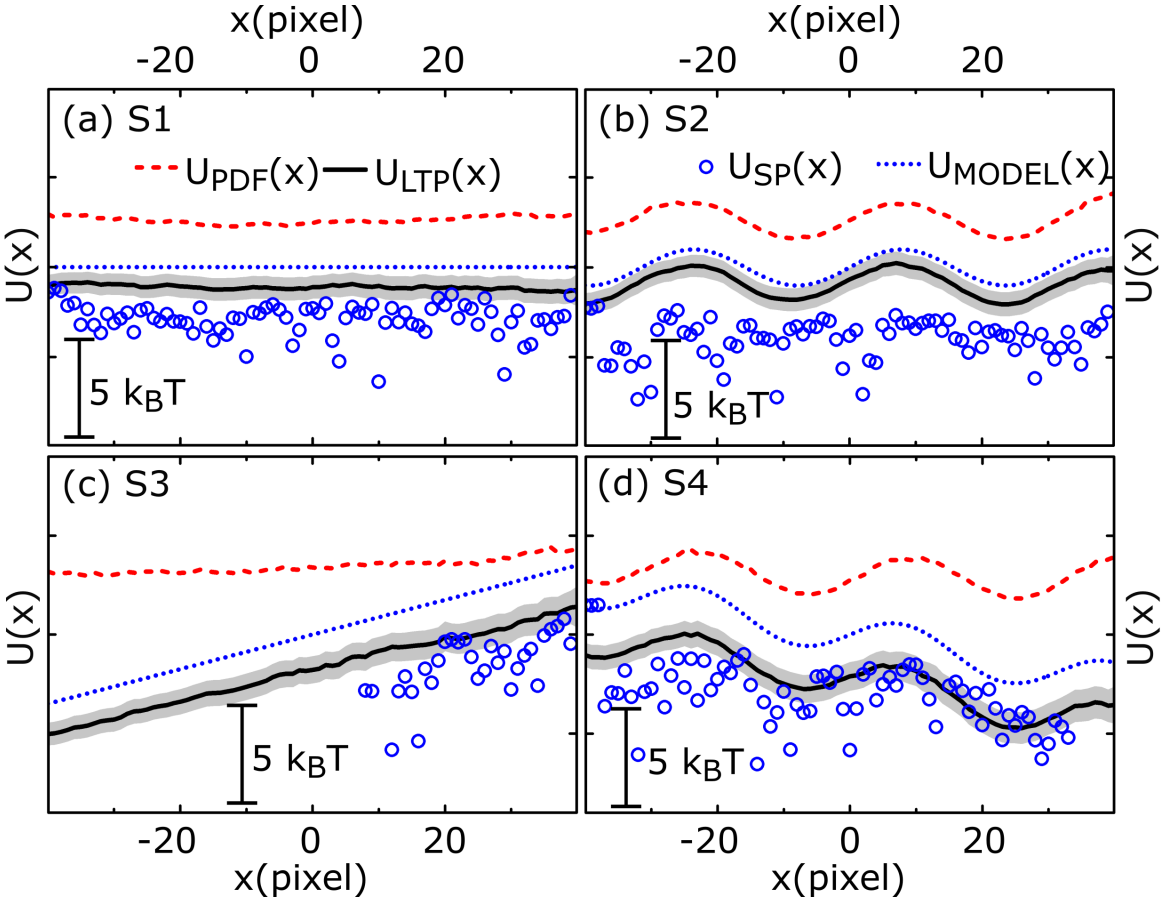

Fig. 4.20 Comparison of the energy landscape used in simulations ($U_{MODEL}(x)$, dotted lines) and the energy landscapes estimated via the PDF ($U_{PDF}(x)$, dashed lines), the SP ($U_{SP}(x)$, circles) and the LTP approach ($U_{LTP}(x)$, solid lines and grey areas indicating mean and standard deviation, respectively). (a,b) is conducted at equilibrium settings. (c,d) is conducted at non-equilibrium settings. Note that the relative value of $U(x)$ shows the potential energy landscape at different positions along the channel.

Chapter 5

Particle transport across a channel via an oscillating potential[1]

Membrane protein transporters alternate their substrate-binding sites between the extracellular and cytosolic side of the membrane according to the alternating access mechanism. Inspired by this intriguing mechanism devised by nature, we study particle transport through a channel coupled with an energy well that oscillates its position between the two entrances of the channel. We optimise particle transport across the channel by adjusting the oscillation frequency. At the optimal oscillation frequency, the translocation rate through the channel is a hundred times higher with respect to free diffusion across the channel. We also test the effect of particle concentrations in the reservoirs on the transport process.

To further investigate the stochastic gating phenomenon found in membrane transport, we oscillate the potential energy landscape stochastically by frequencies randomly chosen from exponential distributions. We find that a potential oscillating stochastically in channel enhances the translocation probability compared to a potential oscillating deterministically. Our findings reveal the effect of time dependent potentials on particle transport across a channel and will be relevant for membrane transport and microfluidic applications.

[1] Part of this chapter has been published as **Particle transport across a channel via an oscillating potential** Yizhou Tan, Jannes Gladrow, Ulrich F. Keyser, Leonardo Dagdug, and Stefano Pagliara, *Phys. Rev. E*, 96, 052401 (2017)

5.1 Particle transport in a potential energy landscape oscillating deterministically

5.1.1 Introduction

Transport proteins are ubiquitously expressed in all kingdoms of life and allow for the continuous exchange of ions and nutrients across cell membranes [8]. A feature common to all transporters is their capability to bind their substrates. The number, position and strength of the substrate-binding sites can be optimised in order to maximise substrate exchange across the cell membrane [104]. The physical mechanisms underlying transport optimisation have been extensively investigated experimentally. Crystal structure of GLUT1 has showed the existing of binding sites in glucose transporters [15, 105]; binding site has been found in LamB formed pores [106] and OmpF [16] in lipid bilayer experiments; binding effect has been demonstrated in transport of maltodextrins through maltoporin by ionic current analysis [107]; optical potential has been coupled in microfluidic channels to mimic the binding effect in channel transport in our group [51, 52]. Molecular dynamics simulation has revealed channel-glycerol hydrogen bonding interactions [22]. Meanwhile, the theory behind the binding effect has been studied by a continuum diffusion model based on the Smoluchowski equation which showed affinity for molecules helps transport in biological channels [24], a discrete stochastic model [25] which demonstrated presence of attractive binding sites in the pore can accelerate the particle current and a general kinetic model where transport is affected by inter-particle interactions in a confined space [26].

However, these studies do not take into account a fundamental hallmark shared by several transporters that is their capability to alternate their substrate-binding sites between the extracellular and cytosolic side of the membrane according to the alternating access mechanism proposed by Oleg Jardetzky in 1966 [9]. A simplified alternated particle transport mechanism can be achieved by modulating the energy landscape in which particles diffuse. To the best of our knowledge, the effect of oscillating potentials on particle transport across one-dimensional (1D) channels remains to be investigated.

In this section, inspired by the naturally occurring alternating access transport, we use our synthetic membrane experimental system [51, 52, 98] to couple a modulated potential in a quasi 1D microfluidic channel. Specifically, Holographic Optical Tweezers (HOTs) [64, 67] are used to create an optical potential that oscillates deterministically in time between the two entrances of the channel. We find that (i) there is an optimal oscillation frequency that maximises the particle transport rate through the channel; (ii) at this oscillation frequency, the particle transport rate is two orders of magnitude larger with respect to free diffusion;

(iii) the observed optimal oscillation frequency is close to the time which particles take to diffuse across the region between the centres of the energy well positions.

5.1.2 Model

We first study the effect of an imposed external energy well on particle transport across a channel in a 1D channel where particles start at a point. As sketched in the inset of Fig. 5.1(a), all the particles initiate at point B in the channel. Channel ends A and C are two absorbing boundaries which terminate the particle once it touches either side. Particle flux on the absorbing boundary is related to the starting position of the particle and has been deducted in literature [53] as:

$$\begin{aligned} J_{BA}(t) &= \frac{\pi D}{2L^2}\exp\left(\frac{v(2[\alpha-1]L+vt)}{4D}\right)\vartheta_3'\left(\frac{[\alpha-1]\pi}{2},\tilde{z}(t)\right) \\ J_{BC}(t) &= -\frac{\pi D}{2L^2}\exp\left(\frac{v(2\alpha L+vt)}{4D}\right)\vartheta_3'\left(\frac{\alpha\pi}{2},\tilde{z}(t)\right) \end{aligned} \tag{5.1}$$

where $\tilde{z}(t) \equiv \exp(-\pi^2 Dt/L^2)$, L is the channel length, v is the drift speed, D is the diffusion coefficient of the particle, α is the length ratio between AB and BC, the theta function $\vartheta_3(r,q) = 2\sum_{k=1}^{\infty}\cos(2rk)q^{k^2}$.

In an equilibrium environment, we obtain the particle flux at A and C as plotted by dashed and solid lines in Fig. 5.1(a) by putting $\alpha = 0.7/2.4$, $D = 0.25\ \mu\text{m}^2/\text{s}$ in Eq. 5.1. J_{BA} overshoots J_{BC} at the beginning of the diffusion due to the starting position B is closer to A. Then both fluxes decrease to zero as particles escape the channel eventually.

We then discuss the alternating access model in two stages. At stage I, particles start at B and diffuse freely in the channel. If the particle touches boundary C, we assume it passes the channel centre and starts diffusion again as stage II. The channel is divided into two parts as AC and CE, sketched in the inset of Fig. 5.1(b). For a translocation event, the particle first diffuses from B to C as stage I, then starts again at D and finally exits from E at stage II. By integrating J, we can get the total number of particles absorbed by a boundary which is $N = \int_0^T J\mathrm{d}t$. The translocation rate of particles through the channel can then be written down as

$$J_T = \frac{N_{BC} * N_{DE}}{2T_\Omega} \tag{5.2}$$

where T_Ω is the equivalent diffusion time for stage I and II. The calculated translocation rate is plotted in Fig. 5.1(b) with a maximum found at 4.06 s. This is worth noting here that the model simplifies the actual channel transport by excluding the process of particle diffusing into the channel and the possibility of multiple transport periods. However, it gives us a

guide line that an optimal oscillation frequency might exist. In the next section, experiment is undertaking and the relationship between the diffusion period and the particle transport is investigated in details.

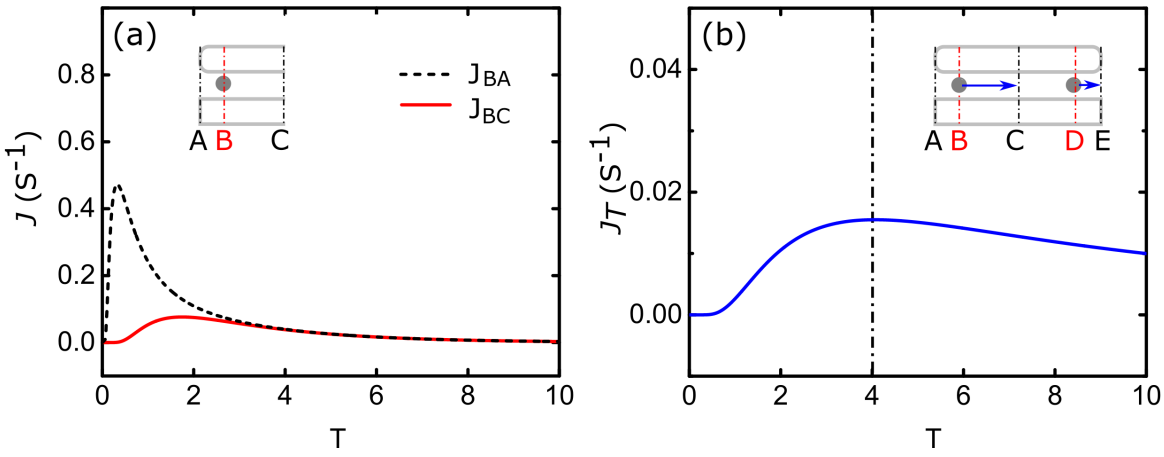

Fig. 5.1 Particle flux in 1D diffusion between two absorbing boundaries. (a) Particles start at point B within absorbing boundaries A and C. J_{BA} (dashed line) represents the particle flux at A and J_{AC} (solid line) represents the particle flux at C. (b) In a two-stage model, a particle first starts at B and terminates at C. Then it starts from D and ends at E. The translocation rate J_T from B to E is calculated by Eq. 5.2.

5.1.3 Experimental methods

Our microfluidic devices are fabricated as described in Section 3.3.3 [68, 69]. They consist of two 3D reservoirs with a depth of 12 μm separated by a Polydimethylsiloxane barrier and connected by an array of microfluidic channels. Each channel has a cross section of around 0.9×0.9 μm^2 and a length of $2L = 4.8$ μm. The reservoirs are filled with spherical polystyrene particles of diameter (510 ± 10) nm. We use a laser line trap generated by HOTs to create an attractive potential well that extends from the centre of the channel to 1.7 μm in the left reservoir [Fig. 5.2(a), (c) and dotted line in Fig. 5.2(d)]. After a time interval T_Ω, we switch off this laser line and simultaneously switch on a second laser line trap that extends, for a same time interval T_Ω, from the centre of the channel to 1.7 μm in the right reservoir [solid line in Fig. 5.2(d)]. In this way, we produce an attractive potential that oscillates at frequency $f = (2T_\Omega)^{-1}$ between the two channel entrances [Fig. 5.2(a,d)]. We estimate the extension, depth and shape of the energy wells from the intensity distribution of the line traps as discussed in Chapter 4. Experiments are performed over a range of oscillation frequencies and particle concentrations c in the reservoirs. The particle concentration in the reservoirs are estimated by the method introduced in Section 3.4.3.

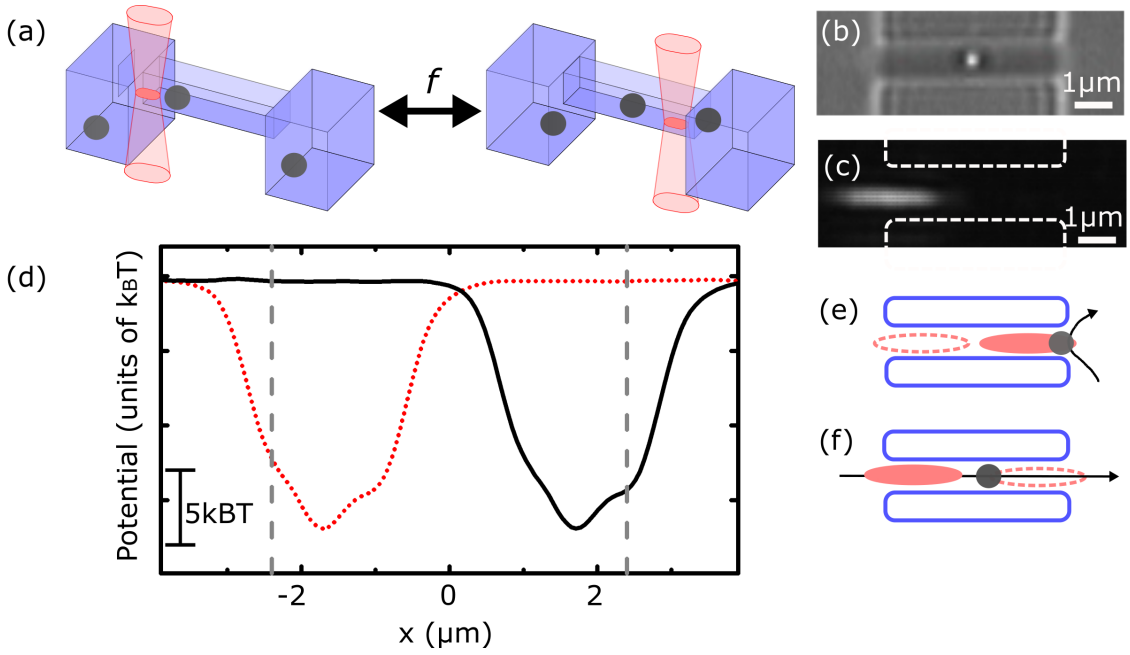

Fig. 5.2 Schematics of particle transport via an oscillating potential. (a) Schematics illustrating the oscillation of the position of a laser line trap between the left and right hand side of a channel at a frequency f. (b) Bright-field image of a polystyrene particle diffusing in a microfluidic channel. (c) Corresponding dark-field image showing the intensity distribution of a laser line trap positioned at the left entrance of the microfluidic channel. The dashed lines highlight the channel contours. (d) Oscillating energy potential created when the laser trap is positioned at the left (dotted line) and at the right channel entrance (solid line). The potential extension, depth and shape are estimated from the intensity distribution of the laser traps. The vertical lines indicate the channel entrances. (e) Schematics illustrating particle return (e) and translocation (f) events.

Videos of particles undergoing Brownian motion in the channels and reservoirs are recorded and particle trajectories are extracted (details in Section 3.4). We define an attempt as the event for which a particle enters into the channel from either reservoirs and explores it for at least 33 ms, one frame time of the camera that we use [52]. Once a particle has entered the channel, it can either go back to the same reservoir, defined as a return event [Fig. 5.2(e)], or translocate through the channel and exit to the opposite reservoir, defined as a translocation event [Fig. 5.2(f)]. We determine the attempt rate J_A which is the sum of the return and translocation events, the translocation rate J_T and the translocation probability P_T, defined as J_T/J_A. Average rate values for each oscillation frequency are obtained from at least five experiments of one hour duration each. In order to collect statistically sufficient samples for the translocation time, we use HOTs for drag-and-release experiments. In the drag-and-release experiment, a particle is first trapped in one of the reservoirs by the HOTs

[Fig. 5.3(a)]. The particle is then dragged into the channel and placed at the channel entrance [Fig. 5.3(b)]. It is released with an optical line trap generated simultaneously [Fig. 5.3(c)]. The position of the line trap is oscillating between the two channel entrances at a frequency f [Fig. 5.3(d)].

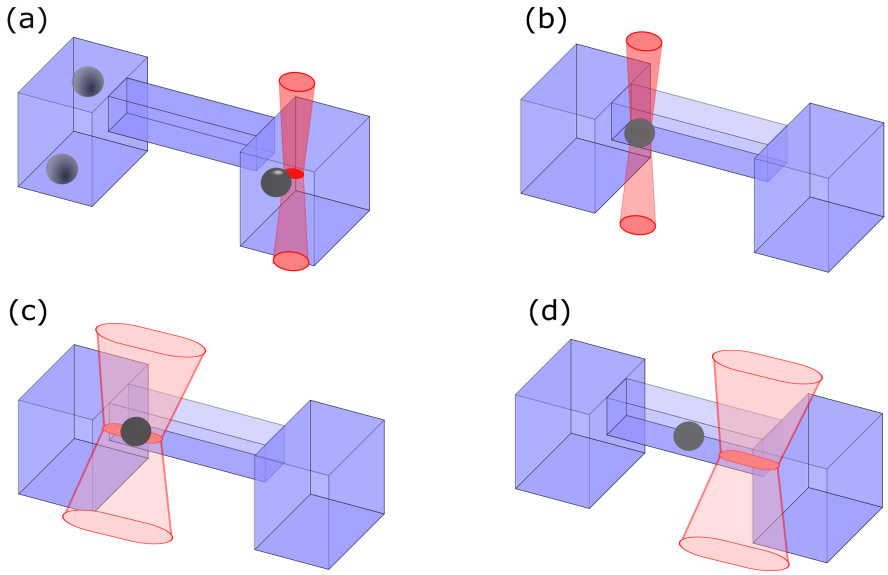

Fig. 5.3 Schematics of the drag-and-release experiment. (a) A particle is trapped in one of the two reservoirs. (b) The particle is dragged and positioned at one of the two channel entrances. (c) The particle is released from the optical trap and simultaneously a laser line is switched on at the same channel entrance. (d) After T_Ω this laser line is switched off and a laser line is switched on at the opposite channel entrance. The laser line position is oscillated at a frequency $f = 1/(2T_\Omega)$ until the particle leaves the channel. This experiment is repeated at least 300 times for each f and performed at particle concentration $c = 0.01$ nM in the reservoirs.

5.1.4 Results and discussion

Dependence of translocation rate and probability on the frequency of the oscillating potential

The effect of an oscillating potential on particle transport is first studied in a microfluidic environment in which particles are diffusing freely in reservoirs, as sketched in Fig 5.2(a). The optical potential is oscillating at frequencies f from 0.025 to 1 Hz. Three different concentrations of particles c are used for experiments. The effect of f and c on particle transport is investigated in terms of attempt rate J_A, translocation probability P_T and translocation rate J_T, with results plotted in Fig. 5.4. The rates are averaged from at least five experiments of

one hour duration. In order to better identify the peaks, an empirical two-term exponential function is used to fit P_T and J_T for each c. The fitting details can be found in Appendix A.

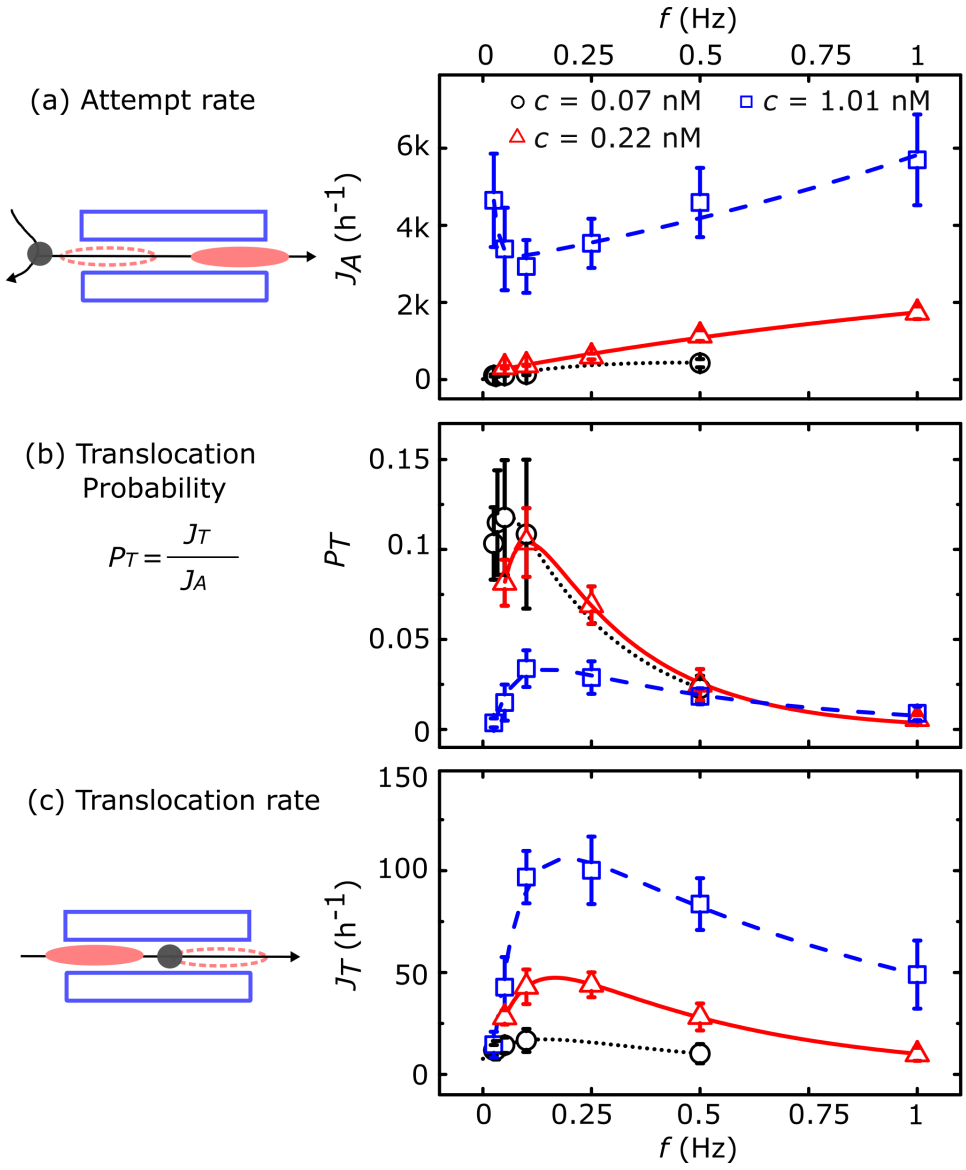

Fig. 5.4 Dependence of (a) attempt rate J_A, (b) translocation probability P_T and (c) translocation rate J_T on the potential oscillation frequency f with a particle concentration of 0.07 (circles), 0.22 (triangles) and 1.01 nM (squares) in the reservoirs. Lines are two-term exponential fitting of the data and allow identifying the following peak frequencies: 0.05, 0.10 and 0.15 Hz for P_T and 0.14, 0.16 and 0.19 Hz for J_T at c=0.07, 0.22 and 1.01 nM, respectively.

For the lowest tested particle concentration $c = (0.07 \pm 0.01)$ nM, the attempt rate J_A is (104 ± 27) particles (h^{-1}) at $f = 0.025$ Hz. It increases with the oscillation frequency up to (424 ± 105) particles (h^{-1}) at $f = 0.5$ Hz [circles in Fig. 5.4(a)]. By contrast, the

translocation probability P_T first increases with f then sharply decreases down to 0.02 at $f = 0.5$ Hz [circles in Fig. 5.4(b)]. The maximum P_T value is found at $f = 0.05$ Hz. Meanwhile, the translocation rate J_T has a weak dependence on the oscillation frequency [circles in Fig. 5.4(c)] which peaks at 0.1 Hz with 16 particles (h^{-1}) at $c = 0.07$ nM.

At higher particle concentrations, the frequency of the oscillation strongly affects particle transport across the channel. For $c = (0.22 \pm 0.06)$ nM, J_A increases nearly linearly with f up to a maximum of (1733 ± 163) particles (h^{-1}) at $f = 1$ Hz, which is nearly five times higher than J_A at $f = 0.05$ Hz [triangles in Fig. 5.4(a)]. However, P_T first increases with f and peaks at 0.1 Hz with a measured P_T of 0.1, then drops to 0.005 at $f = 1$ Hz [triangles in Fig. 5.4(a)]. Meanwhile, J_T measured under $c = 0.22$ nM shows a similar trend as P_T. J_T reaches a maximum with 43 and 44 particles (h^{-1}) at $f = 0.1$ and 0.25 Hz, then decreases to 10 particles (h^{-1}) at $f = 1$ Hz [triangles in Fig. 5.4(c)]. From the exponential fitting, P_T and J_T peak at 0.1 Hz and 0.16 Hz, respectively.

At an even higher particle concentration $c = (1.01 \pm 0.07)$ nM, J_A decreases with f from 0.025 Hz to 0.1 Hz then increases back to 5699 particles (h^{-1}) at 1 Hz. From the empirical exponential fitting results, P_T and J_T first increase and peak at an optimal oscillation frequency f of 0.15 Hz and 0.19 Hz respectively, and then both decrease for higher f [squares in Fig. 5.4(b) and (c)].

Overall, we find that J_A and J_T increase with c for all the tested oscillation frequencies f [Fig. 5.4(a,c)], but this is not the case for P_T. In the result plotted in Fig. 5.4(b), the maximum P_T at $c = 1.01$ nM (squares) is about three times lower than the maximum P_T at $c = 0.07$ nM (circles) and 0.22 nM (triangles). Interestingly, P_T shows a maximum value for f close to 0.1 Hz for all three tested particle concentrations.

Moreover, we compare particle transport in an oscillating potential to transport in a channel without external potentials and a channel with a stationary potential at $c = 0.22$ nM in Fig. 5.5. In the channel without an external potential, particles enter the channel by free diffusion. Without the help of an attractive potential at the channel entrances, J_A and J_T are as measured as 85 and 0.4 particles (h^{-1}) [dashed lines in Fig. 5.5(a,c)].The stationary potential has the same extension but 42% smaller depth with respect to the oscillating potential. The reduced depth avoids channel jamming in the presence of a static potential (details in Appendix B). In the presence of a stationary potential, J_A and J_T reach 447 and 23 particles (h^{-1}) [dotted lines in Fig. 5.5(a,c)]. By comparison, J_A in an oscillating potential [triangles in Fig. 5.5(a)] overtakes J_A in the stationary potential for $f \geq 0.25$ Hz. In terms of J_T, the value measured in the oscillating potential at the optimal oscillation frequency $f = 0.1$ Hz is 102 times higher than the one measured in free diffusion [dashed line in Fig. 5.5(c)] and twice the one measured for a static potential constantly switched on [dotted lines in Fig. 5.5(c)].

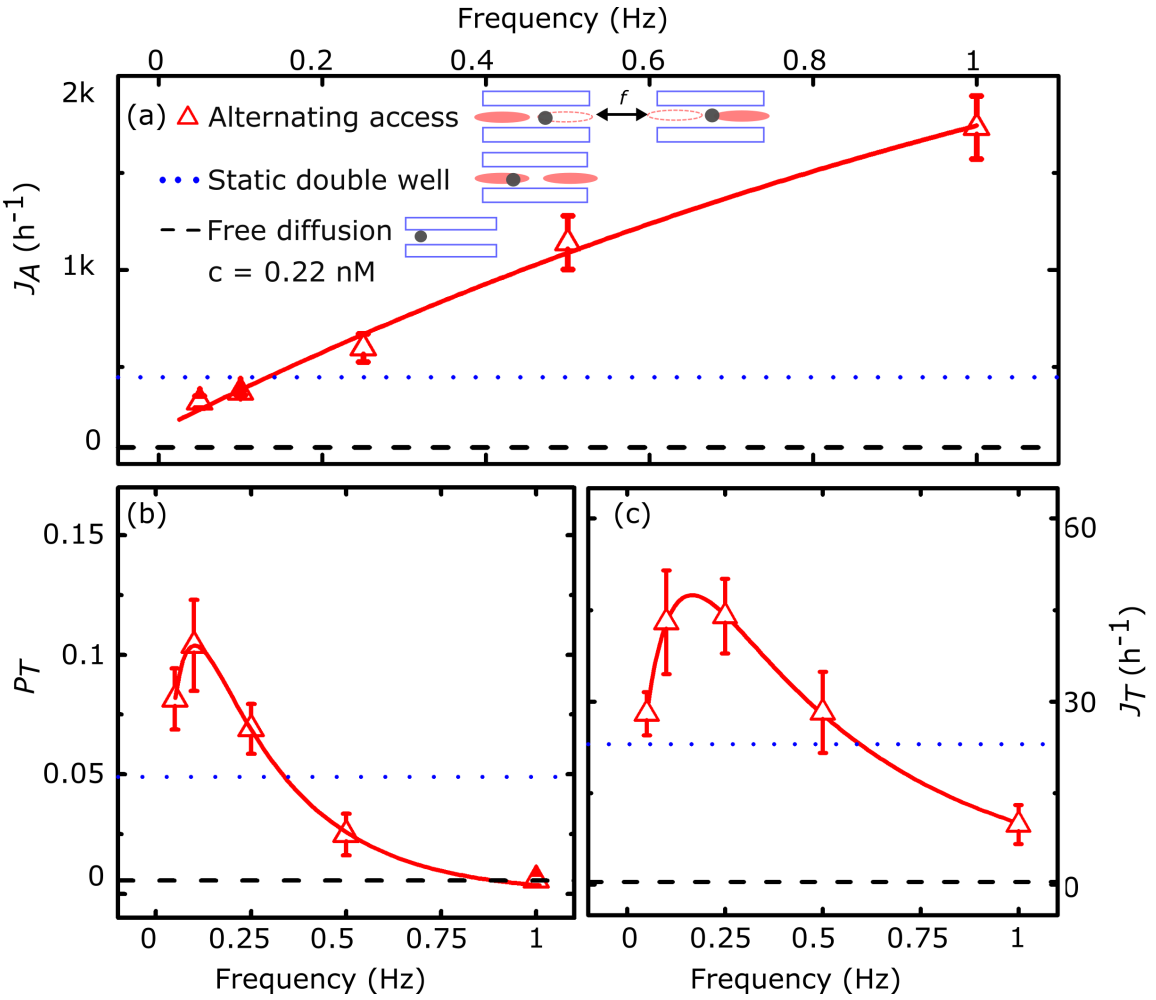

Fig. 5.5 Comparison of (a) attempt rate J_A, (b) translocation probability P_T and (c) translocation rate J_T between the oscillating potential configuration (triangles), a static potential with two energy wells with the same extension but 42% smaller depth with respect to the oscillating potential (dotted line) and a channel without optical potential coupled (dashed line).

P_T in the oscillating potential at $f = 0.1$ Hz [triangles in Fig. 5.5(b)] is 2.5 times higher than the one measured in the stationary potential [dashed line in Fig. 5.5(b)] and 20 times higher the one in the channel without external potential [dotted line in Fig. 5.5(b)]. For c = 1.01 nM at $f = 0.1$ Hz, J_T [squares in Fig. 5.4(c)] is 65 times higher than in free diffusion and 4 times higher than in the presence of the static double well potential. The details of particle transport in a channel without an external potential at different c can be found in Appendix C.

Dependence of the channel translocation time on the frequency of the oscillating potential

In order to have a better understanding in the aspect of single particle diffusion, we perform drag-and-release experiments to measure the translocation times of single particles across the channel. The experiment method is illustrated in Fig. 5.3 and repeated at least 300 times for each f at $c = 0.01$ nM. The low c ensures that particles rarely diffuse into the channel by free diffusion. During experiments, a particle is released at the left channel entrance and a translocation is defined as the particle exiting from the right channel entrance.

We first measure the distribution of the experimentally collected translocation times for each particle under an oscillating potential with result plotted in Fig. 5.6. We find resonance-like peaks with the first maximum located at 40.5, 20.5, 10.5 and 4.5 s for $f = 0.025, 0.05, 0.1$ and 0.33 Hz, respectively [red bins in Fig. 5.6(a-d)]. Interestingly, the position of the first peak is the inverse of the oscillation frequency used in experiment. For example, the first peak (10.5 s) in Fig. 5.6(c) is very close to the inverse of the oscillation frequency (0.1 Hz). By averaging six sets of independent measurements obtained in the drag-and-release experiments, P_T is normalised and plotted as a function of f in Fig. 5.6(f). We find that P_T is maximised at $f = 0.1$ Hz.

To have a better understand of the diffusion process, Brownian dynamics simulations in a 1D channel with length $2L$ are performed using the experimentally measured oscillating potential[2]. Particle trajectories start at $-L$ and are terminated at their first contact with each of the perfect absorbing boundaries set at $-L$ and L that are the channel entrances. We measured the fraction of particles that end at $L/2$ as well as their transit time defined as the time that a particle takes to reach L for the first time. The actual position of a particle, x_{n+1}, is given by $x_{n+1} = x_n + x_{ran} + \beta D_c F \Delta t$, where x_n is the previous position, x_{ran} is a pseudo random number generated with a Gaussian distribution with average position displacement $\mu = 0$ and standard deviation $\sigma = \sqrt{2D_c\Delta t}$, $\beta = (k_B T)^{-1}$and force F was derived from the measured potential [Fig. 5.2(d)]. When running simulations we set $\Delta t = 1 \times 10^{-4}$ s and we average over 100 millions random walkers. For a particle in free diffusion in the channel, the translocation time calculated according to Eq. 2.14 [54] using $L = 2.4$ μm and D_c = 0.25 $\mu m^2/s$ [75], is 15.36 s. This is in agreement with the value obtained via Brownian simulation (14.99 s).

During simulations, the potential starts oscillating at a frequency of f once the particle is released. The distribution of the translocation times collected in simulations is plotted for different f in Fig. 5.7. As we can see, the distributions show similar harmonic peaks as their experimental counterpart (Fig. 5.6). Boarder peaks appear before the first harmonic peak in

[2]Brownian motion simulations were carried out by Prof. Leonardo Dagdug.

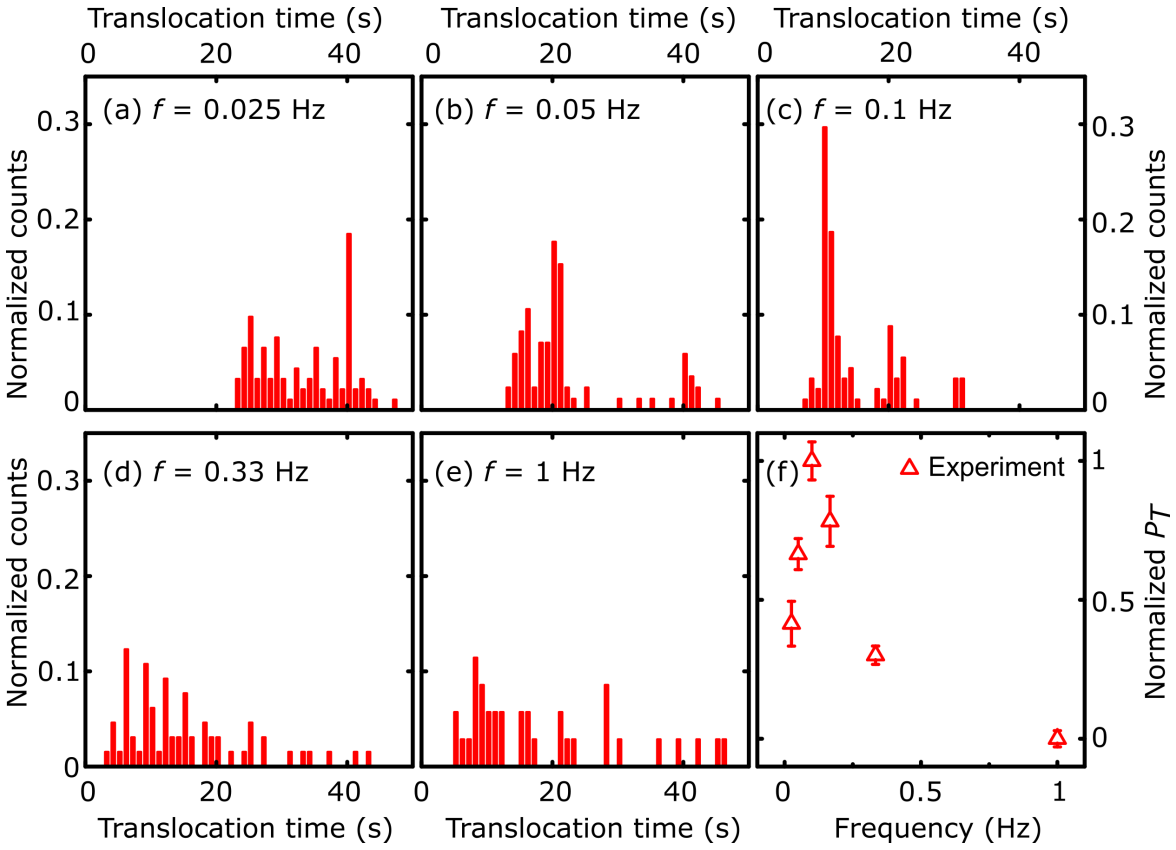

Fig. 5.6 Experimental translocation time distribution on oscillation frequency. (a-e) Histograms reporting the normalised distribution of translocation times (red bars) measured in drag-and-release experiments at $c = 0.01$ nM for different potential oscillation frequencies f. (f) Experimental (triangles) translocation probability P_T normalised to their maximum values. Experimental P_T is the mean of six sets of 50 independent measurements obtained in drag-and-release experiments.

Fig. 5.7(a,b). The appearance of those peaks is due to the relative position of the absorbing boundaries to the channel ends, which is discussed in Appendix D. It is worth noting that the harmonic peaks are also found at $f = 1$ Hz [Fig. 5.7(e)] in the simulation result, but not the experiment result [Fig. 5.6(e)] due to lack of translocation events for $f = 1$ Hz in experiment. Importantly, our Brownian dynamics simulations confirm the frequency dependence of the translocation probability with an optimal oscillation frequency of $f = 0.125$ Hz close to the experimentally measured one [dots and triangles, respectively, in Fig. 5.7(f)].

For comparison, we also measured translocation times of particles at different c and f for experiments with particles diffusing freely into the channel, which has been discussed in Fig. 5.4. The distributions of translocation times are plotted in Fig. 5.8. At the optimal oscillation frequency $f = 0.1$ Hz, harmonic peaks starting at 10 s are found in all three

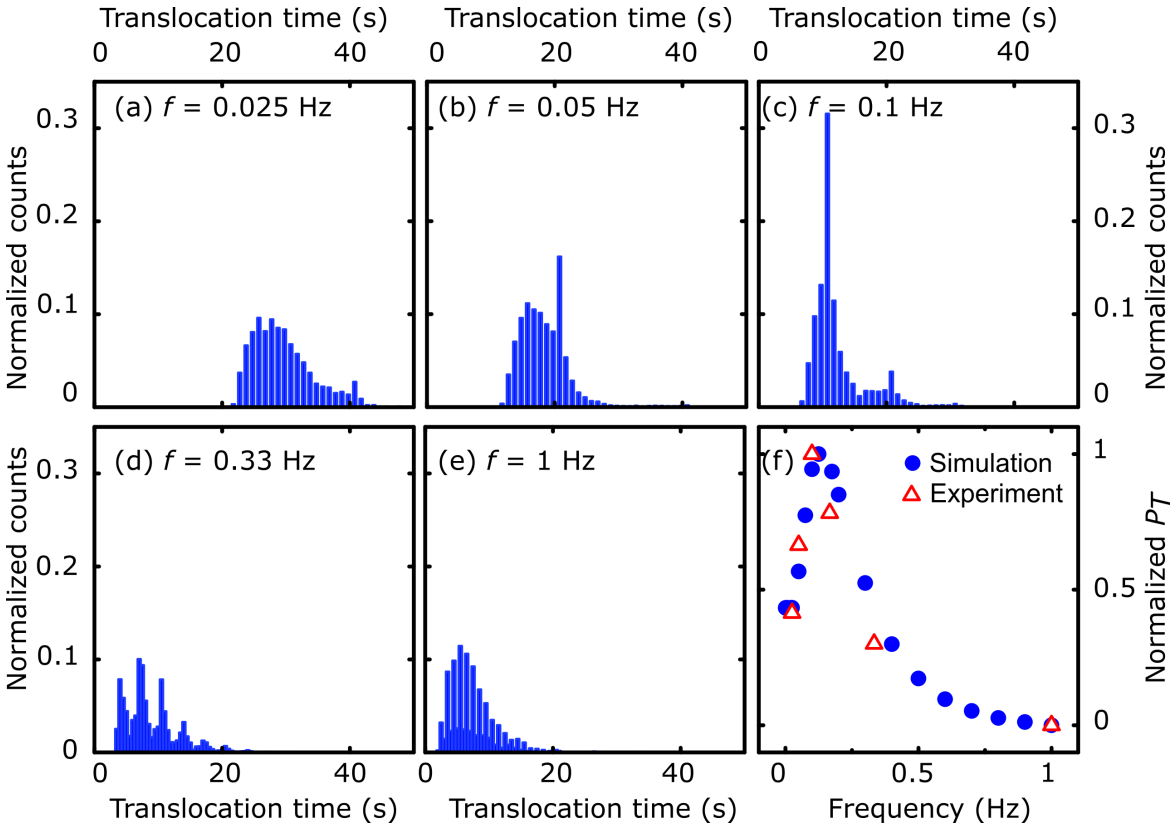

Fig. 5.7 Time distribution of simulated translocation events on the oscillation frequency. (a-e) Histograms reporting the normalised distribution of translocation times measured via Brownian dynamics simulations (blue bars) for different potential oscillation frequencies f. (f) Experimental (triangles) and simulated (circles) translocation probability P_T normalised to their maximum values.

concentrations [Fig. 5.8 (a-c.ii)]. However, we can not identify any harmonic peak in other oscillation frequency in the rest of the results.

Explanation of the observed optimal oscillation frequency

An intuitive explanation of the optimal oscillation frequency is provided by measuring the transition times across portions of the channel. Firstly, let us consider a representative translocation from the left to the right reservoir. Upon entering the channel, the particle may diffuse to the minimum of the left attractive potential well, while the left laser line is switched on [Region I in Fig. 5.9(a)]. The particle is trapped close to this position until, at $T_\Omega = (2f)^{-1}$, the left laser line is switched off and the right line is turned on. At this time the particle is free to diffuse either towards the left or right entrance of the channel. In the most efficient scenario in terms of particle transport, the particle travels in free diffusion across

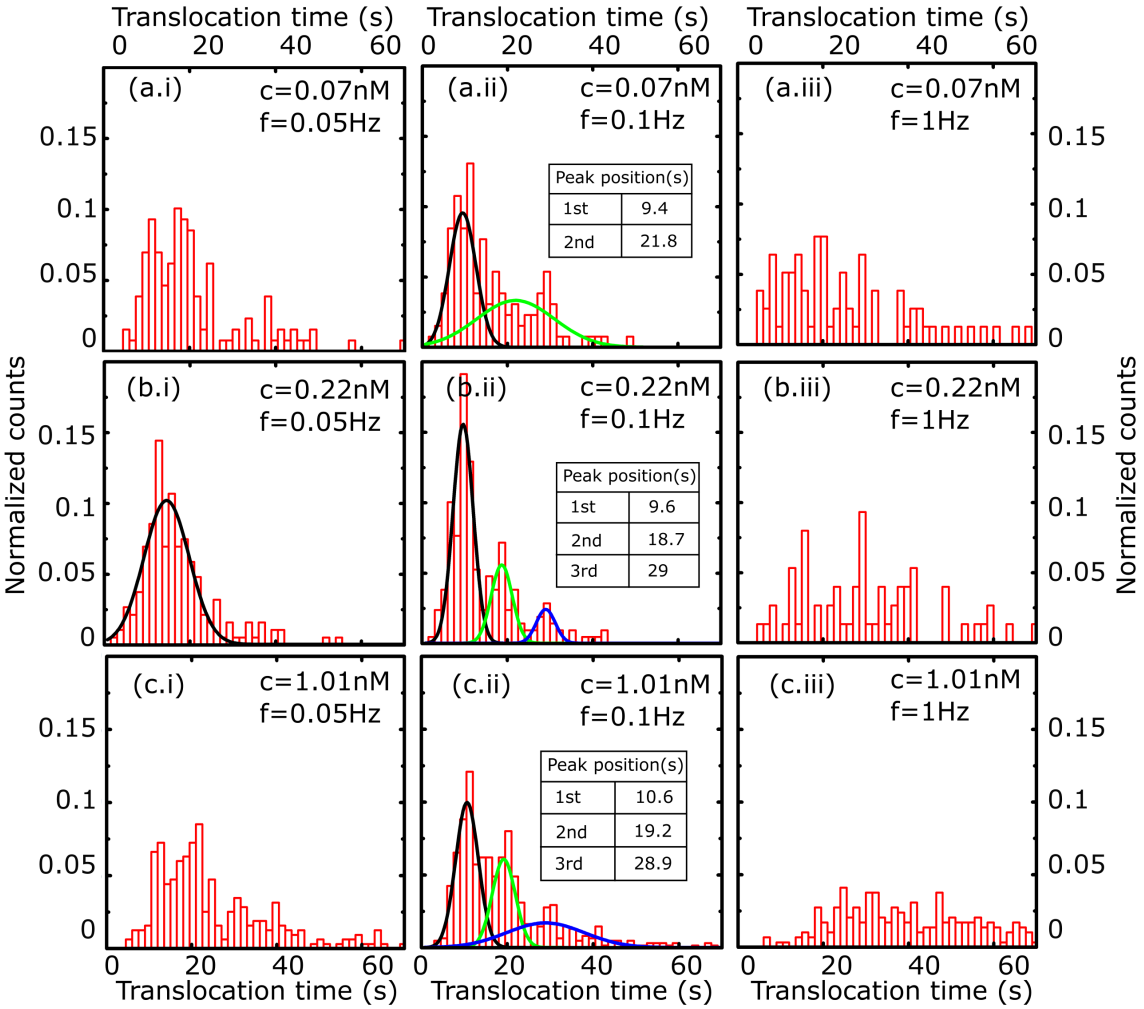

Fig. 5.8 Histograms reporting the experimental distributions of translocation times for $f = 0.05$ Hz, 0.1 Hz and 1 Hz (from left to right) and c = 0.07 nM, 0.22 nM and 1.01 nM (from top to bottom). The distributions are fitted with Gaussian functions (solid lines) allowing for the extrapolation of harmonic peaks. The insets report the harmonic peak positions obtained by fitting Gaussian functions.

region II [Fig. 5.9(b)] and region III where it reaches the right-hand side potential minimum when the right laser line is still on [Fig. 5.9(c)]. Finally, when this line is switched off the particle is free to diffuse through region IV out of the channel [Fig. 5.9(d)].

We perform drag-and-release experiments to evaluate the transition time across each of the four regions above. The particle's direct transition time by free diffusion in channel portions of different length is plotted in Fig. 5.10(a). The experimental values match the theoretical predictions according to Eq. 2.14, further demonstrating that our system is close to the 1D scenario. The direct transition time through region II and III is $T_{II\&III} = 2.8$ s at the

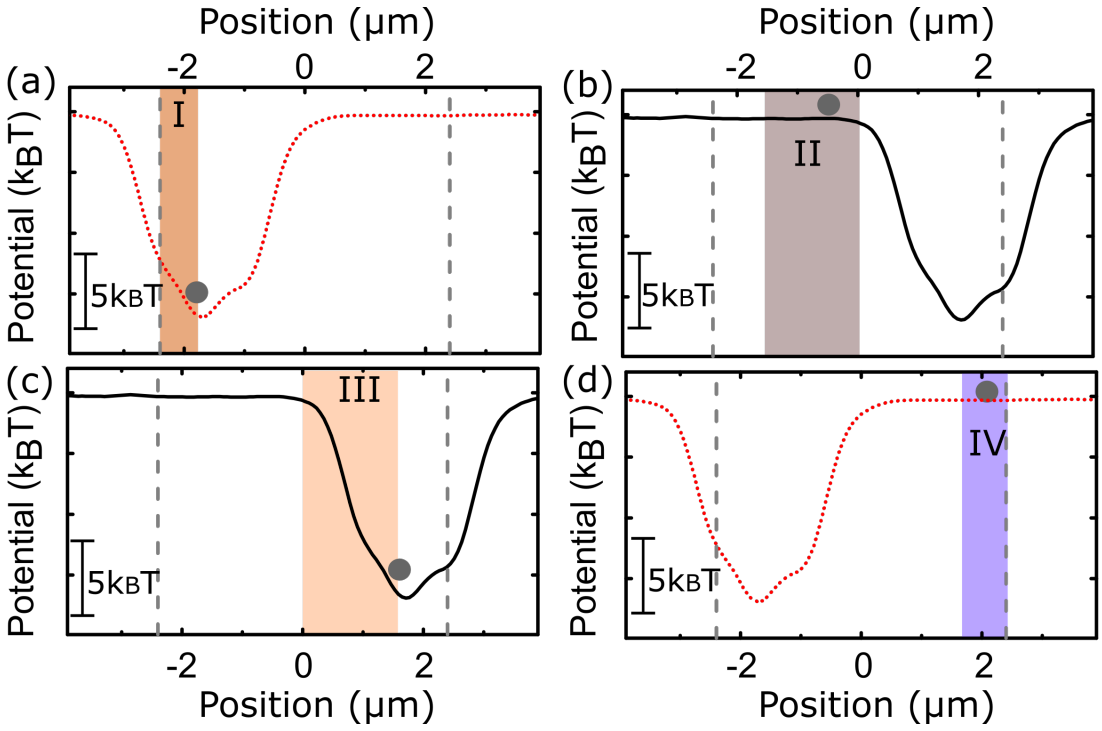

Fig. 5.9 Schematics illustrating a representative translocation from left to right in the presence of an oscillating potential. (a) A particle enters the left entrance of the channel when the laser line is on at the left channel entrance and diffuses through region I to the attractive well energy minimum. (b) The left laser line is switched off and simultaneously the right one is switched on, the particle freely diffuses through region II. (c) The particle diffuses through region III into the minimum of the right attractive energy well. (d) The laser line at the right entrance is switched off and the one on the left switched on and the particle diffuses through region IV and out of the channel.

oscillation frequency $f = 0$ Hz (Fig. 5.10(b), that is when a particle is released from the HOTs at the left entrance of the channel with the right-hand side potential constantly on). $T_{II} = 1.61$ s at $f = 0$ Hz is smaller than the corresponding $T_{tr} = 1.95$ s calculated according to Eq. 2.14 due to the presence of the external potential. $T_{III} = 1.02$ s at $f = 0$ Hz is in agreement with the value calculated according to Eq. 2.15 ($T_{tr} = 1.13$ s) by using the experimentally measured potential. $T_{II\&III}$ is close to $T_\Omega = 5$ s indicating that the optimal oscillation frequency is the one that is close to the transition time through regions II and III. Notably, for f higher than the optimal oscillation frequency, particle's transition through regions II and III is interrupted by the potential oscillation. For f lower than the optimal oscillation frequency, a particle has a higher chance to exit the channel through region I resulting in a return event, although the chance for a particle to be transported through regions II and II is increased. Overall for frequencies different from the optimal frequency, particle diffusion through regions II and III

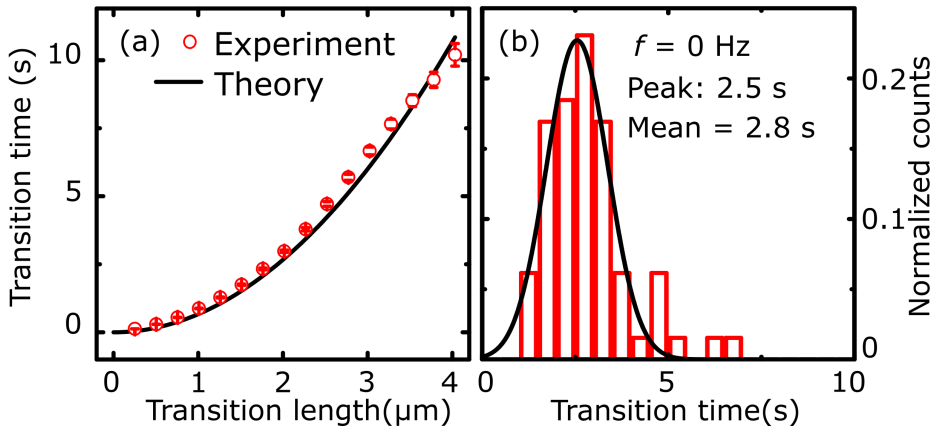

Fig. 5.10 Calculated and measured direct transition time. (a) Transition times of a freely diffusing particle through portions of the channel of different lengths. The experimental values (circles) are mean and standard errors of the values obtained in 200 experiments. The theoretical values (line) are calculated according to Eq. 2.14 by using experimentally measured parameters. (b) Distribution of transition times through regions II and III for $f = 0$ Hz, measured by performing drag and release experiments at $c = 0.1$ nM. The peak position is obtained by fitting the data with a Gaussian function.

does not synchronize with the time scale defined by the oscillation frequency. This explains the observed decrease in translocation rate and probability at f lower and higher than the optimal frequency (Fig. 5.4). Besides this argument, the optimised oscillation period 5 s found in our experiment is close to our estimation 4s in the 1D diffusion model as discussed in Section 5.1.2. Furthermore, we solve the Fokker-Planck equation numerically in Appendix E, which supports our explanation that the optimal oscillation frequency matches the particle diffusion across the region between energy wells in the channel.

5.1.5 Conclusion

Optical potentials modulated in time have been extensively employed to direct particle motion [38–50], including in microfluidics applications [44]. However, these have yet to be implemented for enhancing particle transport across a quasi-1D microfluidic channel connecting two reservoirs. In this section we created a modulated optical potential consisting of a laser line that alternates its position between the two entrances of a microfluidic channel at constant frequencies. We optimised the oscillation frequency (Fig. 5.4) and explained the physical mechanism underlying the optimal oscillation frequency (Fig. 5.6-5.10).

We studied the effect of a time dependent potential on particle transport through a microfluidic channel. We found that particle transport through the channel can be maximised by

optimizing the oscillation potential frequency. Importantly, the optimal oscillation frequency makes the alternating access channel more efficient in terms of transport compared to static channels where particles are either in free diffusion or can simultaneously bind to the ends of the channel. We found that the optimal frequency is the one that allows synchronizing alternating access with particle diffusion across the region of the channel between the two oscillating energy well positions. We also showed the effect of particle concentrations on the transport rate experimentally and explored relationship between channel occupancy and oscillation frequency at different particle concentration, details in Appendix. F. We anticipate that our findings will stimulate further investigation on mimicking the functioning of membrane protein transporters [108], on synchronized oscillations [30, 50, 109] and on the use of modulated potentials for particle control in microfluidics applications [44].

5.2 Particle transport in a potential energy landscape oscillating stochastically

5.2.1 Introduction

Channel proteins switch between open and closed states spontaneously by rearranging their structures, which is known as stochastic gating of membrane channel [110]. The phenomenon was found by Patch Clamp experiments nearly half century ago where suction was applied through a pipette to seal a small patch of membrane from cells. Later experiments showed stochastic gating in different types of ligand and voltage gated ion channels, ligand binding process to proteins [111, 112], migration of small molecules in proteins [113–115] and fast electrical coupling in cardiac muscle within gap junctions between neurons [116, 117]. Although the gating is random in a single channel, the ensemble average of recorded currents shows a smooth transient time course of opening and closing states [118, 119].

A large number of studies have been carried out to understand the effect of the stochastic gating under a common assumption that the gating reduces flux of transported solutes by a factor equivalent to the probability of a channel in its open state [118, 120]. Prof. Berezhkovskii and Prof. Bezrukov showed in literature [120], however, that gating can generate a much higher mean flux than the simple product of channel open probability and the flux through the channel when the characteristic time of gating is comparable, or smaller than, that of molecule diffusion through the channel. More recently, they demonstrated that the gating effect on flux is independent of the gating position along the channel [110].

Intrigued by this new result on the effect of stochastic gating in 1D channels, we expand our study of colloidal particles transport through microfluidic channels into the potential

energy landscape, oscillating stochastically. In the previous section, we find that there is a maximum translocation rate of particles transporting through an energy well oscillating deterministically. Here, we oscillate the potential energy landscape stochastically at frequencies from exponential distributions. Exponential distributions are chosen considering that solutes entering channels are Poisson processes and electrophysiology experiments have showed that opening and closing time of certain ion channels could be exponential [121, 122]. Interestingly, we find that the stochastically oscillated potential enhances the translocation probability in channels compared to that which oscillates deterministically. However, the harmonic peaks of particle translocation time found in the deterministically oscillated potential disappear in the stochastic oscillation experiment. Our result not only opens new way for enhancing particle transport efficiency but also provides experiment data to establish quantitative links between theory of stochastic gating and the channel transport process.

5.2.2 Experimental methods

The experiment setting is similar to the potential oscillation experiment described in Fig. 5.3 from Section 5.1.4. Briefly, a single particle is trapped within the reservoirs using HOTs, dragged to the entrance of the channel, released, and allowed to diffuse until it escapes the channel to the reservoir. Meanwhile, an optical line trap is generated by HOTs and starts to oscillate its position between the channel entrances once the particle is released. Here, the oscillation time T_Ω is chosen randomly from an exponential distribution with a mean value μ. More specifically, we first generate 300 sets of random numbers from the exponential distribution with mean parameter μ. Then 300 particles are tested in the drag-and-release experiment using individual sets of generated random numbers as oscillation periods. A mean oscillation frequency f is related to μ by $f = 1/(2\mu)$ and we repeat above experiments for seven different f. The probability density function $P(x)$ of exponential distributions with different μ is plotted in Fig. 5.11(a). The oscillation times used for $\mu = 5$ s are plotted against the corresponding $P(x)$ in Fig. 5.11(b) and show good agreement. In order to compare the effect of potential oscillating stochastically to the one oscillating deterministically, we conduct both experiments in the same microfluidic channel consecutively.

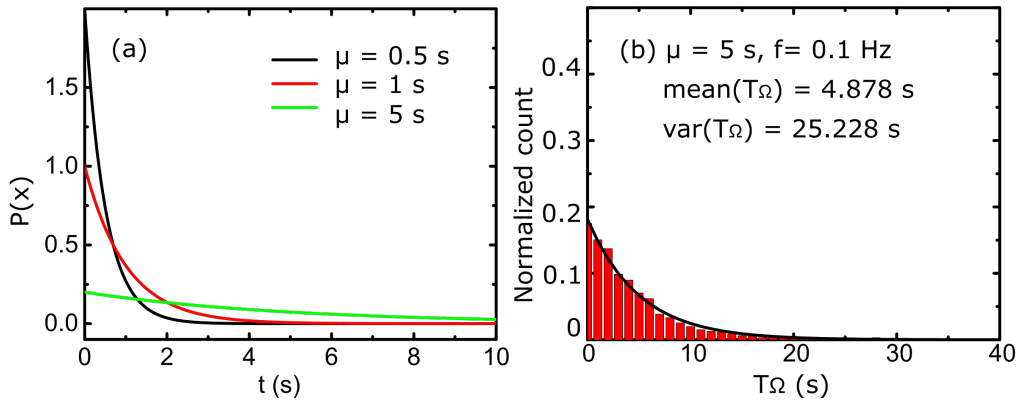

Fig. 5.11 (a) Probability density function of exponential distribution with three different mean values μ. (b) The counts of oscillation times T_Ω chosen randomly from the exponential distribution with $\mu = 5$ s show a good agreement with the probability density function $\frac{1}{\mu}e^{-\frac{T_\Omega}{\mu}}$.

5.2.3 Results and discussion

Firstly, we consider the translocation probability of particle transport across the channel with an oscillating potential. To this end, in Fig. 5.12 we plot the averaged translocation probability of particles transport through a channel with a potential oscillating stochastically (P_{sto}), along with the value measured with a potential oscillating deterministically (P_{det}). Note that for guidance, the data points are fitted by an empirical two term exponential model. P_{det} reached a peak at 0.1 Hz which is in consistent with the result in Section 5.1.4. Meanwhile P_{sto} showed the same qualitative behaviour as P_{det}, which topped at the 0.1 Hz as well. Interestingly, the measured P_{sto} value is nearly double the P_{det} in all the tested oscillation frequencies except one frequency of 0.05 Hz. So far, we have seen that a potential, oscillating stochastically enhances the transport probability of particles across channel compared to a potential, oscillating deterministically. Meanwhile both cases are more efficient compared to a static potential imposed in the channel, which is discussed in Section 5.1.4.

Next, we compare the distribution of the translocation time of particles in the channel. Resonance-like peaks are seen in the translocation time of particles through the potential, oscillating deterministically as shown in Fig. 5.13. The position of the first peak matches the inverse of the oscillation frequencies at 0.1 Hz and 0.5 Hz (Fig. 5.13(e) and (f)). However, no peak can be identified in the translocation time distribution of particles transporting through a stochastically oscillated potential with result plotted in Fig. 5.14, exhibiting a somewhat non periodic behaviour.

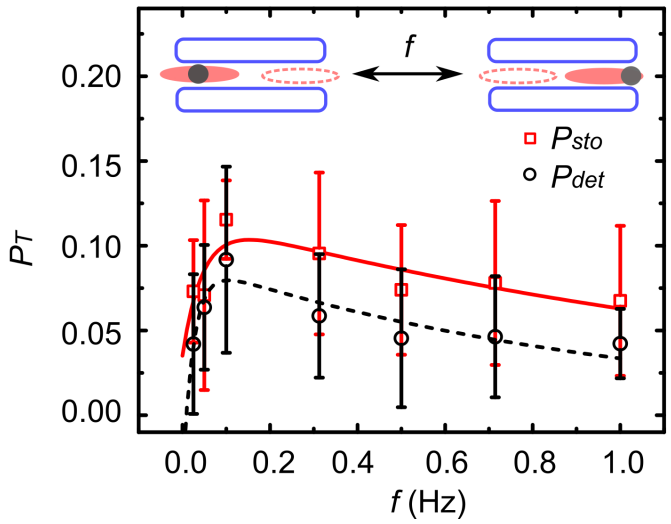

Fig. 5.12 Translocation probability P_T for particle diffusing in a channel permeated by a potential oscillating deterministically (circles) or stochastically (squares). For the potential which is oscillating randomly, each oscillation frequency is chosen from an exponential distribution with a mean value of f. The lines are two component exponential fittings to the data points. Note: the two experiments are taken in the same microfluidic channel.

Colloidal particles in microfluidics environment are undergoing Brownian motions, which are a source of intrinsic noise in our system. The optical generated potential energy landscape is oscillating temporally which switches the system between two states in the view of energy landscape. The synchronization between the thermal motion of particles and the period of energy potential oscillation has been widely studied as stochastic resonance (SR) [49]. Opposite to the general conception that noise deteriorates the system performance, a suitable amount of noise can increase it [123]. Furthermore, a fluctuating optical potential has been implemented to demonstrate that the probability distribution of the residence time of colloidal particles escaping an energy barrier is close to an exponential distribution [48]. Inspired by the SR thoery, we suspect that the stochastic oscillation frequency from the exponential distribution assists the particle transport by improving the synchronization between the potential changing and the particle diffusion. The particle translocation is a random event with a probability distribution and we hypothesize that the random oscillation frequency allows more particles to be transported in the first oscillation period which can be indicated by the disappearing of the harmonics peak in the distribution of translocation time in Fig. 5.14. However, we need to test different random oscillation frequency such as Gaussian distribution to have a better understanding of the mechanism of this enhancement in the future work.

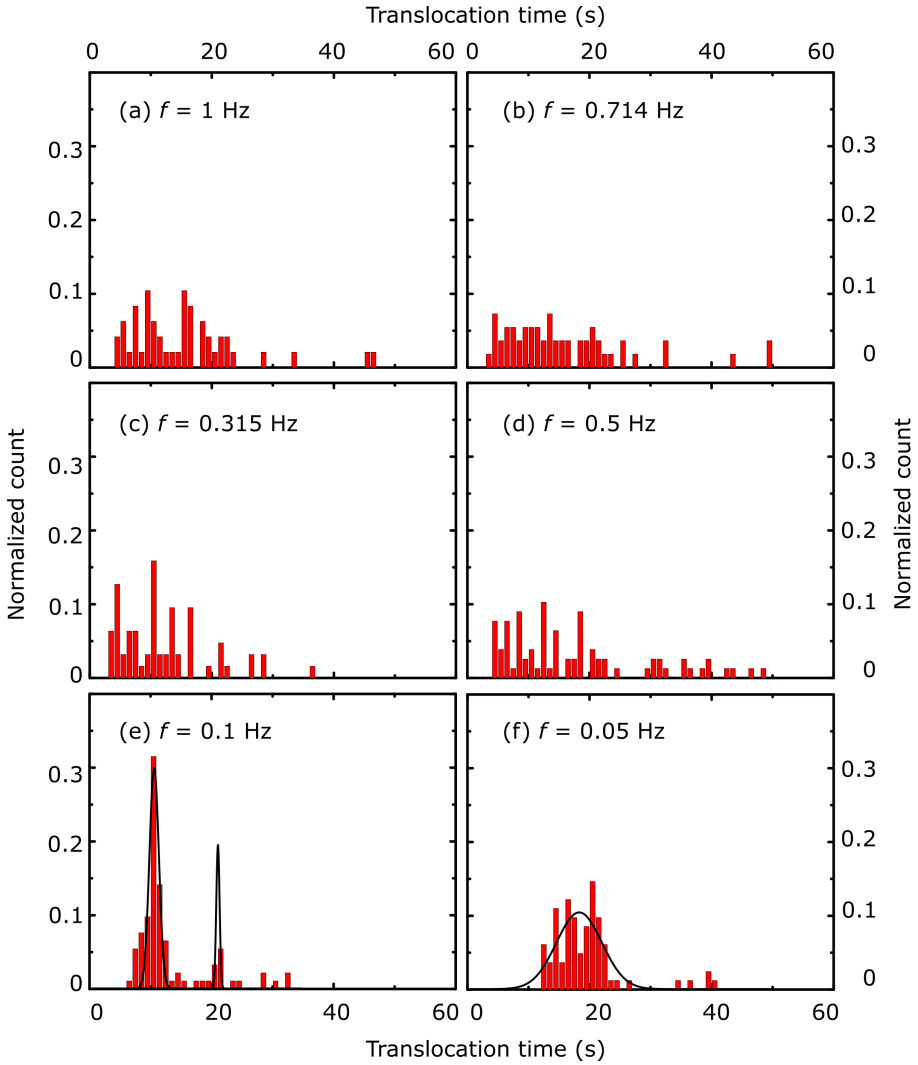

Fig. 5.13 Histogram of translocation time in a potential oscillating deterministically at constant frequencies. The experiment is conducted with particle concentration $c = 0.01$ nM in the reservoirs. The solid line is obtained by fitting a Gaussian function to the data.

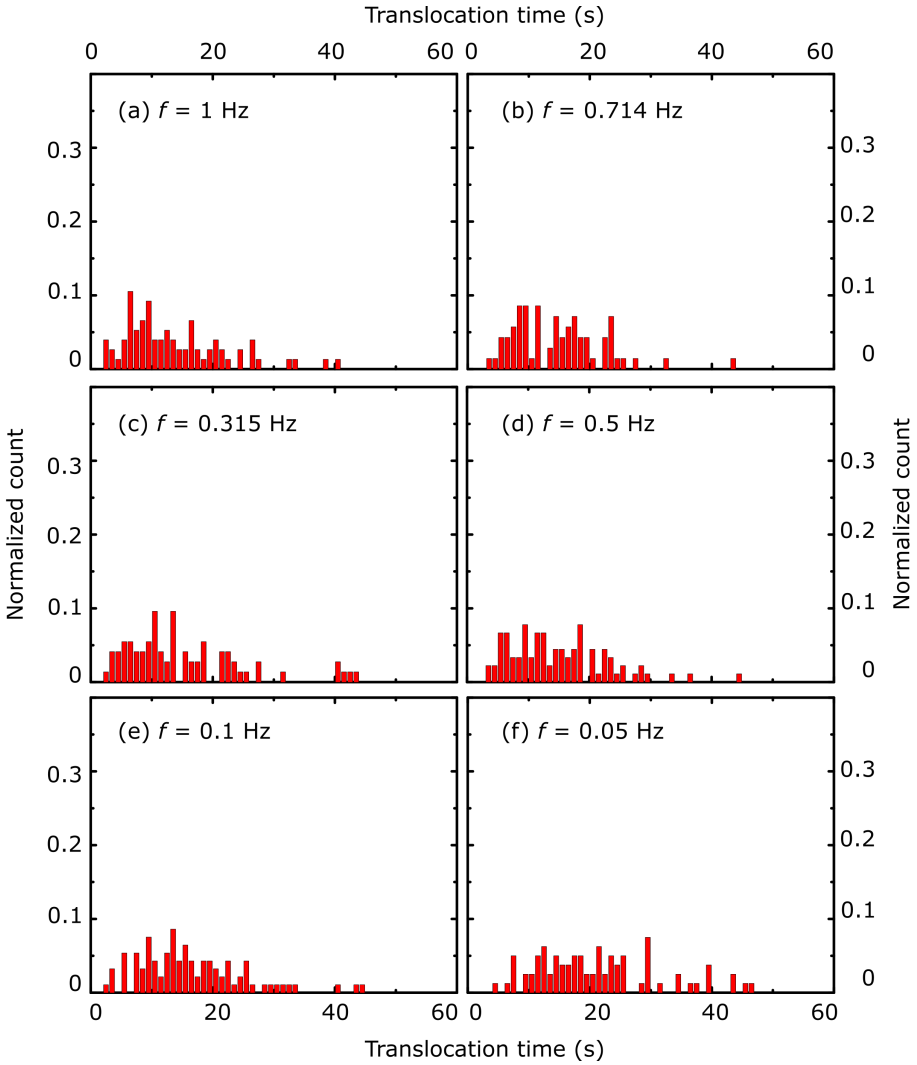

Fig. 5.14 Histogram of translocation time in a potential oscillating stochastically based on exponential distributions. The f denotes the averaged oscillation frequency. The experiment is conducted with particle concentration $c = 0.01$ nM in the reservoirs.

5.2.4 Conclusion

Following our previous work where the translocation probability of particles transport through an oscillating potential is maximised around a certain frequency, we demonstrated that a potential oscillating at random frequencies chosen from exponential distributions is able to increase the translocation probability even more. The maximum translocation probability appears when the mean frequency of the stochastic oscillation matches the free diffusion time of particle through the channel. However, the resonance-like peaks vanished in the distribution of translocation time when the potential is oscillating stochastically.

Although our experiment model system simplifies the channel transport to a 1D scenario, our finding shows the efficiency of a stochastically oscillated potential which can be related to the function of conformation changes found in channel proteins during the stochastic gating. Our experiment indicates that oscillating potentials stochastically may be an additional avenue for enhancing transport across synthetic channels or pores.

Appendix

A. Fitting attempt rate and translocation rate

The experimental data for the attempt rate, translocation rate and translocation probability plotted in Fig. 5.5 and 5.20 is fitted by a two-term exponential model $f(x) = a * \exp(b * x) + c * \exp(d * x)$ via the nonlinear least-squares method, where a, b, c and d are the fitting parameters. The values for these parameters estimated by the fitting are reported in Tables 5.1-5.3.

Table 5.1 Fitting of attempt rate data

c (nM)	a	b	c	d
0.07	9853436.5	-2.1	-9853424.6	-2.1
0.22	83037687.0	-0.3	-83037511.7	-0.3
1.01	3013.6	0.65	10014.3	-73.7

Table 5.2 Fitting of translocation rate data

c (nM)	a	b	c	d
0.07	26.7	-1.9	-19.0	-12.7
0.22	77.4	-2.0	-86.7	-14.5
1.01	137.6	-1.0	-187.9	-17.0

Table 5.3 Fitting of translocation probability data

c (nM)	a	b	c	d
0.07	0.2	-3.9	-0.1	-45.0
0.22	0.2	-3.9	-0.2	-23.9
1.01	0.05	-1.8	-0.1	-20.7

B. Channel jamming with static double well potential

We compared particle transport in a static double well potential with the same extension as the oscillating potential. When we used a static double well potential with the same depth used for the oscillating potential, we observed that the channel was quickly jammed with particles, a typical image shown in Fig. 5.15. Therefore, for the experiments reported in Fig. 5.5 and Fig. 5.20, we reduced the depth of the static double well potential to 42 % of the oscillation potential.

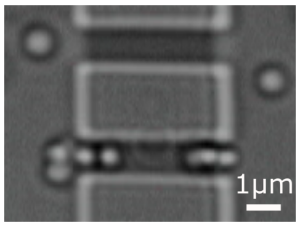

Fig. 5.15 Bright field image of 510 nm polystyrene particles jamming the entrances of the channel permeated with static energy wells as deep as the potential wells used for the oscillation.

C. Transport of particles through a channel in free diffusion

Particles transport through a microfluidic channel for different particle concentrations in the reservoirs and without any optical potential coupled in the channel. Both the attempt rate and translocation rate increase with the particle concentration as expected (Fig. 5.16).

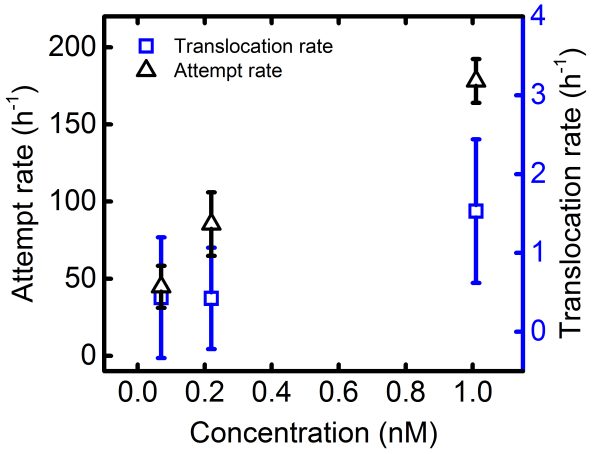

Fig. 5.16 Dependence of attempt (triangles) and translocation rate (squares) with respect to the particle concentration, for particles in free diffusion through the microfluidic channel described in Fig. 5.5. Data and error bars are the mean and standard deviation of the values measured in five different one hour long experiments.

D. Effect of boundary position on the translocation time distribution

In the translocation time distribution obtained via Brownian dynamics simulations (Fig. 5.7), a board peak is found on the left of the first resonance-like peak for frequencies f= 0.025, 0.5 and 0.1 Hz. These peaks indicate that some particles translocate through the channel before the potential oscillation finishes for the first time, which is $2T_\Omega$. This can be explained by the exemplary translocation illustrated in Fig. 5.9. Once a particle diffuses through region II and III [Fig. 5.9(b)], it stays near the minimum of the right-hand potential well [solid line in Fig. 5.9(c)]. The longer the potential is on the right-hand side, the higher the chance particle will touch the right end of the channel. Due to the definition of the channel end as an absorbing boundary, the particle already fulfils a translocation event. The explanations are supported by moving the absorbing boundary position relative to the channel end by a distance Δd. Here, $\Delta d < 0$ represents the absorbing boundary is inside the channel. $\Delta d = 0$ means the absorbing boundary is on the channel end. $\Delta d > 0$ has the absorbing boundary outside the channel end. The board peaks discussed above vanish with an increased value of Δd from negative to zero then to a positive value (Fig. 5.17). The vanishing of the board peaks comes along with the surging of the first harmonics peak at the inverse of the oscillation frequency.

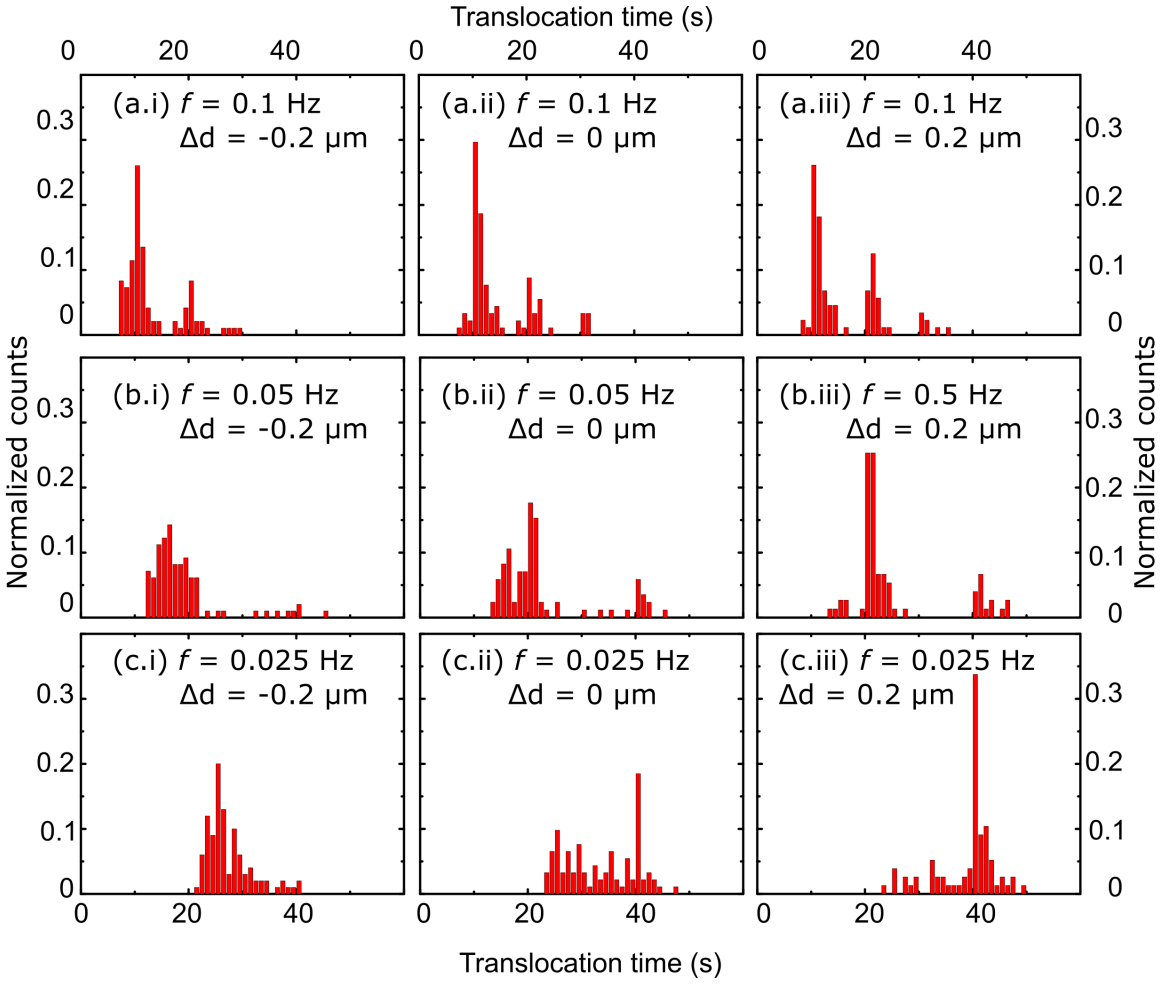

Fig. 5.17 Effect of absorbing boundary position on the translocation time distribution. The normalised distribution of translocation times is measured depending on the distance Δd between the boundary position and the channel end at different oscillation frequency f. (a-c.i) $\Delta d = -0.2$ μm means that the boundaries are inside the channel ends. (a-c.ii) $\Delta d = 0$ μm means that channel ends are set as the absorbing boundaries. (a-c.iii) $\Delta d = 0.2$ μm means that the boundaries are outside the channel ends.

E. Numerical solution of the Fokker-Planck equation

In order to obtain a more quantitative understanding of the optimal oscillation frequency, we solve the Fokker-Planck (FP) equation (Eq. 2.8) numerically using *Mathematica*. As described in Section 2.2, the solution of the FP equation provides the probability density distribution $p(x,t)$ of particles diffusing in an energy potential. Particle current J at position x can be calculated from $\partial p(x,t)/\partial t$, which describes the number of particles passing through x at time t.

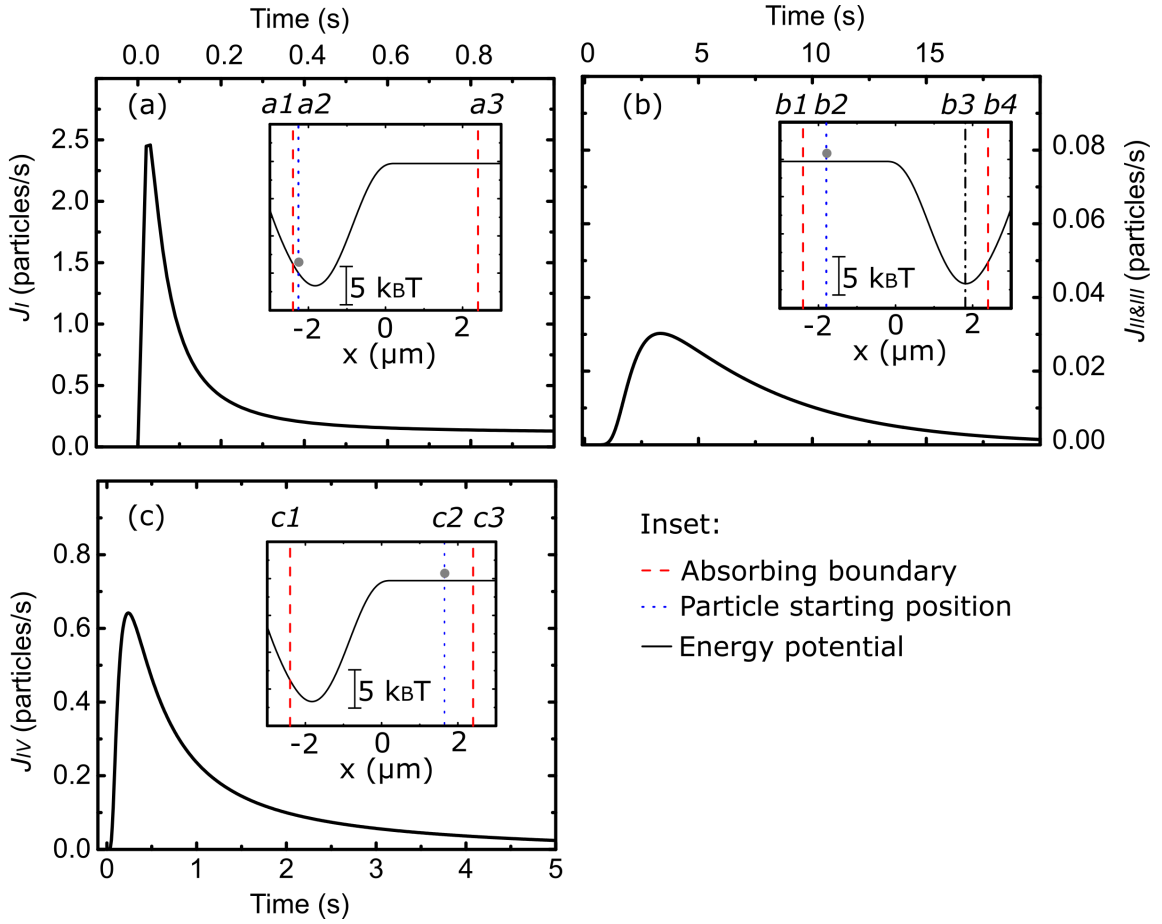

Fig. 5.18 Particle currents calculated by solving the Fokker-Planck equation numerically with an experimentally fitted energy potential (solid lines in the insets). (a) Stage I: a particle is released at *a2* with two absorbing boundaries at *a1* and *a3*. Particle current J_I is calculated at *a1*. (b) Stage II&III: A particle is released at the position of the left-hand potential minimum *b2*. The particle flux $J_{II\&III}$ is calculated at *b3* (dash-dotted line). *b1* and *b4* are the absorbing boundaries. (c) Stage III: A particle is released at the right-hand potential minimum *c2*. Particle current J_{IV} is calculated at *c3*. *c1* and *c3* are the absorbing boundaries. The absorb boundary is represented by a dashed line. The particle starting position is represented by a dotted line.

The experimentally measured energy potential [Fig. 5.2(d)] is first fitted by a sixth-order polynomial curve, shown by solid lines in the insets of Fig. 5.18. The fitted energy potential $U(x)$ and experimentally measured diffusion coefficient D are applied in the numerical solution of the FP equations. The equations are solved in successive stages. Stage I: A particle is released next to the left entrance of the channel at $a2$ [dotted line in the inset of Fig. 5.18(a)]. The left ($a1$) and right ($a3$) entrances of the channel are set as absorbing boundaries [dash lines in the inset of Fig. 5.18(a)]. Particle current is obtained from the solution of the FP equation. Particle current at $a1$, denoted as J_I peaks at 0.03 s then decreases with time, shown by a solid line in Fig. 5.18(a). By integrating J_I by time, we get the percentage of particles absorbed by $a1$ during the period when the left-hand potential is on. The percentage of particles left in the channel is then calculated by $n_I = 1 - \int_0^{200} J_I dt$, with the integration limits denoting the time interval of the numerical solution with units of second. n_I is plotted in Fig. 5.19(a) as a solid line. Stage II: a particle initiates at the minimum position of the left-hand potential $b2$ and diffuses in the right-hand potential, as sketched in the inset of Fig. 5.18(b). The percentage of particles that arrive at $b3$ at time t is given by integrating $J_{II\&III}$ [solid line in Fig. 5.18(b)], denoted as $n_{II\&III}$ [dotted line in the inset of Fig. 5.19(a)]. Stage III: a particle is started at the right-hand potential minimum $c2$ [dotted line in Fig. 5.19(c)]. The percentage of particles absorbed by the right channel entrance n_{IV}

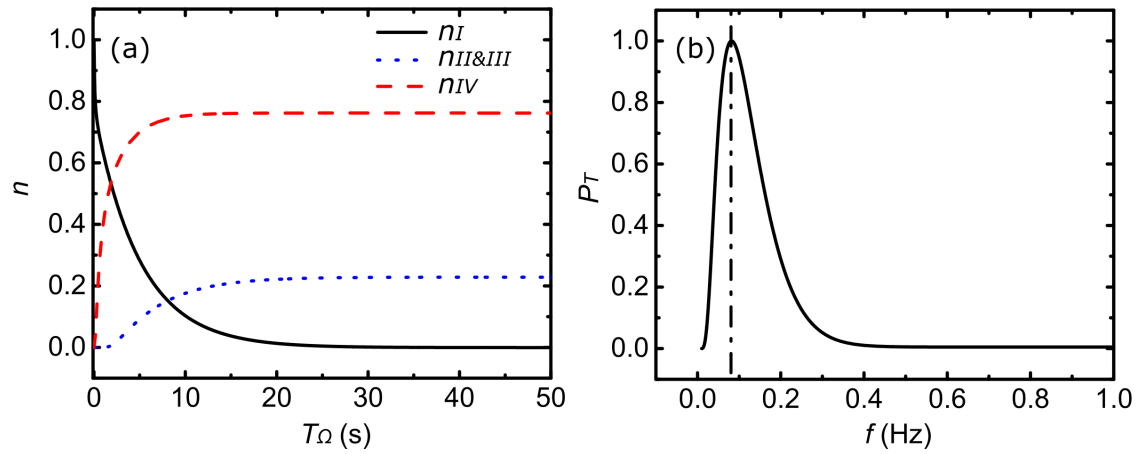

Fig. 5.19 Translocation probability of particles diffusing in an oscillating potential. (a) n is the percentage of particles absorbed by an absorbing boundary or arriving at a certain position by integrating the particle currents J (plotted in Fig 5.18). (b) The normalised translocation probability P_T is the product of $n_I \cdot n_{II\&III} \cdot n_{IV}$.

[dashed line in Fig. 5.19(a)] is calculated by integrating J_{IV} [solid line in Fig. 5.18(c)]. As

stage I to III happens subsequently, the translocation probability P_T is estimated by

$$P_T = n_I \cdot n_{II\&III} \cdot n_{IV} \tag{5.3}$$

resulting in a maximum P_T at $f = 0.08$ Hz, plotted in Fig. 5.19(b). This frequency matches the optimal oscillation frequencies found in our experiment (0.1 Hz) and simulations (0.0125 Hz) in the drag-and-release model (Section 5.1.4).

F. Dependence of channel occupancy on the frequency of the oscillating potential

In order to gain more insight on the presence of an optimal oscillation frequency, we measure the channel occupation probability $p(n)$, which is the probability to simultaneously find n particles in the channel. The result is plotted in Fig. 5.20.

At high particle concentrations, we measure that the probability to find one particle in the channel $p(1)$ is at a maximum for frequencies close to the optimal oscillation frequency (triangles and squares for $c = 0.22$ and 1.07 nM, respectively, in Fig. 5.20(b)). Notably, the channel is predominantly empty at low frequencies (e.g. p(0)=0.58 for $c = 0.22$ nM and $f = 0.05$ Hz, triangles in Fig. 5.20(a)) whereas at high frequency and concentration the channel is crowded [Fig. 5.20(c,d)], e.g. $p(\geq 3) = 0.94$ for $c = 1.07$ nM and $f = 1$ Hz. Therefore, the optimal oscillation frequency is the one that allows for populating the channel without overcrowding it [52].

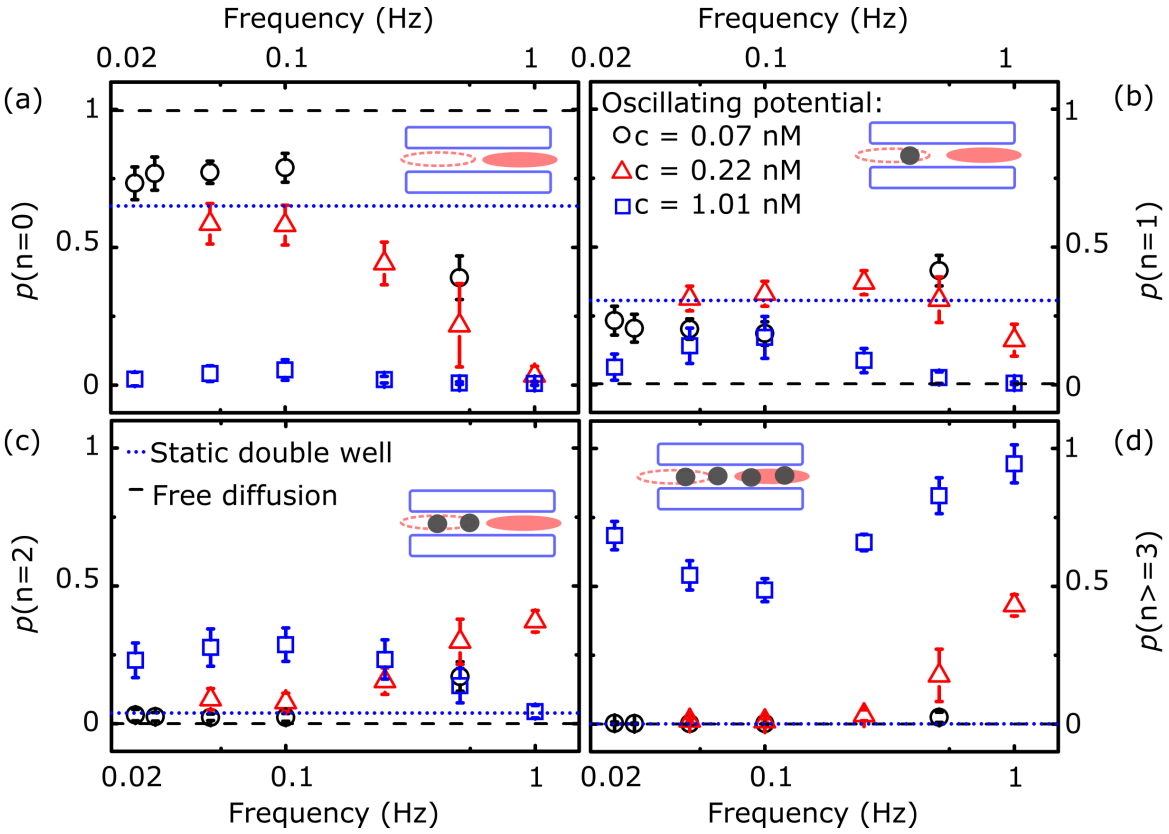

Fig. 5.20 Dependence of the experimentally measured probability to find (a) no particle $p(n=0)$, (b) one particle $p(n=1)$, (c) two particles $p(n=2)$ or (d) more than two colloidal particles $p(n\geq 3)$ on the oscillation potential frequency and particle concentration. Circles, triangles and squares represent data for a particle concentration of 0.07 nM, 0.22 nM and 1.01 nM, respectively. Dotted and dashed lines represent data for a static potential and particle free diffusion in the channel, respectively.

Chapter 6

Summary and outlook

In this thesis, we built up an experimental synthetic membrane system to study the transport of particles across a channel permeated by modulated energy landscapes. The synthetic membrane system is made up of microfluidics channels connecting two reservoirs containing colloidal particles undergoing Brownian motion. Holographic Optical Tweezers (HOTs) were used to modulate the energy landscape in the channel that also allows generating time-dependent potentials and potentials with high energy barriers.

6.1 Characterisation of a potential energy landscape

In order to have a full characterisation of the optically induced energy potential, we first calibrated the effective energy landscape obtained from the intensity distribution of the optical traps with the energy landscape reconstructed from the Probability Density Function (PDF) of particle positions. This calibration was validated by driving a particle through the optically induced potential. The calibration method provides us a way to measure energy landscapes with high barriers which are inaccessible to trajectory-based methods, such as PDF. However, those methods cannot be used to rebuild the energy landscape in systems out of equilibrium. Therefore, we developed a new method which uses the Local Transition Probability (LTP) of particles to reconstruct the energy landscape. The LTP approach improves the robustness of the result compared to the splitting probability (SP) method and it provides a better way to estimate the energy landscape under non-equilibrium conditions. Furthermore, by combining the LTP and the above described calibration method, we were able to reconstruct the energy landscape in a complex environment.

Having a full map of the underlying energy landscape is a useful tool to explore the origins of complex natural processes, but collecting large enough data ensembles from those processes remains a tough challenge. For instance, reaction profiles have long been used to

qualitatively analyse chemical reactions in chemical kinetics; resolving energy landscapes has been a key approach to study protein folding in biology; the translocation through membrane proteins has been rationalized by free energy landscapes which leads to the effect of size and binding on transport [124]. However, all those processes are intrinsically stochastic and the data collection involves lengthy experiments and a lot of effort for unstable reactions or rare events. For example, the probability of a thermal activation across a potential with an energy well scales exponentially with the depth of the well, which could make the experiment unimplementable in practice. Here, the LTP method proposed by us utilizes the Bayesian rules which trains a prior model with data. As a result, our method improves the accuracy of the rebuilt potential energy landscape compared to PDF or SP. We are also able to estimate the uncertainty of the rebuilt potential which is inaccessible to other methods.

Meanwhile, most natural phenomena are far away from equilibrium so their energy landscapes cannot be assessed by the PDF method. The SP method is applicable at non-equilibrium situation but requires a large data ensemble. Based on the original idea of SP method, the LTP method works in both equilibrium and out of equilibrium environments. Remarkably, our approach requires no additional infrastructure for data collection. Getting more accurate result by analysing the same data set is extremely attractive for studies related to energy potential. For example, the DNA trajectory data used to study giant acceleration in entropic barriers [96] can be readily analysed by our method to map out the underlying free energy landscape, which will provide a comparable way to probe the entropy. It is worth mentioning that Bayesian analysis is an important deep learning algorithm in computer science [125]. Our current algorithm is based on a preliminary idea of using Bayesian rules to better fit the model, but the fruitful deep learning research will allow us to improve this initial approach further.

6.2 Function of a fluctuating potential in channel transport

In the second part of our work, particle transport across channels was studied under an oscillating potential. By oscillating the position of the energy well deterministically, an optimal frequency was found which maximises the the translocation rate of particles across the channel. At the optimal oscillation frequency, the translocation rate was found to be enhanced one hundred times compared to a channel with no external potential. The optimal frequency was verified in Brownian dynamics simulations. The optimised transport was further explained by calculating the mean exit time from the channel. We found that the

optimal frequency is the one that matches the potential oscillation with the particle diffusion time across the region between the positions of two oscillating energy wells. Our experiment system provides a synthetic platform where the parameters of alternating access model can be tested individually. Our result sheds light on the possibility of biomimetics by indicating that an oscillating potential may be an additional avenue for enhancing transport across synthetic channels or pores. The result also provides important insights for the function of stochastic resonance (SR) in transport processes. Previous colloidal experiments have explored SR in experiments where a single particle jumping across an energy barrier[49, 50]. On top of that, it is possible to exam the SR theory with multiple particles in a channel with precise control of the number in our experimental system, which is closer to the actual biological pores, where several substrates can be in the pore simultaneously.

One step further, we tested particle transport through channels with a potential energy landscape oscillating stochastically. We find that the translocation probability of particles across the channel is enhanced even more compared to the case where the potential energy landscape is oscillating deterministically. Besides the increased transport rate we observed in a stochastically oscillated energy landscape; the selectivity of substrates which is omnipresent in membrane proteins could be also related to fluctuations of the pore structure. Metabolite channels, which accommodate metabolite molecules, for instance, have a wider radius compared to ion channels but are found permanently closed under certain conditions which allows the membrane to sustain its barrier function. In a recent published work [126], stochastic gating is shown to favour large metabolites compared to small solutes during channel-facilitated transport based on diffusion models. The fast gating reduces the flux of small mobile solutes more strongly than the less mobile ones. Therefore, one very interesting question to ask is can we find selectivity of different size particles in the potential oscillation experiment. The experiment setting can be achieved by having two sizes of particles mixed in the reservoirs and with one specie coated by dye. Then the diffusion of the particles can be recorded and distinguished by switching between white illumination and the corresponding fluorescence wavelength. We conjecture that the concentration and the ratio of the different particles will also play a role in the transport. Besides, we have tested energy landscape oscillating its position stochastically from exponential distributions based on the knowledge that the solute entering channels is a Poisson process. Current theoretical models which do not take the actual oscillation process into account [110, 120, 126]. Therefore other stochastic distributions of oscillation times should be tested and compared, which shows the strength of a synthetic membrane experiment system that can study different oscillation modes. The result will be relevant not only to the ion channel transport, but also to solvent filters with widespread applications.

The stochastic gating is also reminiscent of the concept of Maxwell's Demon which improves the flux only in one direction by blocking the entrance of substrate from one chamber to another. Maxwell's Demon has been demonstrated in various system showing information converted to energy, such as rotational Brownian motion between glasses [127] and coupled single electron circuits [128]. It will be useful to explore the transport in a particle-position dependent energy landscape. As found in membrane proteins, the conformational change can be triggered by binding to one specific solute. In this case, the energy landscape is not only time-dependent, but also position-dependent. It will be meaningful to demonstrate that this mechanism plays a role in the alternating access model. The idea could be tested in our colloids-channel experiment by tracking the particle's position in real time and putting feedback control to the energy landscape, which can be implemented by programming the image processing and optical trap generating algorithm.

6.3 Mimicking the transport across membranes

It is worth noting here that our synthetic membrane system is a highly simplified model compared to cell membranes. In order to mimic the membrane transport in living cells, we should first seek a full control of the particle concentration in the reservoirs connected by the channels. Currently we manage to set the particle concentration equivalent in both reservoirs which provides an equilibrium environment. However, the concentration difference between the extracellular side and the cytosol is a main factor in solute transport across the membrane. While the concentration gradient of solutes powers up the facilitated diffusion, the active transport process moves a substance across a membrane against its concentration gradient. The effect of concentration difference on particle transport could be explored at least in terms of entering probability, jamming and transport efficiency. The result will be more comparable to the cellular environment. To achieve this, we need to separate the two reservoirs completely by modifying the initial design of the microfluidics chip. Then different particle solvents could be injected into the reservoirs, which might induce pressure differences but can be controlled by adjusting the volume of the injected solvent. Secondly, it is possible to explore asymmetric systems with charged particles in one of the two reservoirs. Thus our system will be mimicking electrochemical gradients and even exhibit effects like charge polarisation under applied external driving forces. To do this, we could put electrodes into the two reservoirs then apply voltage across the channel. Thirdly our synthetic platform can be scaled down to nanoscale where the characteristic diffusion time is closer to the one observed in protein transporters. This can be achieved by using capillary nanopore on microfluidics or DNA origami formed pore structure, as a promising candidate with flexibility to be modified

chemically. Beside the above mentioned factors, there are other parameters in the membrane domain which play important roles in the transport process such as the cytoskeleton inside the cell and the energy consumed while conformational changes, which is also worth detailed study. Overall, the complex and important transport process happening across membranes will keep providing incentives to continue with this research.

References

[1] Philip H Jones, Onofrio M Maragò, and Giovanni Volpe. *Optical tweezers: Principles and applications*. Cambridge University Press, 2015.

[2] Philip G Saffman and Max Delbrück. Brownian motion in biological membranes. *Proceedings of the National Academy of Sciences*, 72(8):3111–3113, 1975.

[3] Greta M Lee, Akira Ishihara, and Ken A. Jacobson. Direct observation of brownian motion of lipids in a membrane. *Proceedings of the National Academy of Sciences*, 88(14):6274–8, 1991.

[4] Caterina Strambio-De-Castillia, Mario Niepel, and Michael P Rout. The nuclear pore complex: bridging nuclear transport and gene regulation. *Nature reviews. Molecular cell biology*, 11(7):490–501, 2010.

[5] David Holcman and Zeev Schuss. *Stochastic narrow escape in molecular and cellular biology : analysis and applications*. Springer, 2015.

[6] Zeev Schuss. *Theory and applications of stochastic processes : an analytical approach*. Springer, 2010.

[7] Hida Takeyuki. *Brownian Motion*. Springer, 1980.

[8] Bruce Alberts, Dennis Bray, Julian Lewis, Martin Raff, Keith Roberts, James D Watson, and AV Grimstone. *Molecular Biology of the Cell (3rd edn)*. Garland Science, 1995.

[9] Oleg Jardetzky. Simple allosteric model for membrane pumps. *Nature*, 211(5052):969–970, 1966.

[10] Dirk J. Slotboom. Structural and mechanistic insights into prokaryotic energy-coupling factor transporters. *Nature Reviews Microbiology*, 12(2):79–87, 2014.

[11] Douglas C. Rees, Eric Johnson, and Oded Lewinson. ABC transporters: the power to change. *Nature Reviews Molecular Cell Biology*, 10(3):218–227, 2009.

[12] Kiyohiko Sugano, Manfred Kansy, Per Artursson, Alex Avdeef, Stefanie Bendels, Li Di, Gerhard F Ecker, Bernard Faller, Holger Fischer, Grégori Gerebtzoff, Hans Lennernaes, and Frank Senner. Coexistence of passive and carrier-mediated processes in drug transport. *Nature reviews. Drug discovery*, 9(8):597–614, 2010.

[13] Jeff Abramson, Irina Smirnova, Vladimir Kasho, Gillian Verner, H Ronald Kaback, and So Iwata. Structure and mechanism of the lactose permease of Escherichia coli. *Science*, 301(5633):610–5, 2003.

[14] Li-Qing Chen, Lily S Cheung, Liang Feng, Widmar Tanner, and Wolf B Frommer. Transport of Sugars. *Annual Review of Biochemistry*, 84(1):865–894, 2015.

[15] Dong Deng, Chao Xu, Pengcheng Sun, Jianping Wu, Chuangye Yan, Mingxu Hu, and Nieng Yan. Crystal structure of the human glucose transporter GLUT1. *Nature*, 510(7503):121–125, 2014.

[16] Ekaterina M Nestorovich, Christophe Danelon, Mathias Winterhalter, and Sergey M Bezrukov. Designed to penetrate: time-resolved interaction of single antibiotic molecules with bacterial pores. *Proceedings of the National Academy of Sciences*, 99(15):9789–94, 2002.

[17] Yongfang Zhao, Daniel S Terry, Lei Shi, Matthias Quick, Harel Weinstein, Scott C Blanchard, and Jonathan a Javitch. Substrate-modulated gating dynamics in a Na+-coupled neurotransmitter transporter homologue. *Nature*, 474(7349):109–13, 2011.

[18] Raimund Dutzler, Y-F Wang, PJ Rizkallah, JP Rosenbusch, and T Schirmer. Crystal structures of various maltooligosaccharides bound to maltoporin reveal a specific sugar translocation pathway. *Structure*, 4(2):127–134, 1996.

[19] C. Hilty and Mathias Winterhalter. Facilitated Substrate Transport through Membrane Proteins. *Physical Review Letters*, 86(24):5624–5627, 2001.

[20] Jonathan R Burns, Kerstin Göpfrich, James W Wood, Vivek V Thacker, Eugen Stulz, Ulrich F Keyser, and Stefan Howorka. Lipid-Bilayer-Spanning DNA Nanopores with a Bifunctional Porphyrin Anchor. *Angewandte Chemie*, pages 12069–12072, 2013.

[21] Jehangir Cama, Harsha Bajaj, Stefano Pagliara, Theresa Maier, Yvonne Braun, Mathias Winterhalter, and Ulrich F. Keyser. Quantification of Fluoroquinolone Uptake through the Outer Membrane Channel OmpF of Escherichia coli. *Journal of the American Chemical Society*, 137(43):13836–13843, 2015.

[22] Morten Ø Jensen, Sanghyun Park, Emad Tajkhorshid, and Klaus Schulten. Energetics of glycerol conduction through aquaglyceroporin GlpF. *Proceedings of the National Academy of Sciences*, 99(10):6731–6, 2002.

[23] Simon Gravelle, Laurent Joly, François Detcheverry, Christophe Ybert, Cécile Cottin-Bizonne, and Lydéric Bocquet. Optimizing water permeability through the hourglass shape of aquaporins. *Proceedings of the National Academy of Sciences*, 110(41):16367–72, 2013.

[24] Alexander M Berezhkovskii and Sergey M Bezrukov. Optimizing Transport of Metabolites through Large Channels: Molecular Sieves with and without Binding. *Biophysical Journal*, 88(3):L17–L19, 2005.

[25] Anatoly Kolomeisky. Channel-Facilitated Molecular Transport across Membranes: Attraction, Repulsion, and Asymmetry. *Physical Review Letters*, 98(4):048105, 2007.

[26] Anton Zilman. Effects of Multiple Occupancy and Interparticle Interactions on Selective Transport through Narrow Channels: Theory versus Experiment. *Biophysical Journal*, 96(4):1235–1248, 2009.

[27] Pietro Tierno. Depinning and collective dynamics of magnetically driven colloidal monolayers. *Physical Review Letters*, 109(19):4–8, 2012.

[28] Simon Verleger, Andrej Grimm, Christian Kreuter, Huei Ming Tan, Jeroen a. van Kan, Artur Erbe, Elke Scheer, and Johan R. C. van der Maarel. A single-channel microparticle sieve based on Brownian ratchets. *Lab on a chip*, 12(7):1238–41, 2012.

[29] Xiang Yang, Chang Liu, Yunyun Li, Fabio Marchesoni, Peter Hänggi, and H P Zhang. Hydrodynamic and entropic effects on colloidal diffusion in corrugated channels. *Proceedings of the National Academy of Sciences*, 114(36):9564–9569, 2017.

[30] Michael P N Juniper, Arthur V Straube, Rut Besseling, Dirk G A L Aarts, and Roel P A Dullens. Microscopic dynamics of synchronization in driven colloids. *Nature communications*, 6:7187, 2015.

[31] Binhua Lin, Mati Meron, Bianxiao Cui, Stuart Rice, and Haim Diamant. From Random Walk to Single-File Diffusion. *Physical Review Letters*, 94(21):216001, 2005.

[32] Guillem Portella, Tanja Polupanow, Florian Zocher, Danila a Boytsov, Peter Pohl, Ulf Diederichsen, and Bert L de Groot. Design of peptide-membrane interactions to modulate single-file water transport through modified gramicidin channels. *Biophysical journal*, 103(8):1698–705, 2012.

[33] Karsten Hahn, Jörg Kärger, and Volker Kukla. Single-File Diffusion Observation. *Physical Review Letters*, 76(15):2762–2765, 1996.

[34] Volker Kukla, Jan Kornatowski, Dirk Demuth, Irina Girnus, Harry Pfeifer, Lovat V C Rees, Stefan Schunk, Klaus K Unger, and Jorg Karger. NMR Studies of Single-File Diffusion in Unidimensional Channel Zeolites. *Science*, 272(5262):702–704, 1996.

[35] Alexander M. Berezhkovskii, Leonardo Dagdug, and Sergey M. Bezrukov. Biased diffusion in three-dimensional comb-like structures. *Journal of Chemical Physics*, 142(13), 2015.

[36] Alexander M. Berezhkovskii, Mark A. Pustovoit, and Sergey M. Bezrukov. Channel-facilitated membrane transport: Transit probability and interaction with the channel. *Journal of Chemical Physics*, 116(22):9952–9956, 2002.

[37] Alexander M. Berezhkovskii, Leonardo Dagdug, and Sergey M. Bezrukov. Mean Direct-Transit and Looping Times as Functions of the Potential Shape. *The Journal of Physical Chemistry B*, 121(21):5455–5460, 2017.

[38] Sang-Hyuk Lee and David G. Grier. Giant Colloidal Diffusivity on Corrugated Optical Vortices. *Physical Review Letters*, 96(19):190601, 2006.

[39] Michael P N Juniper, Arthur V Straube, Dirk G A L Aarts, and Roel P A Dullens. Colloidal particles driven across periodic optical-potential-energy landscapes. *Physical Review E*, 93(1):012608, 2016.

[40] Luc P Faucheux, L. S. Bourdieu, P. D. Kaplan, and A. J. Libchaber. Optical Thermal Ratchet. *Physical Review Letters*, 74(9):1504–1507, 1995.

[41] Sang-Hyuk Lee, Kosta Ladavac, Marco Polin, and David G Grier. Observation of Flux Reversal in a Symmetric Optical Thermal Ratchet. *Physical Review Letters*, 94(11):110601, 2005.

[42] Stefan. Bleil, Peter. Reimann, and Clemens. Bechinger. Directing Brownian motion by oscillating barriers. *Physical Review E*, 75:1–5, 2007.

[43] Laurence Talini, S Jeanjean, and Pascal Silberzan. Sorting of Brownian particles by the pulsed application of an asymmetric potential. *Physical Review E*, 56(2):2025–2034, 1997.

[44] Michael P. MacDonald, Gabriel C. Spalding, and Kishan. Dholakia. Microfluidic sorting in an optical lattice. *Nature*, 426(6965):421–424, 2003.

[45] Alexandr Jonáš and Pavel Zemánek. Light at work: The use of optical forces for particle manipulation, sorting, and analysis. *Electrophoresis*, 29(24):4813–4851, 2008.

[46] Ke Xiao and David G Grier. Sorting colloidal particles into multiple channels with optical forces: Prismatic optical fractionation. *Physical Review E*, 82(5):051407, 2010.

[47] Kosta Ladavac, Kristen Kasza, and David G Grier. Sorting mesoscopic objects with periodic potential landscapes: Optical fractionation. *Physical Review E*, 70(1):010901, 2004.

[48] Adam Simon and Albert Libchaber. Escape and synchronization of a Brownian particle. *Physical Review Letters*, 68(23):3375–3378, 1992.

[49] Dusan Babič, Caremen Schmitt, I Poberaj, and Clemens Bechinger. Stochastic resonance in colloidal systems. *Europhysics Letters*, 67(2):158–164, 2004.

[50] Carmen Schmitt, Bartlomiej Dybiec, Peter Hänggi, and Clemens Bechinger. Stochastic resonance vs. resonant activation. *Europhysics Letters*, 74(6):937–943, 2006.

[51] Stefano Pagliara, Christian Schwall, and Ulrich F Keyser. Optimizing diffusive transport through a synthetic membrane channel. *Advanced materials*, 25(6):844–9, 2013.

[52] Stefano Pagliara, Simon L Dettmer, and Ulrich F Keyser. Channel-Facilitated Diffusion Boosted by Particle Binding at the Channel Entrance. *Physical Review Letters*, 113(4):048102, 2014.

[53] Zénó Farkas and Tamás Fülöp. One-dimensional drift-diffusion between two absorbing boundaries: application to granular segregation. *Journal of Physics A: Mathematical and General*, 34(15):3191–3198, 2001.

[54] Sidney Redner. *A guide to first-passage processes*. Cambridge University Press, 2001.

[55] Fanlong Meng, Ming Li, Xin Zhou, and Zhongcan Ouyang. A theoretical study on entropy-driven polymer translocation through a finite-sized nanochannel. *Chemical Physics Letters*, 565:116–121, 2013.

[56] Arthur Ashkin. Acceleration and Trapping of Particles by Radiation Pressure. *Physical Review Letters*, 24(4):156–159, 1970.

[57] Lowell L McCann, Lowell L McCann, Mark Dykman, Mark Dykman, Brage Golding, and Brage Golding. Thermally activated transitions in a bistable three dimensional optical trap. *Nature*, 402(December):785, 1999.

[58] Michael T Woodside, Peter C Anthony, William M Behnke-Parks, Kevan Larizadeh, Daniel Herschlag, and Steven M Block. Direct Measurement of the Full, Sequence-Dependent Folding Landscape of a Nucleic Acid. *Science*, 314(5801):1001–1004, 2006.

[59] John D. Chodera and Vijay S. Pande. Splitting probabilities as a test of reaction coordinate choice in single-molecule experiments. *Physical Review Letters*, 107(9):1–5, 2011.

[60] Ajay P. Manuel, John Lambert, and Michael T. Woodside. Reconstructing folding energy landscapes from splitting probability analysis of single-molecule trajectories. *Proceedings of the National Academy of Sciences*, (14):201419490, 2015.

[61] Michael P N Juniper, Rut Besseling, Dirk G a L Aarts, and Roel P a Dullens. Acousto-optically generated potential energy landscapes: potential mapping using colloids under flow. *Optics express*, 20(27):28707–16, 2012.

[62] Michael P. N. Juniper. *Dynamics of driven colloidal systems in one-dimensional potential energy landscapes*. PhD thesis, University of Oxford, 2014.

[63] David G. Grier. A revolution in optical manipulation. *Nature*, 424(6950):810–816, 2003.

[64] Miles Padgett and Roberto Di Leonardo. Holographic optical tweezers and their relevance to lab on chip devices. *Lab on a Chip*, 11(7):1196, 2011.

[65] Alice L Thorneywork, Roberto E Rozas, Roel P. A. Dullens, and Jürgen Horbach. Effect of Hydrodynamic Interactions on Self-Diffusion of Quasi-Two-Dimensional Colloidal Hard Spheres. *Physical Review Letters*, 115(26):268301, 2015.

[66] Roberto Di Leonardo, Francesca Ianni, and Giancarlo Ruocco. Computer generation of optimal holograms for optical trap arrays. *Optics Express*, 15(4):1913, 2007.

[67] Richard W. Bowman, Graham M. Gibson, Anna Linnenberger, David B. Phillips, James a. Grieve, David M. Carberry, Steven Serati, Mervyn J. Miles, and Miles J. Padgett. Red tweezers: Fast, customisable hologram generation for optical tweezers. *Computer Physics Communications*, 185(1):268–273, 2014.

[68] Stefano Pagliara, Catalin Chimerel, Richard Langford, Dirk G a L Aarts, and Ulrich F Keyser. Parallel sub-micrometre channels with different dimensions for laser scattering detection. *Lab on a chip*, 11(19):3365–8, 2011.

[69] Stefano Pagliara, Simon L. Dettmer, Karolis Misiunas, Lewis Lea, Yizhou Tan, and Urich F. Keyser. Diffusion coefficients and particle transport in synthetic membrane channels. *The European Physical Journal Special Topics*, 223(14):3145–3163, 2014.

[70] Nicolas Chenouard, Ihor Smal, Fabrice de Chaumont, Martin Maška, Ivo F Sbalzarini, Yuanhao Gong, Janick Cardinale, Craig Carthel, Stefano Coraluppi, Mark Winter, Andrew R Cohen, William J Godinez, Karl Rohr, Yannis Kalaidzidis, Liang Liang, James Duncan, Hongying Shen, Yingke Xu, Klas E G Magnusson, Joakim Jaldén, Helen M Blau, Perrine Paul-Gilloteaux, Philippe Roudot, Charles Kervrann, François Waharte, Jean-Yves Tinevez, Spencer L Shorte, Joost Willemse, Katherine Celler, Gilles P van Wezel, Han-Wei Dan, Yuh-Show Tsai, Carlos Ortiz de Solórzano, Jean-Christophe Olivo-Marin, and Erik Meijering. Objective comparison of particle tracking methods. *Nature methods*, 11(3):281–289, 2014.

[71] Carlo Manzo and Maria F Garcia-Parajo. A review of progress in single particle tracking: from methods to biophysical insights. *Rep Prog Phys*, 78(12):124601, 2015.

[72] David G. Grier John C. Crocker. Methods of Digital Video Microscopy for Colloidal Studies. *Journal of Colloid and Interface Science*, 310(179):298–310, 1996.

[73] K. H. Lan, N. Ostrowsky, and Didier. Sornette. Brownian dynamics close to a wall studied by photon correlation spectroscopy from an evanescent wave. *Physical Review Letters*, 57(1):17–20, 1986.

[74] Jonathan Leach, H Mushfique, Stephen. Keen, R Di Leonardo, G Ruocco, J M Cooper, and Miles J Padgett. Comparison of Faxén's correction for a microsphere translating or rotating near a surface. *Physical Review E - Statistical, Nonlinear, and Soft Matter Physics*, 79(2):1–4, 2009.

[75] Simon L. Dettmer, Stefano Pagliara, Karolis Misiunas, and Ulrich F. Keyser. Anisotropic diffusion of spherical particles in closely confining microchannels. *Physical Review E*, 89(6):062305, 2014.

[76] Alice L. Thorneywork. *Structure and dynamics of two-dimensional colloidal hard spheres*. PhD thesis, University of Oxford, 2015.

[77] Vikram Prasad, Denis Semwogerere, and Eric R. Weeks. Confocal microscopy of colloids. *Journal of Physics Condensed Matter*, 19(11):1–25, 2007.

[78] Wolfgang Haiss, Nguyen T K Thanh, Jenny Aveyard, and David G. Fernig. Supporting Information: Determination of size and concentration of gold nanoparticles from UV-Vis spectra. *Analytical Chemistry*, 79(11):4215–4221, 2007.

[79] Guisheng Zhuang and Jörg P Kutter. Anti-stiction coating of PDMS moulds for rapid microchannel fabrication by double replica moulding. *Journal of Micromechanics and Microengineering*, 21(10):105020, 2011.

[80] Karthik Uppulury and Anatoly B Kolomeisky. Channel-facilitated molecular transport: The role of strength and spatial distribution of interactions. *Chemical Physics*, 481:34–41, 2016.

[81] Peter J F Henderson and Stephen a Baldwin. This is about the in and the out. *Nature structural & molecular biology*, 20(6):654–5, 2013.

[82] Matthew Pelton, Kosta Ladavac, and David G. Grier. Transport and fractionation in periodic potential-energy landscapes. *Physical Review E*, 70(3):031108, 2004.

[83] Craig F. Bohren and Donald R. Huffman. *Absorption and scattering of light by small particles*. Wiley, 2004.

[84] Yasuhiro Harada and Toshimitsu Asakura. Radiation forces on a dielectric sphere in the Rayleigh scattering regime. *Optics Communications*, 124(5):529–541, 1996.

[85] Jennifer E. Curtis, Brian A. Koss, and David G. Grier. Dynamic holographic optical tweezers. *Optics Communications*, 207(1-6):169–175, 2002.

[86] Miles Padgett and Roberto Di Leonardo. Holographic optical tweezers and their relevance to lab on chip devices. *Lab on a chip*, 11(7):1196–205, 2011.

[87] Ignacio a Martínez and Dmitri Petrov. Force mapping of an optical trap using an acousto-optical deflector in a time-sharing regime. *Applied optics*, 51(22):5522–6, 2012.

[88] Andrew Callum Richardson, S. Nader S. Reihani Reihani, and Lene Broeng Oddershede. Non-harmonic potential of a single beam optical trap. *Optics express*, 16(20):15709–15717, 2008.

[89] Tahmineh Godazgar, Rouzbeh Shokri, and S. Nader S. Reihani. Potential mapping of optical tweezers. *Optics Letters*, 36(16):3284, 2011.

[90] Marcus Jahnel, Martin Behrndt, Anita Jannasch, Erik Schäffer, and Stephan W. Grill. Measuring the complete force field of an optical trap. *Optics Letters*, 36(7):1260, 2011.

[91] Alejandro V Arzola, Karen Volke-Sepúlveda, and José L Mateos. Force mapping of an extended light pattern in an inclined plane: deterministic regime. *Optics Express*, 17(5):3429–3440, 2009.

[92] Graham Milne, Daniel Rhodes, Michael P MacDonald, and Kishan Dholakia. Fractionation of polydisperse colloid with acousto-optically generated potential energy landscapes. *Optics Letters*, 32(9):1144–1146, 2007.

[93] Michael T Woodside and Steven M Block. Reconstructing folding energy landscapes by single-molecule force spectroscopy. *Annual review of biophysics*, 43:19–39, 2014.

[94] Joan Camunas-Soler, Marco Ribezzi-Crivellari, and Felix Ritort. Elastic Properties of Nucleic Acids by Single-Molecule Force Spectroscopy. *Annual Review of Biophysics*, 45(1):65–84, 2016.

[95] Jongyoon Han, SW Turner, and Harold G Craighead. Entropic trapping and escape of long dna molecules at submicron size constriction. *Physical review letters*, 83(8):1688, 1999.

[96] Daniel Kim, Clark Bowman, Jackson T. Del Bonis-O'Donnell, Anastasios Matzavinos, and Derek Stein. Giant Acceleration of DNA Diffusion in an Array of Entropic Barriers. *Physical Review Letters*, 118(4):048002, 2017.

[97] Sarah E. Henrickson, Martin Misakian, Baldwin Robertson, and John J. Kasianowicz. Driven DNA transport into an asymmetric nanometer-scale pore. *Physical Review Letters*, 85(14):3057–3060, 2000.

[98] Karolis Misiunas, Stefano Pagliara, Eric Lauga, John R. Lister, and Ulrich F. Keyser. Nondecaying Hydrodynamic Interactions along Narrow Channels. *Physical Review Letters*, 115(3):038301, 2015.

[99] Emanuele Locatelli, Matteo Pierno, Fulvio Baldovin, Enzo Orlandini, Yizhou Tan, and Stefano Pagliara. Single-File Escape of Colloidal Particles from Microfluidic Channels. *Physical Review Letters*, 117(3):038001, 2016.

[100] Sang-Hyuk Lee and David G Grier. One-dimensional optical thermal ratchets. *Journal of physics. Condensed matter : an Institute of Physics journal*, 17(47):S3685–95, 2005.

[101] Bob Carpenter, Andrew Gelman, Matthew D. Hoffman, Daniel Lee, Ben Goodrich, Michael Betancourt, Marcus Brubaker, Jiqiang Guo, Peter Li, and Allen Riddell. Stan: A Probabilistic Programming Language. *Journal of Statistical Software*, 76(1), 2017.

[102] Nadine Tarantino, Jean Yves Tinevez, Elizabeth Faris Crowell, Bertrand Boisson, Ricardo Henriques, Musa Mhlanga, Fabrice Agou, Alain Israël, and Emmanuel Laplantine. Tnf and il-1 exhibit distinct ubiquitin requirements for inducing NEMO-IKK supramolecular structures. *Journal of Cell Biology*, 204(2):231–245, 2014.

[103] Leonardo Dagdug, Alexander M. Berezhkovskii, Yurii A. Makhnovskii, Vladimir Yu Zitserman, and Sergey M. Bezrukov. Communication: Turnover behavior of effective mobility in a tube with periodic entropy potential. *Journal of Chemical Physics*, 134(10):132–135, 2011.

[104] John J Kasianowicz, Tam L Nguyen, and Vincent M Stanford. Enhancing molecular flux through nanopores by means of attractive interactions. *Proceedings of the National Academy of Sciences*, 103(31):11431–2, 2006.

[105] Linfeng Sun, Xin Zeng, Chuangye Yan, Xiuyun Sun, Xinqi Gong, Yu Rao, and Nieng Yan. Crystal structure of a bacterial homologue of glucose transporters GLUT1–4. *Nature*, 490(7420):361–366, 2012.

[106] Roland Benz, Angela Schmid, Taiji Nakae, and Greetje H Vos-Scheperkeuter. Pore formation by LamB of Escherichia coli in lipid bilayer membranes. *Journal of bacteriology*, 165(3):978–86, 1986.

[107] Lisen Kullman, Mathias Winterhalter, and Sergey M. Bezrukov. Transport of Maltodextrins through Maltoporin: A Single-Channel Study. *Biophysical Journal*, 82(2):803–812, 2002.

[108] Yaron Caspi, David Zbaida, Hagai Cohen, and Michael Elbaum. Synthetic Mimic of Selective Transport Through the Nuclear Pore Complex. *Nano Letters*, 8(11):3728–3734, 2008.

[109] Charles R Doering and Jonathan C Gadoua. Resonant activation over a fluctuating barrier. *Physical review letters*, 69(16):2318, 1992.

[110] Alexander M Berezhkovskii and Sergey M Bezrukov. Effect of stochastic gating on the flux through a membrane channel: a steady-state approach. *Journal of Physics: Condensed Matter*, 30(25):254006, 2018.

[111] J. Andrew McCammon and Scott H. Northrup. Gated binding of ligands to proteins. *Nature*, 293(5830):316–317, sep 1981.

[112] Huan Xiang Zhou and Attila Szabo. Theory and simulation of stochastically-gated diffusion-influenced reactions. *Journal of Physical Chemistry*, 100(7):2597–2604, 1996.

[113] D. Beece, L. Eisenstein, H. Frauenfelder, D. Good, M. C. Marden, L. Reinisch, K. T. Yue, A. H. Reynolds, and L. B. Sorensen. Solvent Viscosity and Protein Dynamics. *Biochemistry*, 19(23):5147–5157, 1980.

[114] Robert Zwanzig. Dynamical disorder: Passage through a fluctuating bottleneck. *The Journal of Chemical Physics*, 97(5):3587–3589, sep 1992.

[115] N. Eizenberg and J. Klafter. Molecular motion under stochastic gating. *Chemical Physics Letters*, 243(1-2):9–14, 1995.

[116] Feliksas F Bukauskas and Vytas K Verselis. Gap junction channel gating. *Biochimica et Biophysica Acta (BBA) - Biomembranes*, 1662(1-2):42–60, 2004.

[117] Paul C Bressloff. Diffusion in Cells with Stochastically Gated Gap Junctions. *SIAM Journal on Applied Mathematics*, 76(4):1658–1682, 2016.

[118] Bertil Hille. *Ion channels of excitable membranes*, volume 507. Sinauer Sunderland, MA, 2001.

[119] Gregory D Smith. Modeling the stochastic gating of ion channels. In *Computational cell biology*, pages 285–319. Springer, 2002.

[120] Alexander M. Berezhkovskii and Sergey M. Bezrukov. Effect of stochastic gating on channel-facilitated transport of non-interacting and strongly repelling solutes. *Journal of Chemical Physics*, 147(8), 2017.

[121] Glenn L Millhauser, Edwin E Salpeter, and Robert E Oswald. Diffusion models of ion-channel gating and the origin of power-law distributions from single-channel recording. *Proceedings of the National Academy of Sciences*, 85(5):1503–7, 1988.

[122] Igor Goychuk and Peter Hänggi. Ion channel gating: a first-passage time analysis of the Kramers type. *Proceedings of the National Academy of Sciences*, 99(6):3552–3556, 2002.

[123] Luca Gammaitoni, Peter Hänggi, Peter Jung, and Fabio Marchesoni. Stochastic resonance. *Reviews of Modern Physics*, 70(1):223–287, 1998.

[124] Alice Thorneyworka, Yizhou Tan, Jannes Gladrow, Anatoly Kolomeisky, and Ulrich Keyser. Uncovering Fundamental Relations Between Dynamics and Underlying Free-Energy Landscapes from Distributions of First-Passage Events. *To be submitted*, 2018.

[125] Christian Robert. Machine Learning, a Probabilistic Perspective. *CHANCE*, 27(2):62–63, 2014.

[126] Alexander M. Berezhkovskii and Sergey M. Bezrukov. Stochastic Gating as a Novel Mechanism for Channel Selectivity. *Biophysical Journal*, 114(5):1026–1029, 2018.

[127] Shoichi Toyabe, Takahiro Sagawa, Masahito Ueda, Eiro Muneyuki, and Masaki Sano. Experimental demonstration of information-to-energy conversion and validation of the generalized Jarzynski equality. *Nature Physics*, 6(12):988–992, 2010.

[128] Jonne V. Koski, Aki. Kutvonen, Ivan M. Khaymovich, Tapio. Ala-Nissila, and Jukka P. Pekola. On-Chip Maxwell's Demon as an Information-Powered Refrigerator. *Physical Review Letters*, 115(26):1–5, 2015.